Investigation of Barley Proteins' Interfacial Properties and Their Applications as Nanoscaled Materials

by

Jingqi Yang

A thesis submitted in partial fulfillment of the requirements for the degree of

Doctor of Philosophy

in

Food Science and Technology

Department of Agricultural, Food and Nutritional Science
University of Alberta

Abstract

The overall objective of this thesis research is to gain fundamental knowledge on the relationship between barley protein molecular structures and their interfacial properties as well as to develop barley protein value-added applications with special emphasis on their utilization as nanoparticles for delivery systems of lipophilic bioactive compounds and electrospun nanofibers. Firstly, the interfacial properties of barley proteins were investigated using B-hordein as a representative. The results revealed that B-hordein had the ability to lower the air-water surface tension to 45 mN/s within 2 h and formed an elastic-dominant film at the interface through intermolecular β-sheets, which stabilized the interface. Compression at the interfacial B-hordein film triggered the conformation and orientation changes of B-hordein. This resulted in the occultation of the repetitive region of B-hordein from aqueous phase, leading to a low digestibility in simulated gastric fluids. Based on this knowledge, barley protein based nanoparticles were successfully developed by high pressure homogenization as a delivery system for lipophilic bioactive compounds. At optimized processing conditions, nanoparticles with regular spherical shape, smooth surface, size of 90-150 nm and zeta-potential of -35 mV were obtained. Barley protein based nanoparticles had less than 2% of the encapsulated bioactive compounds released after incubation in simulated gastric fluids for 2 h and the complete release occurred in simulated intestinal fluids due to pancreatin degradation. Thus, they had potential to protect the encapsulated bioactive compounds in harsh gastric environment, and completely release them in the small intestine, which was the main adsorption site to improve absorption.

Barley protein based nanoparticles were resistant to pepsin digestion, had low cytotoxicity and could be internalized by Caco-2 cells. Thus, these barley protein nanoparticles showed strong potential to be used as delivery systems of bioactive compounds for food, pharmaceutical and cosmetic applications.

The third and fourth studies explored the opportunity of using barley protein based electrospun fabrics for applications as electrode materials for supercapacitors. Hordein, the major fraction of barley proteins, was electrospun into fibers with zein and lignin. The protein-lignin fibers were then converted into carbon fibers by carbonization at 900°C under argon. The specific surface area was 772 m^2/g after activation by CO_2 at 800°C for 3 h. These carbon fibers had 3D hierarchical porous structure, high amount (4 atomic%) of nitrogen on the carbon surface and graphene-like nanosheet structures. Such morphology and chemical composition allowed carbon fibers with excellent capacitance of 240 F/g and 31.2 $\mu F/cm^2$ in 6 M KOH with high cyclic stability. To further increase the nitrogen content, in the last study, calcium acetate was added in the electrospinning solution to form nanofibers with protein, sustain the fibrous structure and generate pores during carbonization. Nitrogen-doped (7%) porous graphitic carbon fibers were derived from protein-Ca^{2+} fibers through one-step pyrolysis, which was facile and environmentally friendly. Moreover, it was the first time that highly ordered spherical graphitic structure was observed in carbon fibers derived from biomass at relatively low temperature (850°C) without catalysis and corrosive reagents. Based on their structure and chemical features, these carbon fibers had a specific capacitance of 64 $\mu F/cm^2$ and 98% retention after 5,000 cycles,

which was ranking in the most excellent range of carbon fibers reported recently. These carbon fibers have the potential to be used in industrial energy storage systems and personal electronic products.

Preface

Chapter 2 of this thesis has been published as Jingqi Yang, Jun Hunag, Hongbo Zheng, Lingyun Chen, "Surface pressure affects B-hordein network formation at the air-water interface in relation to gastric digestibility" in Colloids and Surfaces B: Biointerfaces 2015, *135*, 784-792. I was responsible for conducting experiments and analyzing data as well as preparing the manuscript. Assistance was received from Jun Huang in obtaining atomic force microscopic images. Drs. Hongbo Zeng and Lingyun Chen were supervisory authors. Dr. Zeng provided accessible lab equipment including AFM and Langmuir-Blodgett trough. Dr. Lingyun Chen was responsible for manuscript revision, editing and submission.

Chapter 3 of this thesis has been published as Jingqi Yang, Ying Zhou, Lingyun Chen, "Elaboration and characterization of barley protein nanoparticles as an oral delivery system for lipophilic bioactive compounds" in Food & Function 2014, *5*, 92-101. I was responsible for conducting experiments and analyzing data as well as preparing the manuscript. Ying Zhou provided me assistance with the cell culture work. Dr. Lingyun Chen was supervisory author and responsible for manuscript revision, editing and submission.

Chapter 4 of this thesis has been submitted as Jingqi Yang, Yixiang Wang, Jingli Luo, Lingyun Chen, "Creation of 3D hierarchical porous nitrogen-doped carbon fibers for supercapacitors from plant protein and lignin electrospun fibers". I was responsible for conducting experiments and analyzing data as well as preparing the manuscript. Yixiang Wang provided assistance in protein-lignin electrospun fabric preparation and manuscript preparation. Drs. Jingli Luo and

Lingyun Chen were supervisory authors. Dr. Luo provided assistance in electrochemical properties measurements. Dr. Lingyun Chen was responsible for manuscript revision, editing and submission.

Another manuscript based on Chapter 5 is to be submitted soon as Jingqi Yang, Yixiang Wang, Jingli Luo and Lingyun Chen, "Nitrogen-doped porous graphitic carbon fibers for supercapacitor from plant proteins". I was responsible for conducting experiments and analyzing data as well as preparing the manuscript. Yixiang Wang provided assistance in protein-lignin electrospun fabric preparation and manuscript preparation. Drs. Jingli Luo and Lingyun Chen were supervisory authors. Dr. Luo provided assistance in electrochemical properties measurements. Dr. Lingyun Chen was responsible for manuscript revision, editing and submission.

Acknowledgements

Firstly, I would like to give my sincere appreciation to Dr. Lingyun Chen, my supervisor for this long-term PhD program. Without her support, guidance, encouragement and trust, this tough journey would never be accomplished. I still remembered the telephone interview with Dr. Chen in early 2010 when she offered me the opportunity to come to Canada and pursue my dream of doing research. From that point, my life was completely changed. Dr. Chen provides me with abundance of help on my way to become a qualified PhD student and a more mature researcher. I also would like to thank Drs. Feral Temelli and Thava Vasanthan for serving as supervisory committee members. They give me lots of patience, support and encouragement in these unforgettable five years. I am also grateful to Drs. Weixing Chen and Ashraf Ismail for their help with my thesis and final exam.

Also, I would like to thank my parents and my husband. I would like to say many thanks to my parents who love me unconditionally and give me endless support. My husband, Victor Liu, is always my sunshine. Thank you for going through all the ups and downs together with me. Victor makes my life bright and colorful. I am very happy that we will have our first baby Yuzhi Liu in early 2016.

Special thanks also go to my lovely group members. I am so grateful to have all of them in my life. They are all genius in doing research and they are great friends in daily life. It is my honor and pleasure to work with these excellent people. All the joyful moments we share together are unforgettable.

Table of Contents

List of Tables

List of Figures

List of Abbreviations and Symbols

AFM	Atomic force microscopy
ANOVA	Analysis of variance
ATR	Attenuated total reflectance
CA	Calcium acetate
CLSM	Confocal laser scanning microscopy
CNF	Carbon nanofiber
CV	Cyclic voltammetry
Cys	Cysteine
DAPI	4’,6-diamidino-2-phenylindole
DMF	Dimethylformamide
DMEM	Dulbecco’s modified Eagle's medium
DMSO	Dimethyl sulfoxide
E’	Interfacial dilatational storage modulus
E’’	Interfacial dilatational loss modulus
EDLC	Electric double layer capacitor
EDTA	Ethylenediaminetetraacetic acid
EE	Encapsulation efficiency
EIS	Electrochemical impedance spectroscopy
FBS	Fetal bovine serum
FE-SEM	Field emission-scanning electron microscope
FTIR	Fourier transform infrared
G’	Interfacial shear storage modulus
G’’	Interfacial shear loss modulus
GI	Gastrointestinal
Gln	Glutamine

Glx	Glutamine or glutamic acid
HBSS	Hanks' balanced salt solution
HEPES	4-(2-hydroxyethyl)-1-piperazineethanesulfonic acid
HR-TEM	High resolution-transmission electron microscopy
Ile	Isoleucine
IRRAS	Infrared absorption reflection spectroscopy
LC	Loading capacity
Leu	Leucine
Lys	Lysine
MTT	3-(4,5-Dimethylthiazol-2-yl)-2,5-Diphenyltetrazolium Bromide
NEAA	Non-essential amino acid
NMP	N-methyl-2-pyrrolidone
PAN	Polyacrylonitrile
PANI	Polyaniline
PBS	Phosphate-buffered saline
PDI	Polydispersity index
Phe	Phenylalanine
pI	Isoelectric point
PM-IRRAS	Polarization modulation- infrared absorption reflection spectroscopy
PPy	Polypyrrol
Pro	Proline
PVDF	Polyvinylidene fluoride
RI	Refractive index
RMS	Root mean square
SDS-PAGE	Sodium dodecyl sulfate polyacrylamide gel electrophoresis
SEM	Scanning electron microscope

SGF	Simulated gastric fluid
SIF	Simulated intestinal fluid
t	Time
TEM	Transmission electrical microscopy
TFA	Trifluoroacetic acid
TGA	Thermogravimetric analysis
Trp	Tryptophan
UV	Ultraviolet
Val	Valine
XPS	X-ray photoelectron spectroscopy
XRD	X-ray powder diffraction
α-Lac	α-Lactalbumin
β-Lac	β-Lactoglobulin
δ	Phase lag
ε	Dielectric constant
λ	Wavelength
Π	Surface pressure
σ	Surface tension

Chapter 1

Literature Review

1.1 Barley grains

Barley (*Hordeum vulgare* L.) is the fourth most important crop on earth after wheat, rice and corn. Barley is adapted to a wide range of natural climate and soil conditions. European Union, Russia and Canada are the major producers of barley, providing about 100 million tons of barley per year.[1, 2] Alberta produces more than 5 million tons of barley per year, which contributes more than half of the barley production in Canada. Livestock feeding and malt products are the main consumptions of barley production (about 80-90%) in many western countries. Human consumption of Alberta barley is rather limited.[2] Recently, barley has attracted great attention since the high amount of dietary fibers in grains, especially β-glucan has been reported to show health-promoting benefits, such as controlling diabetes, reducing cholesterol level and the risk of cardiovascular diseases.[3, 4] Despite the large production and the potential health benefits, value-added applications of barley in food and non-food industries have not been sufficiently developed.

Barley grain kernel has a spindle like shape, which is thicker in the center and tapered towards two ends. It consists of two parts, the caryopsis and the hull. Some hullless varieties have been developed. The caryopsis is comprised of the pericarp, integuments, aleurone layer, endosperm and germ/embryo.[2] After removing the husk, endosperm, aleurone layer and the embryo are the

three major tissues. The major components of barley grain are starch (60-64% of dry weight), protein (8-15%), arabinoxylans (4.4-7.8%), β-glucans (3.6-6.1%), lipids (2-3%) and minerals (3%).[2]

1.2 Barley protein

1.2.1 Overview of barley protein

Proteins are the second major component of dry barley grains. Due to the high production every year, barley is an affordable and abundant source of food proteins. The content and profile of proteins in barley seeds vary among different cultivars and are affected by the environmental conditions during growth, such as temperature, sunshine and soil conditions.[5] According to the classification method developed by Osborne, barley seed proteins can be classified into 4 categories, i.e. albumin, globulin, hordein and glutelin, based on their different solubilities. Albumins and globulins are mainly located in the bran and embryo, thus, called cytoplasmic proteins. They comprise 3-4% and 10-20% of the total seed proteins, respectively. Albumins are water soluble while globulins can be extracted by dilute salt buffer (0.5M NaCl). Hordeins, the prolamin in barley grain, are soluble in 70% ethyl alcohol and comprise about 30-50% of total barley proteins. Glutelins are soluble in dilute acid/alkali, which are the leftover fraction after sequential extraction by water, dilute salt solution and 70% ethanol. Some recent studies reported that glutelins were considered as a group of the prolamin (hordein for barley) family due to their similar gene sequences, biosynthesis mechanism and also the physiological functions.[6] Hordeins

and glutelins are mainly found in the starchy endosperm, together contributing to about 70-90% of the total dry seed proteins.

Hordeins are the major barley storage proteins, which can be classified into 5 fractions based on their electrophoretic mobilities and amino acid compositions: A-hordein, B-hordein (70-90%), C-hordein (10-20%), D- and γ-hordein (less than 5%).[7] A-hordeins are a group of low molecular weight polypeptides (M_w<15 kDa). B hordeins are the main fraction of hordein and can be separated into 3 distinguishable subtypes, B1-, B2- and B3-hordeins. Their molecular weights range from 34 to 46 kDa. As the second major hordein fraction, C-hordeins appear as monomers with 55 kDa. D-hordeins are larger than 100 kDa and belong to high molecular weight prolamin family. D-hordein molecules are composed of two or more polypeptides cross-linked by intra-chain disulfide bonds.[7] γ-Hordeins are less than 20 kDa and composed of two classes, γ- and γ3-hordeins.[8]

1.2.2 Amino acid composition of barley proteins

The amino acid compositions of the 4 barley protein fractions are shown in Table 1-1.[9] Barley proteins are recognized as incomplete proteins for food and feed applications because of the low content of lysine (Lys) and tryptophan (Trp) in the major storage proteins. Both hordeins and glutelins are rich in glutamine (Gln), proline (Pro) and hydrophobic amino acids such as valine (Val), leucine (Leu), isoleucine (Ile) and phenylalanine (Phe). Due to the large amount of

hydrophobic amino acids and low charged amino acids, barley storage proteins are water insoluble, whereas, albumins and globulins are high in Lys and low in Gln and Pro.

Table 1-1 Amino acid composition of barley protein fractions (mol%)[9]

Amino Acid	Albumin	Globulin	Hordein	Glutelin
Ala	9.3	7.9	2.6	10
Asp	10.6	10.5	1.8	11.5
Cys	6.5	5.6	2.4	/
Glu	19.2	14.5	35	21
Gly	10.8	12.7	3.1	12.5
Ile	3.8	3	5.3	6
Leu	6.8	8.4	7.8	10.9
Lys	3.4	7.8	0.6	0.8
Met	2.5	1.6	1.2	1.9
Phe	3.6	4.4	6.8	5.3
Pro	6.1	7.3	20.1	2.1
Ser	6.7	7.9	5.8	9.7
Tyr	4.4	3	3.3	1.1
Val+Thr	6.4	5.5	4.3	7.2

The amino acid compositions of the different hordein fractions are listed in Table 1-2.[10] C-hordeins are distinguishable to other hordein fractions due to their low content of cysteine (Cys), which is the essential amino acid to develop disulfide bonds. Also, C-hordeins are rich in Glx (glutamine or glutamic acid), Pro and Phe, together taking up more than 60% of the amino

acid residues. Glx, Pro and Phe are mainly found in the middle repetitive motif of the C-hordein sequence. B-, D- and γ-hordeins have more Cys residues, which provide them the possibility of developing inter and intra molecular disulfide bonds.

Table 1-2 Amino acid compositions of hordein fractions (mol%)[10]

Amino Acid	γ-hordein	B-hordein	C-hordein	D-hordein
Ala	2.1	2.6	1.5	3.2
Arg	1.8	2.6	0.9	1.6
Asx	2.4	0.7	1.5	1.5
Cys	3.5	2.9	/	1.5
Glx	28	30	37	28
Gly	3.1	2.9	0.6	15.7
His	1.4	1.5	0.6	3
Ile	3.8	4.4	3.4	0.7
Leu	7	8	8.6	4.1
Lys	1.8	0.7	0.9	1.2
Met	1.8	1.1	/	0.4
Phe	5.6	4.7	7.7	1.3
Pro	16.8	19.4	29.1	10.5
Ser	5.6	4.7	2.5	10.5
Thr	3.1	2.2	1.2	7.3
Trp	0.7	0.7	0.6	1.2
Tyr	2.1	2.6	1.8	4.2

1.2.3 Structure of barley proteins

Though hundreds of barley proteins have been identified, only a few of them has been characterized and their structures have not been clearly revealed. B and C hordeins are the most intensively explored barley proteins.

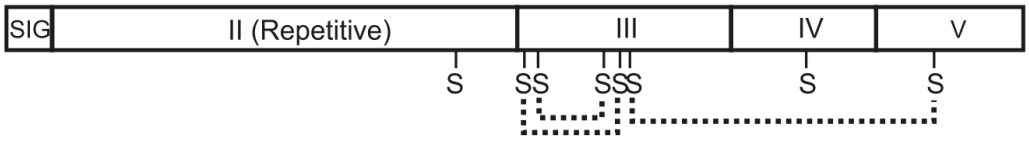

Figure 1-1 Simplified structure of orthologous B-hordeins. SIG represents signal peptide. S indicates Cys residues and broken line demonstrats the presumptive disulfide bonds.[8]

B-hordein polypeptide chain is composed of 5 domains as showed in Figure 1-1. The first domain is a short signal peptide starting from the N-terminal. Domain II is a repetitive region of variations on short repetitive motifs. The remaining region is occupied by a nonrepetitive region containing 5 Cys residues (domain III), a region high in Gln (domain IV) and a C-terminal repetitive domain (domain V). B-hordein is found to have 8 Cys residues. Six of these Cys residues may form intramolecular disulfide bonds and contribute to the stability of the folding of B-hordein polypeptide chain. The remaining two free Cys residues are likely to promote the aggregation of B-hordeins. The repetitive region (second domain) takes up about half of all the amino acid residues of B-hordein. The repetitive domain contains a large number of hydrophobic amino acids, including Pro, Val, Iso, Leu and Phe. Four amino acid residues motif

(Pro-Phe/Tyr-Pro-Gln) is a common repeat motif pattern found within the repetitive domain.[8] Pro is a unique amino acid since its side chain is cyclised back onto the backbone amide position. The backbone φ dihedral angle is restricted to a limited range around -65°. Meanwhile, the bulkiness of the N-CH_2 group leads to space restriction on the conformation of Pro residue, making it unfavourable to form α-helix. Since the amide proton is replaced by a CH_2 group, Pro residue is not able to be a hydrogen bond donor. Based on the knowledge gained from other proline-rich tandomly repetitive proteins, such as the salivary proline-rich proteins and elastin, B hordein polypeptide chains are more likely to be rigid, extended and have a higher chance to form β-conformation.[11] The repetitive appearance of aromatic amino acids, such as Tyr, Phe and Trp in domain II is much more frequent than in other domains. Large amount of aromatic amino acids may contribute to the stability of protein conformation and development of inter/intra protein interactions.[12] The third domain contains about 5 Cys residues, which may participate in the development of inter/intra protein disulfide bonds. Moreover, within domain IV, about 50% of amino acid residues are Gln, which result in a relatively hydrophilic nature.[8] However, the conformation of B-hordein is still insufficiently explored. Gaining knowledge in this area is important to support its further application development.

Compared to B-hordein, the structure and conformation of C-hordein received more intensive studies. C-hordeins also have high content of Gln (40-50 mol%), Pro (20-30 mol%) and Phe (7-9 mol%), but do not contain Cys and have low content of charged amino acid residues. C-hordeins are a group of proteins sharing highly homologous structure with short N- and C-terminal

domains at two sides and a long repetitive domain in between.[13] The consensus repeat sequence is $(Pro\text{-}Phe\text{-}Pro\text{-}Gln)_{1\text{-}2}(Pro\text{-}Gln\text{-}Gln)_{1\text{-}2}$. Molecular modelling techniques were used to predict the possible structure of repetitive motif. Results suggested that they were more likely to form overlapping β-turns and develop a helical structure with little or no α-helix and β-sheet.[14] The circular dichroism (CD) spectroscopy of C hordein in 70% ethanol concluded that β-turns were found while α-helix and β-sheet were absent. C-hordein was in rod shape with a molecular size from about 36 × 1.7 nm to 26.5 × 2 nm.[15]

1.2.4 Nutritive value and functionalities of barley proteins

Barley endosperm proteins have a moderate nutritional quality due to its relatively low content of Lys and Trp, which are essential amino acids for human.[16] Although barley proteins are not competitive for nutritional purpose, barley proteins show some interesting functionalities, which have potential to be utilized in food and non-food industries. Some previous studies have characterized the emulsifying, foaming, encapsulating and film-forming properties of barley proteins as following described in detail.

1.2.4.1 Emulsifying capacity

Emulsification is one of the most important processes in manufacturing of many food and non-food products. Proteins are used as emulsifiers since they have the ability to lower the oil-water interfacial tension and stabilize the emulsion by forming a protein film at the surface of oil droplets.[17] The relation between protein structure and their emulsifying capacity will be

discussed in the next section. Wang *et al.* [18] concluded that barley glutelin demonstrated balanced water and oil holding capacities and strong oil binding capacity, which resulted in supreme emulsifying capacity. Since the emulsifying properties of proteins were positively correlated to their solubility,[19] Zhao and her colleges [20, 21] tried to improve the solubility and emulsifying properties of barley glutelin and hordein by deamidation treatments. Even a limited degree of deamidation significantly increased glutelin and hordein solubility in water and strongly improved their emulsifying capacities at a wide pH range.[20, 21] However, the fundamental knowledge of barley protein behaviour at the interface has not been explored yet.

1.2.4.2 Foaming capacity

Foaming properties are another kind of protein functionality related to protein behaviour at the interface. Protein characteristics, including solubility, size, surface hydrophobicity, structure flexibility and protein-protein interactions, all play important roles in its foaming capacity. Kapp *et al.*[22] found that both barley albumin and hordein fraction had the capacity to produce stable foams. Kapp *et al.* [22] believed that the flexible structure of albumin and the hydrophobic nature of hordein contributed to their foaming capacities. The application of barley protein as a foaming agent was limited by its low solubility at neutral pH. Modification techniques, such as denaturation, proteolysis,[22] acetylation[1] and deamidation,[20, 21] have been employed to improve the foaming capacity of barley protein.

1.2.4.3 Film forming capacity

Biodegradable films produced from biopolymers, such as proteins, have attracted extensive attention recently, since they can provide alternatives for petroleum-based films. Barley protein film has been successfully prepared by thermopressing with glycerol as plasticizer. Barley proteins are good candidates to prepare film because barley proteins, especially hordein, show good cohesive and elastic properties. Barley protein films possessed good moisture barrier properties, resulting from the hydrophobic nature of barley protein.[23]

1.2.4.4 Encapsulation capacity

Due to the good emulsifying and film forming properties, barley proteins can be used as wall materials to encapsulate active compounds.[24, 25] Microcapsules of fish oil and β-carotene based on barley protein had been successfully developed.[26, 27] Barley proteins could form a thick and solid matrix after high pressure homogenization, encapsulating the oil phase inside. Barley proteins microencapsulation prevented fish oil and β-carotene from oxidation since the thick and integrate protein coating was a good oxygen barrier. Moreover, due to the low solubility of barley prolamin in the aqueous environment, barley protein encapsulations potentially resisted swelling and controlled the release of the encapsulated compounds in solution and under humid conditions. This was a unique characteristic for barley protein microcapsules as compared to other food grade hydrophilic proteins, such as soy proteins and whey proteins. Notably, a thin layer of barley protein could resist pepsin degradation and prevent the encapsulated compound

from being released. The oil phase was slowly released under simulated intestinal conditions.[26, 27] Based on its release profile, barley protein microcapsule has potential to be used as a delivery system to improve the bioavailability of the encapsulated bioactive compounds.

1.2.4.5 Electrospinnability

Hordeins, the major faction of barley proteins, can be prepared into nanofibers through electrospinning without any assistance of synthetic polymers.[28] When cooperating with zein nanoparticles, hordein nanofibers exhibited a stable network structure and had improved tensile strength and stability in both water and ethanol.[28] The mechanical properties of electrospun hordein and zein nanofibers could be further improved by adding cellulose nanowhiskers.[29] Protein nanofibers have various potential applications, such as delivery systems, wound dressing materials, smart textile, composites of biosensor and precursor of carbon fibers.[30, 31]

1.3 Interfacial properties of barley proteins and their applications

The boundary between two immiscible phases is defined as an 'interface'. This thesis research focused on water-oil and water-air interfaces. To simplify, here, the word 'interface' refers to both water-oil and water-air interfaces. Emulsions and foams commonly exist in complex food systems. Their formation and stabilization strongly rely on the behaviour of interfaces during processing and storage.[32] Usually, interface is occupied by one or more layers of surface active components, which prevents oil droplets/ air bubbles from aggregation and/or coalescence. Surface active components can be roughly classified into two categories, small molecular

surfactants (such as polysorbate, fatty acids, phospholipids) and surface active polymers.[33] Proteins are widely utilized as emulsifying and foaming agents since they are biocompatible and have the capacity to adsorb to the interface, lower interfacial tension and form a 2D viscoelastic film to stabilize the interface [17]. The surface activity of protein depends on many factors, such as its thermodynamic stability, structure flexibility, amphipathicity, size and charge.[34]

As mentioned above, barley proteins were shown to be surface active[18] and able to form a solid-like coating at oil-water interfaces. The latter was different from many hydrophilic food proteins which were more likely to form liquid-like or gel-like films at oil-water interfaces.[27, 35] Despite this, their interfacial behaviour is not well studied yet.

1.3.1 Protein behaviour at the interface

In general, proteins stabilize the interface through the following process. First, proteins diffuse from solution to the interface and anchor onto the interface. This step depends on intrinsic properties of proteins and also on physical properties of the bulk phase, such as viscosity, density, purity and polarity.[32] Protein absorption results in a decrease of interfacial tension. Generally, protein absorption is considered as irreversible since desorption of protein molecules from interface, especially air-water surface, is a hindered process due to the existence of an activation energy barrier.[36] In bulk solution, protein molecules tend to expose the hydrophilic residues to water, covering the hydrophobic interior. Once proteins are adsorbed to interface, hydrophobic segments may be in contact with the air or oil phase which reduce the hydrophobic interactions

and destabilize protein's original secondary and tertiary structures. Thus, protein molecules change their conformation to expose the hidden hydrophobic regions and re-orient themselves towards the air/oil phase.[37] The adsorption and further conformation changes of proteins play an essential role in reducing the interfacial tension. When more proteins adsorb to the interface, the space between protein molecules decreases, which results in physical entanglements and intermolecular interactions with each other through non-covalent and covalent bonds.[17] The physical entanglements and intermolecular interactions among protein molecules play an important role in determining the mechanical property of interfacial protein layers.

1.3.2 Interfacial tension

Interfacial tension at the water interface is considered as the result of the attraction of the bulk liquid for the surface layer. At air-water interface, the cohesive forces between liquid molecules contribute to interfacial tension phenomenon.[38] Protein adsorption and the subsequent conformation changes and re-orientation could reduce the interface tension.[39, 40] The interfacial tension is not lowered instantaneously, especially when polymers are used as surface active materials. When protein is adsorbed to the interface, both the equilibrium interfacial tension value and the time at which equilibrium value is reached are important.[41]

Static interfacial tension measurements are used to determine the equilibrium interfacial tension.[42] Dynamic interfacial tension shows the change in interfacial tension as a function of time. The dynamic interfacial tension is usually measured to obtain the information on protein

absorption kinetics. The interfacial tension-time plot demonstrates three distinct regions: (1) initial induction region with minimal tension reduction, which depends on the diffusion and protein interfacial affinity; (2) steep tension decline region in which protein molecules contact the interface and change their orientation and conformation until the formation of monolayer coverage; (3) final region in which the rate of tension reduction slows down until the equilibrium is reached. The final region is attributed to the further conformational changes of protein, continued relaxation of the adsorbed layer and possible build-up of multilayers.[43] Some studies also separate the final stage into the mesoequilibrium region and the steady-state region.[44]

During foaming and emulsifying, large interfacial areas are created. Newly formed interfaces are needed to be stabilized by surface active molecules to prevent bubbles or droplets from coalescence. In these cases, the dynamic surface tension of protein plays an important role in determining the final emulsion droplet size/foam bubble size.[45] The slower proteins can adsorb to interface, the higher is the chance to have large droplet sizes under the same processing conditions.

The ability of proteins to lower the surface tension is recognized to be dependent on intrinsic factors of protein molecules (such as molecular weight, hydrophobicity and chain flexibility) as well as factors of the bulk solution (such as protein concentration, pH, temperature, ionic strength, viscosity and present of other surfactants).[46, 47] For example, Suttiprasit *et al.* [48] compared the surface activity of α-lactalbumin (α-Lac), β-lactoglobulin (β-Lac) and bovine serum albumin. They found that α-Lac had the fastest rate to reduce the surface tension and the

lowest equilibrium surface tension at the same condition, which was possibly due to its low molecular weight and least stable protein structure. Tripp *et al*. [44] found that the protein concentration in solution influenced both the equilibrium interfacial tension and the rate of reaching an equilibrium status. For higher protein concentration, diffusion step was no longer a rate-limiting process.[44]

The change in interfacial tension from pure fluid value is considered as surface pressure $\Pi(t) = \sigma_0 - \sigma(t)$, where σ_0 is the surface tension of the pure fluid and t is time.[49] Techniques to measure dynamic surface pressure include maximum bubble pressure, inclined plate, drop pressure, drop volume, pendant drop and plate or ring tensiometry, which have various measurement time windows.[39] Pendant drop technique is widely used to observe the dynamic surface tension change of protein absorption from dilute solution to interface.[43] For pendant drop method, a drop is suspended from a needle in another bulk liquid or gas phase. The shape of the drop is determined by the relationship between the surface tension and gravity.[50] The surface tension is calculated from the drop shape through Young-Laplace equation. A computer controlled system allows the acquisition of drop image, detection of the drop shape and fitting the equation to determine the dynamic surface tension automatically.[43]

1.3.3 Interfacial rheology of protein films

Interfacial rheology studies the relationship between the deformation of a liquid surface and the accompanying forces. When proteins adsorb to the interface, protein molecules can form a

visco-elastic film around the oil-water or air-water interface through non-covalent and/or covalent interactions. The viscosity and elasticity of protein interfacial thin film can be determined by interfacial rheology.[32] Interfacial rheological properties are commonly considered to be correlated to the structure and composition of the protein film. The major difference between interfacial dilatation and shear rheology is that dilatational deformation has area change while shear deformation does not. Thus, interfacial dilatational rheology is able to provide information on the kinetics of adsorption and desorption of the surface active molecules and detect the intrinsic softness and hardness of the molecules at the interface. Interfacial shear rheology is an indicator of the conformational changes of protein molecules and their interactions.[51]

The changes of shear storage modulus (G') and loss modulus (G'') as a function of time elucidate the adsorption of protein molecules and the interfacial protein network development.[52, 53] Freer *et al.* [54] found that for lysozyme, the complex interfacial shear modulus G* (G* = G' + *i*G'') increased as aging time extended, indicating a conversion from liquid-like behaviour at the early stage to more gel-like network formation. Lysozyme molecules partially unfolded after being adsorbed to the interface, which facilitated the build-up of strong intermolecular interactions leading to the increase of G' with time. However, the strong intramolecular interaction of lysozyme molecules was considered as a kinetic barrier for partial denaturation at the adsorption stage.[54] Cascão Pereira *et al.* [55] found that both the intrinsic stability of protein structure and the lateral interactions between protein molecules contributed to the shear elasticity

of the protein film. The conformation and orientation changes of protein at interface strongly influence the development of intermolecular interactions; thus, influence the interfacial rheological properties.[51] Factors disrupting or strengthening the inter and/or intramolecular interactions can lead to changes in the interfacial rheological properties, such as ionic strength, temperature, aging, chemical and enzymatic modification as well as the addition of polysaccharides and/or small molecular surfactants.[51]

The direct quantitative relationship between protein interfacial rheological properties, and formation and stability of foam and/or emulsion is difficult to determine, since all the interfacial rheology measurements are made on model macroscopic interfaces and the range of analysis parameters (such as stress, strain and rate of deformation) do not reflect the turbulent non-equilibrium conditions during foaming and emulsifying.[32] Despite this consideration, experimental evidence still confirms that the formation of interfacial protein network is correlated to the stability of air-water and oil-water interfaces.[52] The stability of emulsions and foams is linked to both dilatational and shear rheological properties, because both dilatational and shear deformations occur in oil droplet (air bubble) collision and film drainage.[52] For instance, Kim *et al.*[56] compared the interfacial shear rheological properties of native and heated β-Lac. The heated β-Lac had a higher surface hydrophobicity and more flexible structure, leading to lower surface tension and increase of intermolecular interactions between interfacial protein molecules. Thus, they found that the G' of heated β-Lac increased and resulted in an increased resistance to coalescence of oil droplets and higher stability of the bulk emulsion.[56]

Understanding the relationship between protein interfacial film rheology and emulsion degradation processes is important for controlling lipid digestibility and rational design of emulsions with desired digestibility.[57-60] However, research on this new area is insufficient.[60] Lipases work at the oil-water interface. For emulsions stabilized by proteins, the resistance of proteins to lipase displacement from interface and the resistance of protein layers to degradation play important roles in controlling the digestibility of emulsion.[61] Maldonado-Valderrama [59, 62] found that β-Lac had a higher dilatational modulus at air-water than oil-water interface, which might be caused by the higher level of conformational changes of β-Lac at air-water interface. The stronger protein film formed at air-water interfaces hindered bile salt displacement more than the weaker structure formed at oil-water interfaces. Previous study in our group showed that a thin film of barley protein at the oil-water interface can resist the degradation in simulated gastric fluid (SGF). This result is interesting for developing delivery systems with controlled lipid digestibility.[27] However, the resistance mechanism of barley protein is still not clear. The relationship between interfacial rheological properties of barley protein film and its digestibility needs to be investigated.

1.3.4 Protein conformational changes at the interface

The partial denaturation of protein at interface influences its adsorption kinetics and the further development of the viscoelastic interfacial protein film. Thus, the conformation and orientation of protein at interface play a significant role in the formation and stabilization of the emulsion

and/or foams.[63-65] Hence, many studies attempted to reveal protein conformational changes. The degree of protein conformational rearrangement at the interface depends not only on the properties of the interface but also on the protein intrinsic conformational stability.[66] It has found that although proteins have the tendency to unfold at interface, they still maintain some secondary structures.[67, 68]

Fourier transform infrared (FTIR) and infrared absorption reflection spectroscopy (IRRAS) are two of the most popular techniques used to study the protein conformation and orientation at interfaces. The amide I and II regions of the infrared spectra are the most prominent vibrational bands of the protein backbone. Amide I (1700 to 1600 cm^{-1}) is the most sensitive region to the protein secondary structure because the C=O stretch vibrations of the peptide linkages contribute to approximately 80% of the amide I region.[69] Each type of their secondary structure has a different C=O stretching frequency due to unique molecular geometry and hydrogen bonding pattern.[69-71] FTIR involves a measurement of the intensity of the absorption of IR radiation at a given wavelength by a sample, whereas with IRRAS, interfacial protein structures are measured by the spectrum of an IR beam that is reflected from the interface.[72] Polarization modulation-IRRAS (PM-IRRAS) has high sensitivity to the orientation of the transition moment at the interface due to surface selection rule, which can reveal the orientation of interfacial proteins.[72-75]

As analyzed by FTIR, after being adsorbed to the oil-water interface, β-lactoglobulin had an increase in the band at 1682 cm^{-1}, which is assigned to intermolecular β-sheets.[76] Banc *et al.* [77]

coupled Langmuir-Blodgett trough with PM-IRRAS and found that intermolecular β-sheets of γ-gliadin increased at the expense of β-turns when the interface was getting crowded with γ-gliadin molecules. These results confirmed that the conformational changes of protein after being adsorpted to the interface played an important role in the formation of interfacial protein network. Moreover, studies also revealed that the protein conformation changes influenced the response of protein films to different pH [78] and surfactant replacement.[62]

1.4 Protein electrospun nanofibers

1.4.1 Electrospinning technique

Polymer nanofibers have a large surface area to volume ratio, flexible surface functionalities and controllable mechanical performance, which make them suitable for many applications, such as separation membranes, wound dressing materials, controlled drug release system, biocompatible scaffolds and many other applications.[79] Figure 1-2 shows a typical scanning electron microscope (SEM) image of electrospun nanofibers prepared from plant proteins. Nanofibers can be produced by many techniques, including template synthesis, phase separation, self assembly and electrospinning.[80] Among them, electrospinning has attracted great attention since it is a relatively simple and efficient technology to prepare polymer fibers with diameters from 2 nm to several μm.[81] Advantages of electrospinning include but are not limited to: (1) producing nonwoven fabrics with nanofibers within a relatively short time; (2) suitable to form fibers with

wide varieties of materials; (3) able to encapsulate core materials inside fibers and (4) able to control the fiber diameter and alignment.[80, 82, 83]

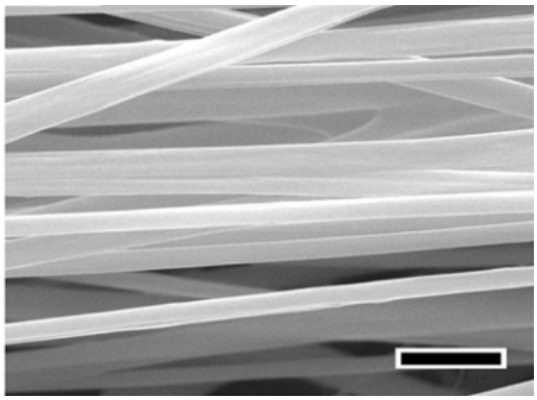

Figure 1-2 SEM image of orientated electrospun hordein/zein fibers. Scale bar: 5μm.[30]

As shown in Figure 1-3, the three major components of an electrospinning equipment are high voltage power supply, a capillary tube with a pipette or needle of small diameter and a collector. The polymer solution can be generated by dissolving in an appropriate solvent or by melting it with high temperature and/or shear stress. Polymer solution is held at the end of a capillary tube by its surface tension. The collector is grounded while the electric field is subjected to the end of the capillary tube that contains the solution. The high voltage supplier allows the creation of an electrically charged jet of polymer solution or melt out of the pipette. Direct current voltage in the range of several to several tens of kV is needed to generate electrospinning. The liquid jet evaporates or solidifies before it is collected as an interconnected network of small fibers on the metal collector. In some cases, a chamber with a ventilation system is a necessity to conduct electrospinning.[79, 80]

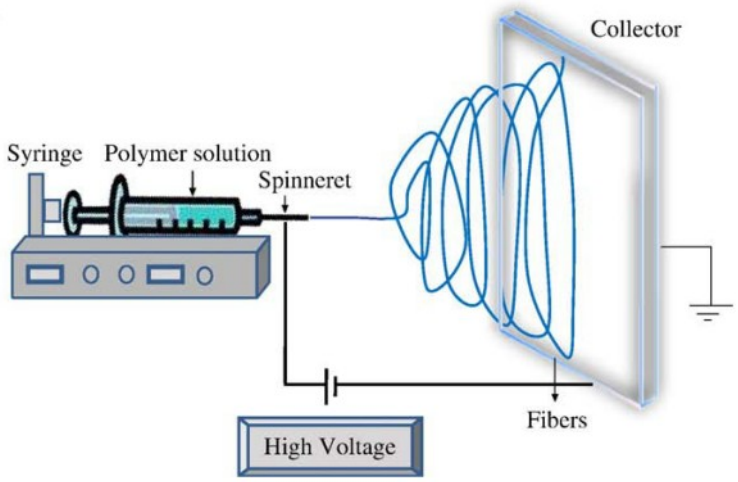

Figure 1-3 Schematic diagram of the set up of horizontal electrospinning apparatus.[81]

When high voltage is applied, the polymeric liquid suffers from two opposite forces: one is surface tension which holds the liquid at the end of the capillary tube, while the other force is electrostatic repulsion which works against surface tension. When the intensity of the electric field is increased, the electrostatic repulsion leads to the elongation of the hemispherical surface of the liquid at the tip of the capillary tube into a conical shape which is also called the Taylor cone.[79] As the electric field reaches a threshold, the electrostatic repulsive force surpasses the surface tension force; a charged jet of the solution is ejected out towards the collector from the tip of the Taylor cone. The solvent evaporates or the melted liquid solidifies rapidly when the polymer jet flies in the air. If the polymer solution can provide sufficient molecular cohesive force, a stable jet is formed and continuous fibers are laid to form a non-woven textile fabric.[79, 80] If not, the polymeric solution breaks into droplets, resulting in electrospraying.

There are many factors influencing the formation, diameter, morphology and mechanical properties of the final nanofibers. These factors come from intrinsic polymer properties (such as molecular weight, molecular weight distribution and architectures), solution properties (i.e. concentration, viscosity, surface tension, conductivity and dielectric constant), process parameters (i.e. voltage, electrostatic field shape, working distance, feeding rate, nozzle diameter) and environmental parameters (i.e. temperature, humidity, air flow).[80, 84] Briefly, these parameters mainly affect the final fibers through chain entanglements, solvent evaporation and forces on the charged jet. Chain entanglements are important to produce a stable jet. Rate of evaporation influences the thinning of the jet and the morphology of fibers. The forces on the spinning jet determine its stretching and bending instability. Fibers with desired properties can be formed by appropriately varying one or more of these parameters.[85]

For different spinning polymers, the spinning conditions are different. For example, for electrospinning poly(ethylene oxide) (PEO) in ethanol-in-water solutions, when the viscosities are higher than 20 poises, the formation of fiber is prohibited due to the high cohesiveness of the solution. When viscosities are lower than 1 poise, electrospraying may happen since a stable jet is not formed.[86] In the case of electrospinning cellulose acetate in acetone/dimethylacetamide solution, the spinnable viscosity range is 1.2 to 10.2 poises.[87]

Diameter is one of the most important fiber properties. Many efforts have been made to correlate the electrospinning parameters with final fiber diameters. Some trends have been found regardless of polymer types. For example, generally, within the spinnable range, a higher

viscosity leads to larger fiber diameter. Since the viscosity is proportional to the polymer concentration in a certain solvent, the higher polymer concentration leads to a larger fiber diameter.[88] Another important factor is the net charge density carried by the electrospinning jet, which is affected by the intensity of the electrostatic field and the conductivity of the polymer solution. In many cases, increasing voltage can reduce the fiber diameter since increasing electric potential at capillary tip enhances repulsive force, resulting in thinner fibers.[89] Also, the addition of extra salt into the polymer solution is observed to increase the charge density of the spinning jet. By adding salt, the elongation forces imposed on the jet is stronger due to the self repulsive forces of the excess charges under electrical field. Thus, adding salt leads to a straighter shape and smaller fiber diameter.[90] Therefore, it is considered that the higher the net charge density is, the more likely it is to obtain smooth fibers without beads.[86]

1.4.2 Protein electrospun nanofibers

It is reported that more than a hundred of polymers has been successfully spun into ultrafine fibers through electrospinning techniques.[80] A variety of electrospun fabrics have also been developed based on biopolymers and their derivatives and composites, such as polysaccharides (i.e. cellulose, chitosan, dextrose, lignin), proteins and DNA.[83] Using biopolymers as electrospinning materials has attracted great attention since biopolymers are renewable resources, biodegradable and biocompatible. However, it is notable that electrospinning of biopolymers can still be challenging since the intrinsic properties of biopolymers such as their molecular weight,

molecular structure, solubility, charge, crystallinity and glass-transition temperature, vary greatly. Also, applications of biopolymer electrospun fabric are needed to be broadened.

Proteins are a major category of biopolymers and protein fibers play important biological functions naturally. However, due to their complex macromolecular structures and strong inter and intra molecular interactions, the process of electrospinning protein is still challenging. In spite of this, much progress has been made recently to prepare protein nanofibers and apply them in medical, food, paper, textile and other industries. Examples include but are not limited to silkworm silk, collagen, gelatin, elastin, casein, wheat gluten and zein.[28, 83, 91] However, their application is limited by poor tensile strength and low water resistance.[92]

In previous work, Wang and Chen[28] have successfully developed electrospun fibers based on plant prolamin zein and hordein in acetic acid. In these novel protein nanofibers, compact zein nanoparticles were incorporated into electrospun hordein network.[28] The conformation of protein molecules in solvent strongly influenced their electrospinnability and the mechanical properties of the final fibers.[93] Wang and Chen[93] found that hordein molecules were unfolded and form an extended and flexible structure in acetic acid. This structure allowed hordeins to form intermolecular interactions more easily during electrospinning. Also, similar to high molecular weight wheat glutelin, hordeins have large domains comprised of repeated sequences and contain β-turn as a structural motif. These structural features allows hordein to possess rubber-like elasticity, which may contribute to the electrospinnability of hordein and the good tensile strength of hordein based electrospun fibers.[94] Meanwhile, zein molecules kept compact

molecular conformation in acetic acid, which acted as reinforced fillers within hordein network.[93] This novel hordein/zein electrospun nanofiber exhibited improved tensile strength and wet stability in both water and ethanol solution. The potential of using hordein/zein electrospun nanofibers in food and biomedical industries has been preliminary justified.[28-30, 95] Although protein electrospun nanofibers have demonstrated many excellent properties, their applications are still limited in food, biomedical and related industries. Further research is needed to develop and broaden their applications.

1.4.3 Applications of electrospun nanofibers

When fiber diameter decreases to nano-scale, the specific surface area increases, leading to the occurrence of some nano-effects, such as increased quantum efficiency, surface energy, surface reactivity, and thermal and electrical conductivity.[83] The small pore size of nanofibers is also important for some applications, such as filtration.[80] The fiber diameter, the pore size between fibers and alignment can be modified to fit desired applications. These interesting features provide electrospun nanofibers potential to be utilized as biomedical devices, supports for enzymes and catalysts, nanofiber-reinforced composites, textile and smart clothes, sensors, templates for materials synthesis, energy devices and electrode materials.[31]

Electrospun nanofibrous materials are considered to be promising candidates to prepare electrode materials for energy storage devices, such as lithium batteries and supercapacitors. This is because electrospun nanofiber textiles possess interesting 3D interconnected pore structure. The

high porosity associated with the nanofiber network leads to rapid transport of ions through the fiber network. Also, the high specific surface area endows electrode with high capacitance.[31, 96] Most attention has been paid to synthetic polymer electrospun fibers for electrodes preparation, such as polyacrylonitrile (PAN), polyvinyl alcohol (PVA) and polyvinylpyrrolidone (PVP).[96] In limited cases, electrospun nanofibers based on biopolymers, mainly lignin [97] and cellulose [98], have been converted into carbon fibers and applied as electrode materials. However, protein based electrospun nanofibers have not been explored in this area yet.

1.5 Applications of protein based electrospun nanofibers as carbon based supercapacitor

1.5.1 Supercapacitors

1.5.1.1 Introduction of supercapacitors

Nowadays, the three major energy storage and conversion devices are batteries, fuel cells and supercapacitors, which have different properties and applications. Supercapacitors have attracted extensive attention in recent years due to their high power density, rapid charging time and long cyclic stability. The specific energy of supercapacitors is several orders of magnitude higher than that of conventional capacitors. Thus, supercapacitors have the potential to fill the gap between batteries and conventional capacitors in terms of power density.[99, 100] Based on the energy storage mechanisms, supercapacitors can be classified into two categories: electric double layer capacitors (EDLCs) and pseudocapacitors.

The energy storage mechanism of EDLCs is similar to conventional capacitors, which was based on the separation of charged species in an electrical double layer across the electrode/solution interface.[101] In EDLCs, the reversible electrostatic accumulation of ions on the surface of porous carbon contributed to their energy storage. An EDLC is comprised of one positive electrode with deficient electrons and one negative electrode with excessive electron. During charging, electrons travel from the negative electrode to the positive electrode through an external pathway. Meanwhile, cations move towards the negative electrode while anions move towards the positive electrode in the electrolytes. During discharging, reverse processes occur.[102] Supercapacitors can store much more energy than the conventional capacitors because of two reasons. Firstly, the distance between separated charges is very small in electric double layer which constitutes the interphase between an electrode and the adjacent electrolyte. Secondly, due to the large amount of pores and high specific surface area, a larger amount of charge can be stored on the electrode surface.[100]

Pseudocapacitors are also called faradaic supercapacitors. In pseudocapacitors, the electrode is electrochemically active and reversible faradaic-type charge transfer happens. When a potential is applied to a pseudocapacitor, fast and reversible faradaic reactions (redox reactions) take place on the electrode materials, which induce the passage of charge across the double layer and result in faradaic current passing through the supercapacitor cell. The way of pseudocapacitors to store energy is similar to the charge-discharge processes in batteries. The capacitance of a pseudocapacitor is determined by the electrochemical charge transfer process that is limited by a

finite amount of electrochemically active materials and/or specific surface.[100] The common electrode materials for pseudocapacitor are transition metal oxides (such as RuO_2, MnO_2 and Co_3O_4) and conductive polymers.[100] There are three types of faradaic processes which may occur in pseudocapacitor electrodes, including reversible adsorption, redox reactions of transition metal oxides and reversible electrochemical doping-dedoping process for conductive polymers.[102] Compared to EDLCs, pseudocapacitors can provide the energy density with one order of magnitude higher. However, pseudocapacitors may have a lower power density since the faradaic reactions involved in the pseudocapacitor systems are slower than nonfaradaic processes.[102, 103] Also, the cyclic stability of pseudocapacitors is poorer due to the redox reactions. Cost of electrode materials also limits the application of pseudocapacitors.

Nowadays, hybrid systems have been developed to utilize the advantages of both EDLC and pseudocapacitors for improved energy-storage performances. Hybrid systems can be constructed by coupling an EDLC electrode with a pseudocapacitor electrode or coupling a supercapacitor electrode with a battery electrode.[102, 104]

1.5.1.2 Cell construction of supercapacitor

Supercapacitors have a sandwich-like structure consisting of two electrodes which are separated by a thin layer of ion permeable separator and immersed inside electrolytes. Usually, a rigid exterior package is used to hold the supercapacitors and prevent possible electrolyte leakage.[100]

Electrolyte is one of the most important elements for supercapacitors. There are mainly three types of electrolytes: aqueous, organic and ionic liquid electrolytes. Aqueous electrolytes, such as H_2SO_4, KOH, Na_2SO_4 and other salt aqueous solutions, provide a high ionic concentration and lower resistance than organic electrolytes. The higher ionic concentration and relatively smaller ionic radius allow supercapacitors containing aqueous electrolytes to have a high capacitance and high power. Additionally, the preparation of aqueous electrolytes is convenient and the cost is relatively low. However, due to the narrow voltage window of water, the major disadvantage of aqueous electrolyte is the small voltage window of about 1.2 V, which strongly limits its energy and power density. On the other hand, organic electrolytes can have a voltage window as high as about 3.5 V. Organic electrolytes are made from organic solvents (such as acetonitrile and propylene carbonate) and organic salts (such as tetraethylammonium tetrafluoroborate and triethylmethylammonium tetrafluoroborate). The issue of using organic electrolyte is that the preparation is strict since water contamination will significantly reduce its voltage window. Ionic liquids are molten salts at desired temperatures. The advantages of ionic liquid electrolytes are low vapour pressure, high thermal and chemical stability, low flammability and even a larger voltage window (2-6 V). Extensive efforts are made to improve the interface properties, temperature range and conductivity of ionic liquid electrolytes.[102, 104, 105]

In additional to electrolytes, electrode materials strongly determine the performance of supercapacitors. Mainly, there are three kinds of electrode materials: metal oxides, conductive polymers and carbon materials. Metal oxide and conductive polymers are mainly used for

pseudocapacitors. Metal oxides can store energy through electrostatic adsorption and also exhibit electrochemical faradaic reactions between electrode and ions. Metal oxides for pseudocapacitors are electric conductive, have two or more oxidation states that coexist without any phase changes. Protons can intercalate into the oxide lattice on reduction. RuO_2 is the most promising candidate. The specific capacitance can reach up to 720 F/g in H_2SO_4 electrolytes, but its high cost strongly limits its commercial applications.[106] Some examples of conductive polymers includes polyaniline (PANI),[107] polypyrrol (PPy)[108] and poly(3,4-ethylenedioxythiophene) (PEDOT) .[109] When oxidation occurs, ions are transferred to the polymer backbone. Ions are released from the backbone into the electrolyte solution when reduction happens.[110] The specific capacitance of polyaniline can reach 775 F/g in H_2SO_4 at the sweep rate of 10 mV/s.[111] Despite the high voltage window and storage capacity, long-term cyclic stability is a problem due to the swelling and shrinking of conductive polymers. One of the methods to overcome this problem is to cooperate conductive polymer nanostructures, such as PANI nanofibers, with carbon materials.[112]

Carbon materials store energy in the electric double-layer at the interface between electrode and electrolyte, thus they are widely used for the assembly of EDLCs. Carbon materials are cost-effective, stable in a wide temperature range, chemically stable and have high specific surface area and good conductivity. Carbon materials can be produced from abundantly available organic materials, such as natural biomass, food waste and by-products of various industries.[104] The structure, pore and surface chemistry of carbon can be engineered. In this thesis research, the

opportunity of using barley protein based electrospun nanofibers into carbon materials for supercapacitor application was explored, which is an approach to open up the utilization of barley proteins in the energy industry.

1.5.1.4 Advantage, applications and challenges of supercapacitors

As compared with the other types of energy storage systems, such as batteries, fuel cells and conventional capacitors, supercapacitors exhibit some advantages. For example, since supercapacitors store electrical charges at the interface or the narrow layer near the surface of the electrode, the rate of charge-discharge process is not restricted to the ionic conduction into the electrode bulk. Thus, supercapacitors, especially, EDLCs have rapid charge-discharge rate and high power density. Since a relatively small amount of energy is lost in the form of heat during charge-discharge cycle, the efficiency of EDLCs is relatively high. Moreover, the low toxicity, safety, good cyclic stability and long shelf life are advantages of EDLCs.[102] Therefore, supercapacitors can be widely used in many areas, such as electric vehicles, electrical tools, portable electronic devices, uninterruptible power supplies and other energy storage systems.[103] However, efforts are still needed to improve the energy density of supercapacitors, which are low (about 5 Wh/kg) as compared with batteries (>50 Wh/kg). Some of the excellent electrode materials for supercapacitors (such as RuO_2) are too expensive to be commercialized. Also, industrial standards are still under construction.[102]

1.5.2 Design of carbon materials for supercapacitor electrodes

Carbon materials store energy in the electric double-layer at the interface between electrode and electrolyte, indicating that the capacitance is determined by the surface area which is accessible to the electrolyte ions. The essential factors contributing to the capacitive performance of carbon materials include specific surface area, pore-size distribution, pore shape and structure, surface functionality and carbon structure.

1.5.2.1 Surface area and pores of carbon materials

Based on the model developed by Helmholtz in 1853, the capacitance of each EDLC electrode can be estimated according to the following equation [113]:

$$C = \frac{\varepsilon_r \varepsilon_0 A}{d}$$

where ε_r and ε_0 is the dielectric constant of electrolyte and vacuum, d is the effective thickness of the double layer and A is the electrode surface area. Therefore, among all the factors, specific surface area and pore size are the two of the most important elements determining the capacitance of EDLCs.

Generally, the increase of specific surface area leads to increased capacitance. Activation of carbon materials can increase the surface area by creating pores at the carbon surface and/or opening pores that are closed, clogged or obstructed.[114] By using different carbon precursor and activation conditions (such as chemicals, temperature, activation time and gaseous environment), the porosity, pore structure and pore size can be controlled.[100] Activation of carbon materials can

be done through physical or chemical treatments. Physical activation modified the carbon surface by controlled gasification and the elimination of volatile pyrolysis products. Usually, physical activation is conducted under oxidising gases such as steam, carbon dioxide, air or gas mixture at 700 to 1000°C. No post-treatment is needed after physical activation. On the other hand, chemical activation is conducted at a temperature of 400 to 700°C with the assistance of chemicals such as phosphoric acid, zinc chloride and potassium hydroxide. The activation process involves the dehydrating action of these reagents. Carbon needs to be washed after activation to remove chemical residues.[100] Over activation may result in thinner pore wall and lower strength of carbon materials. Another approach to increase pores are applying sacrificial templates, such as zeolites or silica.[115]

However, the capacitance is not always proportional to the specific surface area, since not all the pores are accessible to electrolyte ions. The capacitance is also influenced by the relationship between the pore size and the effective size of ions. For aqueous and organic electrolytes, the effective ion size is larger due to the solvation shell. When the pore size is smaller than that of ion, ion sieving effect may happen.[116] Interconnected 3D pore network with hierarchical pores consisting of macro, meso and micropores have attracted extensive attention in supercapacitor applications. Meso and micropores provide the carbon with high surface area resulting in a large capacitance. Meanwhile, the interconnected micro and mesopores facilitate rapid ion transport to ensure high rate capability by working as ion-buffering reservoirs and ion transport pathways.[117]

1.5.2.2 Surface chemistry of carbon materials

In addition to tailoring the pore size and surface area, introducing pseudocapacitance at the electrode/electrolyte interface is another strategy to increase the capacitance of EDLCs. Pseudocapacitance comes from materials such as transit metal oxides, conducting polymers and heteroatoms on the surface of carbon.[104, 118] Addition of heteroatoms into the carbon matrix, such as nitrogen, oxygen, boron and phosphorus, *etc.*, is an efficient way to improve the capacitance of EDLCs through inducing faradaic reaction at the carbon surface without sacrificing the excellent characteristics of carbon materials such as good conductivity, high rate capability and excellent cyclic stability.[119, 120] Nitrogen (N) is one of the most studied heteroatomes in optimizing carbon capacitance. Besides pseudocapacitance, nitrogen functional groups change the electron distribution of the carbon, which enhances the wettability between electrode materials and electrolytes.[119, 121] Generally, there are two approaches to prepare carbonaceous materials rich in N. Firstly, N atoms can originate from the carbon precursor and become part of the chemical structure as a result of incomplete carbonization. Hair,[122] and PPy,[123] which are nitrogen-rich biomass and polymers, are used to prepare carbon materials for supercapacitor electrodes with nitrogen content of 5% and 10% as measured by X-ray photoelectron spectroscopy (XPS). Secondly, N can be incorporated onto the carbon surface through subsequent treatments, such as treating carbon materials with ammonia gas or ammonia solution,[124] urea[120] and/or nitrogen plasma.[125] The post-treatment methods are less preferred due to the toxic gases released during the process and the limited amount of N-functional groups

introduced onto the carbon surface. For graphitic carbon, heteroatoms are located in two kinds of positions: center and edge carbon sites. Functional groups at edges are considered to be more reactive than those in the center as they are often associated with unpaired electrons.[100] There are four configurations of nitrogen present in carbon structure, including pyridinic N (N-6), pyrrolic N (N-5), quaternary N (N-Q) and oxidized N (N-X).[126] N-6 and N-5, which are usually considered to be located at the edge, are the main contributors to the pseudocapacitance by faradaic reactions. N-Q are more likely to be located at the center and can benefit the carbon electrode performance by enhancing its conductivity.[119]

1.5.2.3 Carbon forms

Various forms of carbon materials, such as activated carbon, carbon aerogels, graphite, carbon nanotubes, carbon fibers and carbon onion, have been studied extensively as electrode materials for supercapacitors.[127] For example, activated carbon is the most widely used today due to its low cost and high specific surface area. Highly conductive carbon blacks are usually applied as conductive fillers in many battery and supercapacitor electrodes.[100] Carbon aerogels are highly porous materials prepared by pyrolysis of organic aerogels. Sponge-like Carbon aerogels made from watermelon have 3D flexible structure and achieve 333 F/g with the assistant of Fe_3O_4 at 1 A/g in 6 M KOH.[128]

Continuous carbon nanofibers (CNFs) have shown potential to develop porous electrodes for supercapacitor electrodes which are cost-effective, flexible and property tailorable.[100] Also, the

interconnected pores structure formed by CNF interlacement facilitates the transport of electrolyte. CNFs have low electrical resistance along the fiber axis, but the contact resistance between fibers can be an issue. Interconnected fiber webs can solve this problem by providing shorter and more continuous pathways for electron transport.[129] CNFs can be derived from synthesis and/or natural polymers electrospun nanofibers such as PPy,[123] PAN,[130] lignin[131] and cellulose[118].

Graphitic carbons are considered as all varieties of substances consisting of the element carbon in the allotropic form of graphite (sp^2) irrespective of the presence of structural defects.[132] Carbon precursors decompose and eliminate volatile materials during carbonization. With increasing temperature, condensation reactions occur and local graphitic units begin to grow and become aligned into small graphitic-like microcrystallites, such as 'graphene-like' nanosheets.[100] Graphitic carbon materials are justified by the detection of 3D hexagonal crystalline long-range order through diffraction methods, such as X-ray diffraction (XRD).[132] Porous graphitic carbon, which is a promising supercapacitor electrode material, may present excellent features from both porous carbon and graphene. The porous structure can provide high specific surface area and increase the accessibility of electrolyte to the micropores while the graphitic structure endows the excellent intrinsic electrical conductivity in plane and low resistance pathways for ion transport.[133] The porous carbon with partially graphitic nanostructures derived from resol showed excellent capacitance of 25 $\mu F/cm^2$.[134]

1.5.3 Biomaterials as electrode materials for supercapacitor

In recent years, there is a new trend in recycling natural and industrial wastes to produce carbon for energy storage systems.[127] Biomass materials can be utilized as precursor of carbon materials. These biomasses can be carbonized under inert atmosphere and/or partially carbonized through hydrothermal carbonization methods to be converted into carbon materials. Then, through physical or chemical activation, the surface area and pore size distribution can be further improved.[135] Carbon materials from biomass show excellent capacitance performance, for example, 400 F/g from dead leaves carbon[136], 268 F/g from coconut.[137] Most of these cases are based on lignocelluloses biomass, containing mainly lignin and polysaccharides (such as cellulose, hemicelluloses, starch, chitin and alginate). However, the research on the utilization of proteins, another important category of biomaterials, is still insufficient. Recently, several attempts have been made to employ protein based biomass to produce carbon materials for supercapacitors. For example, human hair,[122] egg shell membrane,[138] collagen,[139] silk fibers[140, 141] and gelatine.[142] The major advantage of using protein based biomass as a carbon precursor is that the large amount of nitrogen on the polypeptide chain can directly endow various nitrogen functional groups on the surface of the final carbon products without any further nitrogen doping process.

After carbonization/activation processes, the intrinsic structures of biomass may be either preserved or lost.[135] It is essential to engineer biomaterials to control the pore texture, structure

and surface chemistry of the final carbons. For example, Lai[131] used electrospinning to turn natural alkali lignin into fibers network and successfully prepared free-standing and mechanically flexible carbon nanofiber mat. Wu *et al.*[128] used watermelon to prepare carbonaceous aerogels containing both carbon nanofiber and nanospheres for supercapacitors.

1.6 Hypothesis and objectives

1.6.1 Summary of the key justifications of this research

Barley is an ancient cereal grain, widely grown around the world. Once upon a time, barley was an important food grain in many areas, but nowadays, it evolved to a feed and malting grain.[16] Currently, 80% of the Canadian barley is used as livestock feed in the domestic market. Around10% of barley production is utilized as malt for beer and whisky production domestically and overseas. In recent years, there is a renewed interest in using barley as food ingredients due to the health benefits of bioactive compounds in barley grains, such as β-glucan, tocols and nonpolar lipids.[16] Commercially available barley products include pot and pearled barley, grits, flakes as well as malt flours. Barley flour and cracked barley can be incorporated into bread and cake formulations.[143] Additionally, barley products can be applied in breakfast cereals, stews, soups, porridge and baby foods.[16, 144] Despite these, barley remains an underutilized cereal for human consumption.[2] Following starch, proteins are the second major component in dried barley grains with a content of 8-15%.[2] Due to the large production of barley, barley is an abundant

source of plant proteins. Thus, exploring human utilization of barley protein can add value to barley and bring more profit to the growers and processors.

Hordeins and glutelins are the major protein components, contributing to 70-90% of total barley proteins. Hordeins are high in Gln, Pro and some hydrophobic amino acids, but low in charged amino acids, resulting in low water solubility.[9] B-hordein, the major fraction of hordeins, contains a large repetitive domain with repetitive pattern of Pro-Phe/Tyr-Pro-Gln,[8] resulting in an extended structure with a high amount of β-turns. Such a structure endows hordein with elasticity and tendency to build up intermolecular interactions, which may contribute to its interfacial behaviour and electrospinnability.

Barley proteins were reported to have foaming, emulsifying, and encapsulating capacities. This can be explained by the high hydrophobic amino acid contents of hordein and glutelin, which makes them capable of adsorbing to the interface. Recently, microparticles from barley proteins have been developed in our group by a pre-emulsifying process followed by microfluidizing without using any organic solvent. Interestingly, hordein formed a solid coating on oil-water interface after high pressure homogenization, which protected the encapsulated neutraceutical from oxidation. This was different from that observed for emulsions prepared by globular proteins, where emulsions only formed soluble aggregates after high pressure treatment. This might be due to the strong tendency of barley protein molecules to develop intermolecular interactions at the interface through hydrophobic interactions.[35] Thus, a cross-linking reagent was not needed to prepare solid barley protein microparticles. However, the detailed mechanism

was not investigated. In addition, these microparticles exhibited the ability to protect the encapsulated lipid phase in SGF and release them under SIF.[27] This was unique as compared to other food protein based microparticles which degraded rapidly in SGF.[145-147] These characteristics might be related to the interfacial properties of the major component B-hordein.[27] However, study on the interfacial properties of barley protein were still lacking. A better understanding on how barley proteins formed a solid coating at the interface and the correlation between protein interfacial behaviour and the particle digestibility will allow us to broaden the applications of barley proteins as well as to design emulsions/particles with desired digestibility.

When particle sizes decrease from micro to nano-scale, some advantages may appear. For example, nanoparticles may improve the bioavailability of nutraceutical compounds. Nanoparticles allow prolonged compound residence time in the gastrointestinal tract and the surface available to interact with biological support increase. Also, nanoparticles have a higher chance to be taken up by cell.[148] Therefore, it would be interesting to adapt this technology to create new nanoparticles from barley proteins for new or improved properties. However, nanoencapsulation system based on barley protein has never been reported.

Another interesting value-added application for barley protein is converting hordein based electrospun nanofiber network into carbon nanofiber as electrode material for supercapacitors. As developed in our previous studies, hordein exhibited good electrospinnability and formed nanofibers through electrospinning without the addition of other synthetic polymers. Also, barley protein based nanofibers showed improved tensile strength and stability in water and ethanol

environment, which surpassed many other protein based electrospun nanofibers.[28, 92] Hordein molecules unfold and have an extended and flexible structure in acetic acid, which helps the formation of intermolecular interactions and the generation of electrospun nanofibers.[93] Electrospun fibres are potential candidates to prepare carbon nanofibers for supercapacitor. Due to the growing market of electronic devices and energy management, there is an increasing demand of supercapacitor. Carbon electrode materials derived from electrospun protein fabric have at least three significant advantages: (1) high content of nitrogen originating from protein contributes additional pseudocapacitance to carbon surface; (2) the fibrous structure provides carbon hierarchical pore structure for electrolyte ion transport and low charge resistance along the fiber axis; and (3) proteins are renewable biomaterials. However, to our knowledge, such research is currently unavailable.

1.6.2 Hypotheses

In the light of these key points, this thesis research was conducted based on the following hypotheses:

Hypothesis 1: B-hordein may form a solid like film at the air-water or oil-water interface upon compression. (Chapter 2)

Hypothesis 2: Conformation and orientation of B-hordein can be changed upon compression to different surface pressures and these conformational changes may subsequently influence its susceptibility to pepsin degradation in the gastric tract. (Chapter 2)

Hypothesis 3: Barley protein may be converted to nanocapsules to incorporate lipophilic bioactive compounds by high pressure technique and such nanocapsules may protect nutraceuticals in harsh gastric juice and target deliver nutraceuticals to small intestine where they are absorbed. (Chapter 3)

Hypothesis 4: Barley protein based electrospun fibers may be converted into nitrogen-doped porous carbon fibers and used as supercapacitor electrode materials. (Chapter 4 and 5)

1.6.3 Objectives

The overall objective of this research is to develop value-added applications of barley proteins. Special focue is placed on barley protein based nanocapsules as nutraceutical delivery systems, and carbon electrode materials derived from barley protein electrospun nanofibers for supercapacitor. This overall objective can be separated into 3 specific objectives:

Objective 1: To study the interfacial properties of B-hordein and to investigate the conformational changes of B-hordein at the interface under compression in relation to the interfacial network degradation in SGF. (Chapter 2)

Objective 2: To elaborate on barley protein based nanoparticles, to study the processing conditions on particle microscopic features and to evaluate their *in vitro* release profile, cytotoxicity and cellular uptake. (Chapter 3)

Objective 3: To develop barley proteins based electrospun nanofibers fabric and to convert them into N-doped carbon fibers with 3D interconnected hierarchical porous structure as electrode materials for supercapacitor. (Chapters 4 and 5)

Chapter 2

Surface Pressure Affects B-hordein Network Formation at the Air-Water Interface in Relation to Gastric Digestibility

2.1 Introduction

Protein-stabilized foams, emulsions and micro/nano-encapsulation systems have received interest from food, personal care, pharmaceutical, petroleum and mining industries due to their remarkable biocompatibility and biodegradability.[64] In addition, proteins can be modified to obtain various structural characteristics and physical properties to fit different applications.[64]

Proteins can be adsorbed to the air-water or oil-water interfaces spontaneously due to their amphiphilic properties and thus reduce the surface tension. Upon adsorption to the air-water or oil-water interface, protein molecules tend to partially unfold and orient to expose their hydrophobic regions towards the air/oil phase, and their hydrophilic regions towards the water phase. As a result of intermolecular interactions, the adsorbed proteins can form a viscoelastic film which stabilizes the emulsion/foam against flocculation and coalescence.[64] Both the conformation and orientation of protein play important roles in determining the properties of the protein stabilized foam, emulsion and micro/nanoencapsulations.[64] For example, the conformation of α-lactalbumin at the interface can impact interfacial protein film thickness and subsequently the physical stability of emulsion.[149]

Emulsions and encapsulation systems with controllable enzyme degradation profiles are desired in many applications, such as controlled-release pesticides in agriculture, food delivery systems, and cosmetic and pharmaceutical products.[147] Increasing interest has been paid to understand the degradation of emulsions in order to strategically design emulsions with different digestion profiles to accommodate various applications.[150] For instance, Maldonado-Valderrama[59] highlighted that different conformations of β-lactoglobulin at the interfaces of tetradecane-in-water and olive oil-in-water emulsions may partially explain the different responses of these emulsions to gastric degradation. However, how protein conformation and orientation affect the digestibility of protein emulsions, in other words, the susceptibility of interfacial protein network to enzyme degradation are still not fully understood.

The conformation and orientation of interfacial protein molecules can be modulated by process conditions.[64] For example, high pressure technologies, such as microfluidization and homogenization, are widely used to produce industrial protein-based foams and emulsions.[64] However, basic understanding on how pressure impacts protein molecular structures and functionalities at the interface is still limited. Lee *et al.*[151] showed that the secondary structures, especially β-sheets and α-helices, significantly changed subsequent to protein adsorption to the interface under high pressure homogenization. Under dynamic conditions, such as homogenization, when oil droplet and/or air bubble size decreases, proteins work in two steps at molecular level to facilitate the formation of foams or emulsions: first by stabilizing the newly formed air-water or oil-water interfaces and droplet structure, and second by rearranging the

molecular conformation to promote a network that inhibits air bubble or oil droplet coalescence.[64] In current study, a Langmuir-Blodgett (LB) protein monolayer was used as a 2D model film to mimic the adsorption of protein molecules to the interface and the formation of an interfacial protein network. Also, this was a practical approach to investigate the protein conformation and orientation changes under mechanical pressure by applying physical stresses to the monolayer through compression of LB trough barriers.[77, 152] During compression, the average molecular area decreased, and protein molecules got crowded, which resulted in strengthened interactions between neighbouring molecules at the interface.[153] The setup of the LB trough was shown in Figure 2-1.

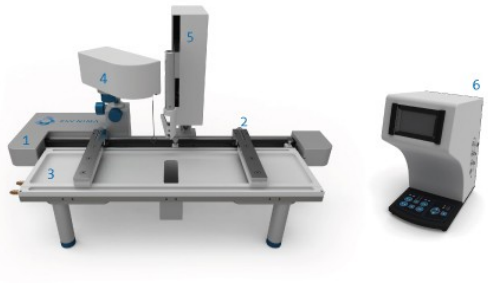

Figure 2-1 Image of LB trough machine setup *(biolinscientific.com)*. 1: frame; 2: barriers; 3: trough top; 4: surface pressure sensor; 5: dipping mechanism for sampling; 6: interface unit.

Barley is one of the most important cereals on earth and hordein is one of the major endosperm storage proteins of barley grain. Due to high content of proline, leucine and valine, hordein is relatively hydrophobic and soluble in 70% ethanol.[8] Hordein can be classified into 4 categories, i.e. B, C, D and γ-hordeins. B-hordein is the dominant group and comprises about 70% of barley prolamins.[8] The amino acid sequence of B-hordein is composed of 5 distinguished domains,

including a non-repetitive N-terminal, a repetitive domain, a non-repetitive domain containing 5 cysteine residues, a region high in glutamine residues and a C-terminal.[8] Among them, the repetitive domain is the major part, composed of half of the amino acid residues. It was reported that hordein has excellent surface functional properties, such as foaming[154] and encapsulating[26]. Wang *et al.*[27] β-carotene micro and nanocapsules have been successfully prepared with hordein by high pressure homogenization. Interestingly, these hordein based micro/nanocapsules exhibited special characteristics, where hordein formed a solid coating on oil-water interface after high pressure homogenization and protect the encapsulated neutraceutical from oxidation. Moreover, the thin protein film attached to the oil droplet surface was resistant to pepsin digestion.[27, 155] These characteristics might be related to the interfacial properties of the major component B-hordein. Thus, in current study, the behaviour of B-hordein at the interface was investigated systematically.

It was hypothesized that the conformation and orientation of B-hordein would be changed upon compression of different surface pressures by LB-trough and these conformational changes will subsequently influence its susceptibility to pepsin degradation. The conformation and orientation of B-hordein films at the air-water interface were analyzed by polarization modulation - infrared reflection absorbance spectroscopy (PM-IRRAS). The use of LB-trough in combination with atomic force microscope (AFM) allowed the visualization the digestion process of interfacial protein network in simplified gastric environment.

2.2 Materials and methods

2.2.1 Materials

Barley grains (Falcon) were kindly provided by Dr. James Helm, Alberta Agricultural and Rural Development, Lacombe, Alberta. Hordeins were extracted from barley grains (Falcon) using an ethanol solution according to a procedure reported elsewhere.[18] In brief, barley flour was defatted by hexane before treated with 70% (v/v) ethanol at 60°C. The supernatant of ethanol extraction was stored at -20°C to precipitate hordein. Hordein was collected by centrifugation and dried at room temperature (25°C). Pepsin (from porcine gastric mucosa, 424 U mg^{-1}) was purchased from Sigma-Aldrich Canada Ltd (Oakville, ON, Canada). Ultrapure water, purified by a Milli-Q Advantage A10 system (EMD Millipore Corporation, MA, USA), was used to prepare buffers. All other chemicals were from Fisher Scientific (ON, Canada) and used as received unless otherwise specified.

2.2.2 B-hordein extraction

B-hordein was isolated from the extracted hordeins by a protein purification system (Gilson PLC 2020,WI, USA) on a Zorbax 300SB-C8 semipreparative column (4.6 X 250 mm) with a linear gradient mixture composed of 0.1% trifluoroacetic acid (TFA) in water and 0.1% TFA in acetonitrile.[156] The acetonitrile and TFA in the collected fraction were removed by rotary evaporation at 60°C. The isolated sample was freeze-dried and characterized by polyacrylamide

gel electrophoresis (PAGE). Only one narrow band was observed in SDS-PAGE. The band was compared with the previous work of Shewry [157] and verified as B-hordein.

2.2.3 Surface tension

The surface tension of B-hordein adsorbed to the air-water interface was measured by the pendant drop technique with an automatic drop tensiometer (Ramè-Hart Instrument Co., NJ, USA) using a method similar to a previous report.[158] The drop profile was fitted to the Young-Laplace equation to obtain the surface tension γ.

2.2.4 Interfacial dilatational rheology

The interfacial dilatational rheology was measured with the same tensiometer aforementioned equipped with an automatic dispensing system (Ramè-Hart Instrument Co., NJ, USA). B-hordein suspensions of different concentrations (0.01, 0.1 and 1 mg/mL) were filled into the tube and needle of the dispensing system. Sinusoidal interfacial area alteration was conducted by precisely controlling the droplet volume. In order to study the change in interfacial dilatational rheology as a function of time, the amplitude and the frequency of the oscillation were fixed as 0.5 μL and 0.1 Hz, respectively. The dilatational modulus (E_d) was calculated by the following equation:

$$E_d = d\gamma/d\ln A = E' + iE''$$

where A is the area and γ is the surface tension of the interface. The storage modulus (elastic modulus, E') is the real part of the dilatational modulus and the loss modulus (viscous modulus,

E'') is the imaginary part. The measurements of surface tension and the dilatational rheology were performed at room temperature.

2.2.5 Interfacial shear rheology

The air-water interfacial shear rheology of B-hordein was measured using a rheometer (HR-3, TA instrument, Delaware, USA) equipped with a Du Noüy ring (a platinum ring with a 19 mm inner diameter and 19.8 mm outer diameter). The interfacial oscillatory shear measurements were conducted according to a method reported previously.[53] In brief, 20 mL of the B-hordein suspension (1.0 mg/mL) was added to a cylindrical glass dish and the Du Noüy ring was placed at the air-water interface with caution. Experiments were conducted at a constant frequency of 0.1 Hz, and the strain was set at 1%, which was within the linear viscoelastic range. The storage modulus (G') and the loss modulus (G") were not dependent on the strain amplitude. The phase lag δ was defined as tan(δ) = G"/G'. The measurements lasted for 2 h and the temperature was kept at 25°C. A plastic cover was used to avoid possible water evaporation.

2.2.6 Surface pressure – area (π-A) isotherm and interfacial protein film deposition

A Langmuir-Blodgett Deposition Trough (KSV NIMA Biolin Scientific, Espoo, Finland) was used to measure the π-A isotherm of B-hordein at air-water interface and to deposit the protein films. The surface of the trough was 98 cm^2. The surface pressure was monitored using the Wilhelmy plate method. Surface pressure (π) was defined by the following equation: $\pi = \gamma_0 - \gamma$, where γ_0 is the surface tension of the subphase without contamination and γ is the surface tension

of the subphase loaded with protein solution.[49] B-hordein was dissolved in 70% ethanol solution with 10 mM acetic acid to obtain a concentration of 1 mg/mL. Using ethanol solution helps to spread B-hordein molecules evenly at the subphase surface and form a monolayer in LB experiments. Phosphate buffer (50 mM, pH 7.0) filtered using a 0.22 μm filter was used as subphase. The cleanliness of the subphase surface was checked and confirmed by compressing the surface with the compression barriers and monitoring the surface pressure. If the surface pressure is below 0.3 mN/m, the subphase meets the cleanliness requirement. To measure the π-A isotherm, system temperature was maintained at 25˚C. The protein solution was spread to the air-water interface by using a 50 μL microsyringe (Hamilton, Reno, USA) following a well-established method.[159] The injected volume of protein solution was adjusted to obtain three different surface pressures including 10, 20 and 30 mN/m.[160] The system was allowed to equilibrate for 15 min before the film was compressed at a constant rate of 3 mm/min (equal to 1.5 cm^2/min). The molecular weight of B-hordein is 14.5 kDa which was used to calculate the area per molecule.[8] After equilibrating at selected surface pressure for 15 min, the surface protein film was deposited onto a freshly-cleaved mica surface or gold coated slides (100 nm thick gold coating, Sigma-Aldrich Canada Ltd, ON, Canada) under constant surface pressure condition for further measurements.

2.2.7 *In situ* digestion

The *in situ* digestion was conducted using the same Langmuir-Blodgett Trough at 37˚C. The surface protein films were first compressed to selected pressures, and the systems were allowed to equilibrate for 0.5 h. During this period, the LB barriers were controlled by the computer software to maintain a constant surface pressure. Then, 1 M HCl was used to adjust the pH of subphase to 2.0. The system was equilibrated for another 0.5 h, and then 20 μl pepsin (1% w/v) was added to the subphase to initiate the digestion test. All the additions were applied carefully using a microsyringe into the aqueous subphase outside the protein film region confined by the two LB barriers to avoid possible disturbance of the protein film. The surface pressure changes during the digestion process were recorded in real time. The protein film at the air-water interface was sampled after 1 h digestion by depositing it onto mica using the method aforementioned.

2.2.8 Atomic force microscopy (AFM)

The surface morphology and roughness of interfacial protein films before and after digestion were characterized by an MFP-3D AFM (Asylum Research, Santa Barbara, USA) in air. The imaging was carried out in Tapping Mode so as to minimize possible surface damage due to the scanning of AFM tip across sample surfaces. The deposited LB protein films were air dried at 25°C before AFM characterization. To demonstrate the reproducibility of AFM results, each experiment was repeated three times. At least three images were taken from the same protein

film. Images were analyzed by the software of Asylum Research Igor Pro 6.32A. The particle sizes were measured and analyzed by ImageJ software. Particles (n=100) were randomly selected from each image to obtain the particle size. Data were presented as mean ± standard deviation (n = 100).

2.2.9 Polarization modulation - infrared reflection absorbance Spectroscopy (PM-IRRAS)

Protein conformation at the interface was studied by PM-IRRAS spectra, recorded using a photoelastic modulator (HINDS PEM-90, Hillsboro, USA) in conjunction with a Fourier transform infrared (FTIR) spectrometer (Thermo Scientific Nicolet 8700, MA, USA). The detector used in all measurements was liquid nitrogen-cooled HgCdTe (MCT) detector with recommended range between 4000 cm^{-1} to 650 cm^{-1}. The PEM-90 was set to a wavelength of 1700 cm^{-1} and half-wave retardation ($\lambda/2$) of 0.5. The incident laser beam angle was adjusted to 83°. Dual channel-double modulation experiment was used in this study, in which two signals, one for the sample and one for the environment were collected spontaneously. B-hordein protein interfacial film was deposited onto the gold coated slide and dried in air for PM-IRRAS measurement. A bare gold coated slide was applied as a reference. Each sample was scanned 1600 times at a resolution of 8 cm^{-1}. The amide I band was analyzed by the curve-fitting function of the PeakFit software (Systat Software, Inc., CA, USA). A linear baseline was drawn between 1760 and 1590 cm^{-1}. The deconvolution was conducted by using Gaussian Lorentzian functions with an iterative linear least-squares algorithm.[74] First, peak widths and positions were fixed and

the intensities were allowed to change until best estimation was achieved. Then, widths, positions and intensities of all peaks were allowed to vary simultaneously. The fitting was continued until an iteration resulted in a decrease in the least-squares error of less than 5% compared to that of the previous iteration.[161] The deconvoluted component peaks were assigned to specific protein secondary structures and the integrated area of the peak was proportional to the percentage of the specific secondary structure presented in the protein.

2.2.10 Statistical analysis

All experiments were performed at least in three independent batches. The percentages of the secondary structure elements of B-hordein and the average size of B-hordein were presented as mean ± standard deviation.

2.3 Results and discussion

2.3.1 The interfacial properties of B-hordein

The interfacial properties and intermolecular interactions of B-hordein play important roles in the formation of foams and emulsions for various applications, which have been systematically investigated, for the first time, in this work.

2.3.1.1 Surface tension

The adsorption of proteins to air-water or oil-water interface is concentration and time dependent.[53] As shown in Figure 2-2 A, the evolution of surface tension as a function of time

was measured for B-hordein suspensions of three different concentrations (i.e. 0.01, 0.1 and 1.0 mg/mL). For the 0.01 mg/mL suspension, a lag phase was observed in the first 10 min as a result of limited amount of B-hordein diffusing from the bulk solution to the air-water interface.[43] Afterwards, the surface tension decreased slowly and a steady state was not reached even after 120 min, indicating that the air-water interface was not saturated with B-hordeins.[162] At higher protein concentrations (0.1 and 1.0 mg/mL), the surface tension dropped rapidly to 64 and 50 mN/m, respectively, within the first 20 min, followed by a mild decrease until 70 min, and then levelled off. The initial stage corresponded to protein adsorption, whereas the second phase of decrease was mainly caused by conformational changes of the adsorbed B-hordein to adjust to the interface [43] and/or the development of multi-layers of B-hordein.[163] The adjustment of protein structure and orientation at the interface allows protein molecules to interact with each other and build up a 2-D network, which stabilizes the air-water interface.[43] At a protein concentration of 1.0 mg/mL, the surface tension reached 48 mN/m after 2 h. The ability of B-hordein to reduce the air-water surface tension was comparable to other proteins known as good emulsifiers, such as β-casein, lysozyme and β-lactoglobulin.[44, 158, 164]

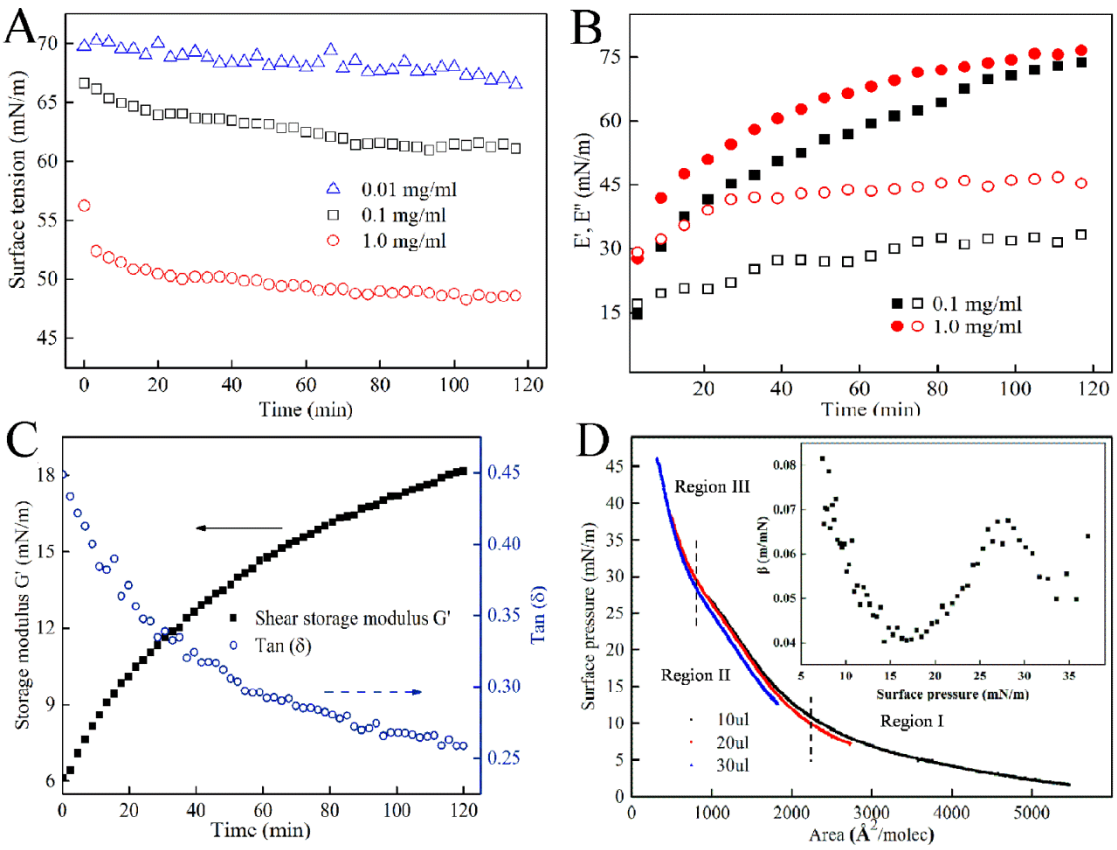

Figure 2-2 (A) Time evolution of the surface pressure of B-hordein of different concentrations at the air-water interface; (B) time evolution of the interfacial dilatational storage modulus E' (solid symbols) and loss modulus E'' (open symbols) for 1.0 mg/mL and 0.1 mg/mL B hordein suspensions; (C) time evolution of the interfacial shear storage modulus G' and the tan(δ) for 1.0 mg/mL B-hordein suspension; (D) surface pressure-molecular area (π-A) isotherms at 25°C at three different loading amounts of 1.0 mg/mL B-hordein solution (10, 20 and 30 μL). Inset is the compression coefficient-surface pressure (β-π) plot for B-hordein.

2.3.1.2 Interfacial rheology

The interfacial rheology has been used to quantify the mechanical properties of adsorbed emulsifier layers at fluid interfaces. During the dilatational rheology measurement, protein molecules that adsorb onto the interface undergo compression and expansion deformation. Measurement of the response of interfacial protein network to such dilatational compression and

expansion can reveal the intrinsic stiffness.[32] Also, the conformation and arrangement of protein molecules at the interface can be inferred by dilatational rheology.[55] At the concentration of 0.01 mg/mL, the E' and E" values were not stable and fluctuated between 0 to 20 mN/m, suggesting that a mechanically elastic interfacial protein network did not yet completely develop (data not shown).[165] At the concentration of 0.1 and 1.0 mg/mL, both the storage and loss modulus increased rapidly within 20 min (Figure 2-2 B), reflecting a quick rearrangement of B-hordein molecules and development of intermolecular interactions at the interface.[32] The loss modulus was similar to the storage modulus in the first 5 min. Then the storage modulus increased quickly and surpassed the loss modulus, whereas the loss modulus remained at a relatively low level, indicating that the B-hordein interfacial films were weakly energy dissipative and predominantly elastic.[166] The rapid increase of the storage modulus in the first 15 min further confirmed the rapid adsorption of B-hordein onto the interface and the development of a densely packed protein network by intermolecular interactions.[167] The dilatational storage modulus continuously increased over 120 min. This stage was reported to be related to the orientation, unfolding and further aggregation of the protein molecules at the interface, which resulted in a strengthened interfacial B-hordein network.[168] After 120 min of oscillation, the dilatational storage modulus reached 74 and 77 mN/m for 0.1 and 1.0 mg/mL B-hordein, respectively. In comparison to many other proteins, such as soy proteins[169], bovine serum albumin[55], gliadin[158] and β-lactoglobulin[170], the elasticity of B-hordein interfacial film ranked among the greatest. This suggests that

B-hordein may possess a relatively rigid internal structure and/or develop stronger intermolecular interactions at the interface.[55]

B-hordein suspension at the concentration of 1.0 mg/mL was selected for the interfacial shear rheology study because it can form an elastic 2D network at the interface as shown by the dilatational rheology. As shown in Figure 2-2 C, the storage modulus of B-hordein protein film increased rapidly over 2 h. The storage modulus was predominantly larger than the loss modulus throughout the whole measurement time range. Also the tan (δ) value remained low, supporting the conclusion that the elasticity dominated the rheological property of the interfacial protein film. For ideal elastic behaviour of an interface, tan (δ) equals to zero. For B-hordein, value of tan (δ) decreased from 0.45 to 0.26, indicating that the protein network at the interface became stiffer and more elastic as the aging time extended. As a comparison, the network of β-casein formed at the air-water interface with a lower shear storage modulus and large tan (δ), was described as a more viscous "gel-like" structure.[162] Due to its high elasticity, the B-hordein interfacial network would be considered as a "solid-like" film.[171] This may be due to the formation of a network through non-covalent intermolecular interaction such as hydrogen bonding and hydrophobic interactions.[172] This is in accordance with the findings of Wang *et al.*[35] that hordein exhibited solid-like behaviour at the water-oil interface, although the stress used in the interfacial shear rheology measurement was significantly less than that employed during a real emulsification process.

2.3.1.3 π-A isotherm

The π-A isotherm obtained by the Langmuir-Blodgett trough experiment provided valuable insight into the structural characteristics and the molecular interactions of B-hordein films.[173] Physical stress was applied to the protein film at the interface through constant compression of the trough barriers. Consequently, the conformational changes and the intra/intermolecular interactions induced by this mechanical stress would be indicated by the slope changes of the π-A isotherm. The π-A isotherm might be used to interpret the corresponding behaviour of the protein under dynamic conditions such as high pressure treatment.[152, 153, 174]

As presented in Figure 2-2 D, three regions were observed on the B-hordein π-A isotherm. By comparing the three π-A isotherms obtained by loading with different amounts of B-hordein (1.0 mg/mL, 10, 20 and 30 μL), the corresponding molecular area regions of the three isotherms coincided. This meant that no or only very small amount of B-hordein was lost to the bulk solution upon spreading and compression. The high surface hydrophobicity of B-hordein contributed to its low solubility in water and high affinity to the interface.[174] For proteins with a high solubility, it is difficult for the protein to be spread to the interface without much loss into the subphase and get a true area/molecule value.[175] As shown in Figure 2-2 D, in the first region, the molecular area decreased significantly, while the surface pressure just slightly increased. In this low surface pressure region, each protein molecule occupied a large area at the interface. Upon further compression, the surface pressure rose rapidly from 10 to 25 mN/m in the second region where B-hordein molecules switched from an expanded liquid phase to a condensed

liquid phase [176]. This is in agreement with the model built up previously, suggesting that molecules experienced several phases upon compression, from gaseous phase at large molecular area to liquid expanded, liquid condensed, solid and collapsed phases at highly condensed molecular area.[177] Furthermore, another slope change was observed upon continuous compression to above 27 mN/m on the B-hordein π-A isotherm. In order to better characterize this phase transition, the surface compressibility was introduced. The compressibility coefficient β of the B-hordein interfacial film at a constant temperature (T) was calculated from the π-A isotherm according to the following equation[178]:

$$\beta = \left(-\frac{1}{A}\right) \times \left(\frac{\delta A}{\delta \pi}\right)$$

By plotting the β-π curve (inset of Figure 2-2 D), the phase transition can be better displayed. The peaks at about 27 mN/m on the β-π curve represented the largest compressibility of the protein film, which may be attributed to the alteration of the protein structure and maximization of the intermolecular interactions.[175] This phase transition to a more solid-like structure of the B-hordein interfacial film is correlated to high storage modulus and low tan (δ) value of the adsorbed protein film as exhibited in the abovementioned interfacial shear rheology results. Langmuir[159] interpreted this change as the transition from liquid film to a gel-like solid film. This phase transition was not commonly found in protein emulsifiers. For example, the interfacial protein film collapsed upon further compression after condensed liquid phase for bovine serum albumin[173] and ovalbumin.[175] High molecular-weight wheat glutenin subunit 1D×5 monolayer at the air-water interface was another plant protein showing a similar phase transition.[174] But, the

B-hordein provided a much higher surface pressure than the wheat glutenin subunit 1D×5 at a similar area per molecule, indicating that B-hordein was more surface active and had the capacity to rearrange and interact with each other to adapt to very small molecular area.[179]

2.3.2 B-hordein orientation and conformation at the interface by PM-IRRAS

The alteration of protein conformation and susceptibility of the protein film to pepsin digestion maybe correlated; however, more information is needed to understand the details of such a mechanism.[58] The surface selection rule leads to the high sensitivity of PM-IRRAS to the orientation of the transition moment at the interface, which makes it suitable to analyze the conformation and orientation of the interfacial protein molecules.[74, 75] Thus, PM-IRRAS was employed to monitor the B-hordein conformation and orientation changes at the air-water interface under different surface pressures.

Figure 2-3 showed the PM-IRRAS spectra (1800-1400 cm^{-1} and the amide I band) with fitted deconvoluted peaks. The percentage of each component and their correlated secondary structures were summarized in Table 2-1. B-hordein PM-IRRAS spectra exhibited three major bands from 1800 to 1400 cm^{-1}, referring to the amide I (1700-1600 cm^{-1}), amide II (1600-1500 cm^{-1}) and CN vibration band (1500-1400 cm^{-1}). The band at 1450 cm^{-1}, which had similar intensity as amide II, was not commonly found in protein IR spectrum. According to previous studies based on gliadin and polyproline,[77, 180] this band could be assigned to the CN vibration in proline residues due to the high proline content of B-hordein (~18%).[8] Due to the surface selection rule, the transition

moments lying parallel to the surface plane show positive bands while the perpendicular transition moments contribute to the negative bands.[77] Thus, the positive bands of B-hordein films were attributed to the amide chains lying parallel to the interface. Due to the selection rules, in PM-IRRAS spectra, the intensity ratio of amide I and amide II is sensitive to the protein orientation because the dipole moments of these two bands are approximately perpendicular to each other.[181] For the B-hordein interfacial film, the intensity ratio of amide I/II decreased from 6.17, 5.14 to 4.15 upon compression from 10 to 30 mN/m. The low intensity of amide II band and the high amide I/II ratio was not commonly found among spectra reported for other proteins. The only comparable example was α-gliadin whose amide I/II ratio was reported to be 7.[77] The contamination of TFA might contribute to the intensity of amide I. However, most of the TFA was removed from B-hordein sample before freeze-drying by evaporation. The low intensity of amide II band might be explained by the reason that α-helix structure orientated flat and parallel to the surface plane when in expanded liquid phase.[182] [183] Upon compression, the α-helix tilted towards the normal of the surface, leading to a decrease of the amide I/II ratio. The change of the amide I/II ratio showed that the interfacial protein molecules rearranged to adapt to the environment with low molecular surface area and high surface pressure. Additionally, the shadow shoulder at 1585 cm^{-1}, corresponding to the antisymmetric COO- stretching vibration in the glutamic acid residue (Glu) side chains, strongly decreased when the protein film was compressed to 30 mN/m.[184] The decrease revealed that the glutamic acid residue may tile towards the perpendicular position of the plane of the air-water interface.[78] This also indicates

that the interfacial B-hordein molecules changed their orientation to adapt to the smaller molecular area upon compression. Notably, the glutamic acid residues, which are hydrophilic, are more likely to be exposed towards a hydrophilic environment, the aqueous phase. This may result in energy reduction and stabilization of the air-water interface.

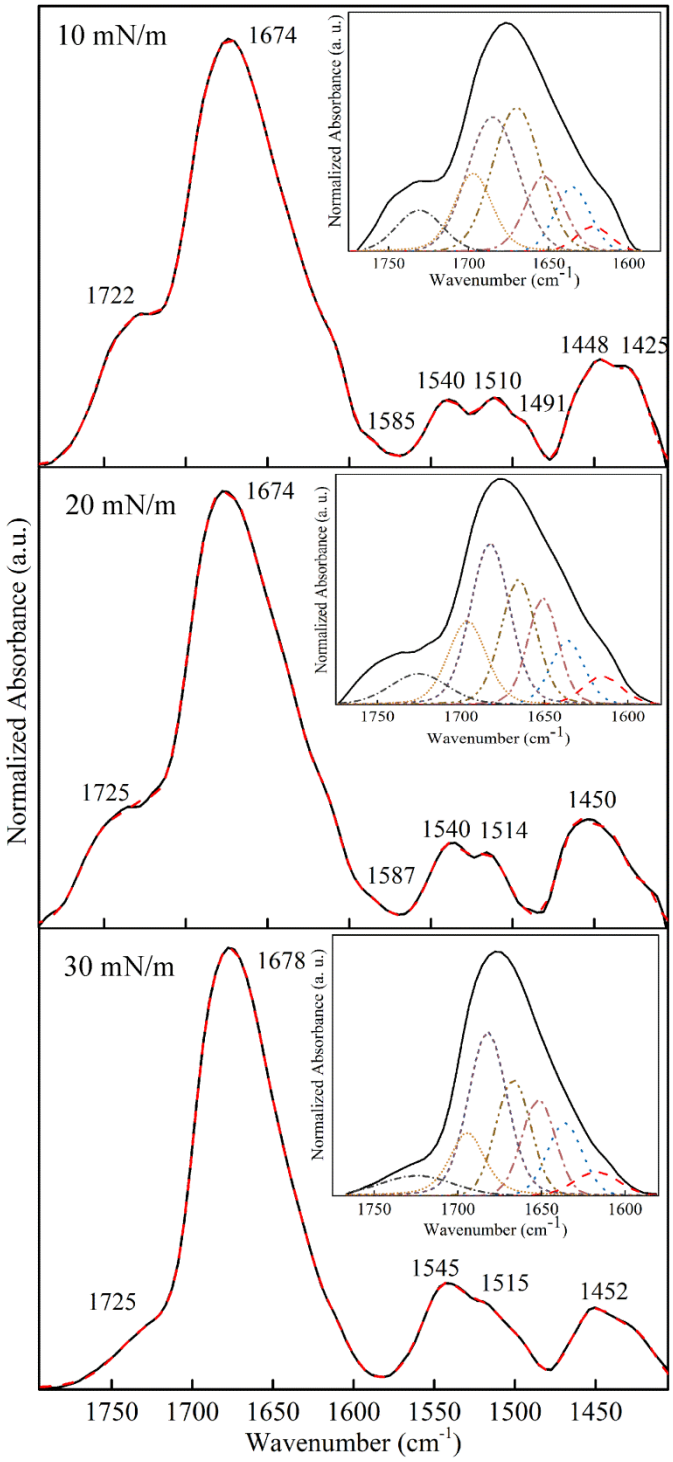

Figure 2-3 PM-IRRAS spectra of B-hordein at the air-water interface: 10 mN/m, 20 mN/m and 30 mN/m. Inset shows the deconvolution of amide I band.

Furthermore, the peak located at 1510 to 1514 cm^{-1} was assigned to the tyrosine (Tyr) ring vibration, which continuously decreased as the surface pressure increased. A decrease in this peak showed that the tyrosine ring might orient towards the normal of the air-water interface. Also, the shoulder at around 1491 cm^{-1}, assigned to the tryptophan (Trp) residues (the C=C stretching vibration coupled with C-H bending vibration), decreased under compression to 20 and 30 mN/m.[78] As mentioned above, Tyr and Trp residues are located in the repetitive domain[8] which is the major part of B-hordein. The movement of the Tyr and Trp may be an indicator of the reorientation of the major repeated sequence. Due to the hydrophobic nature of the repetitive domain,[8] it is not likely to be exposed to the aqueous phase.[34] It might either be covered by the hydrophilic amino acid region or tiled from the air-water interface to the air phase.[78]

Table 2-1 Percentage of the deconvoluted amide I band components and their corresponding secondary structures of B-hordein at air-water interface. Data were presented as mean ± standard deviation (n=3).

B-hordein 10 mN/m		B-hordein 20 mN/m		B-hordein 30mN/m		Peak assignments
Position/cm^{-1}	Percentage/%	Position	Percentage	Position	Percentage	
1620-1624	2.9 ±0.8	1617-1622	2.0±0.4	1616-1619	3.0 ±0.3	β-sheets
1635-1638	9.1 ±0.9	1635-1637	8.9±0.1	1634-1635	9.8±1.3	β-sheets
1652-1655	12.2±0.4	1651-1652	16.0 ± 1.0	1652	15.2 ±1.7	α-helix/ unordered
1666	26.5±2.1	1666-1667	19.9±3.3	1667-1668	21.2±0.3	β-turns
1681-1683	28.7±1.6	1682-1683	38.3±3.2	1682-1685	40.6±2.9	β-sheets/ β-turns
1692-1695	14.2±1.4	1689-1693	12.9±0.1	1693	6.2 ± 1.0	β-sheet/ β-turns
1734-1734	6.5 ±2.5	1723-1743	1.9±1.3	1724-1725	4.0±0.3	Glu side chains

Peak assignment information was from references 77, 181, 185.

The deconvoluted amide I region of B-hordein gained from the air-water interface possessed 7 major bands: 1617 cm^{-1} (β-sheet), 1632 cm^{-1} (β-sheet), 1650 cm^{-1}(α-helix), 1666 cm^{-1} (β-turn), 1682 cm^{-1} (β-sheet), 1693 cm^{-1} (β-sheet/β-turn) and 1720 cm^{-1} (the Glu side chain).[77, 181, 185] The major bands for B hordein at the air-water interface were at 1682 and 1666 cm^{-1}, which were assigned to β-sheets and β-turns, respectively. When surface pressure was changed from 10 to 20 mN/m, a significant decrease in β-turn (26.5 to 21.2%) was observed. High percentage of turn structure indicates a low folded-status of protein molecules.[77] Thus, this suggests that the protein might refold progressively under compression. The slight increase in the α-helix structure (12.2 to 15.2%) also indicated that the B-hordein was re-organized upon adsorption at the interface. Meanwhile, the peak assigned to β-sheet/β-turn at around 1680 cm^{-1} had a substantial increase from 29% at 10 mN/m to 41% at 30 mN/m. Anti-parallel β-sheets contributed to the split peaks at 1619 and 1680 cm^{-1} while the peak at 1630 cm^{-1} was due to the parallel β-sheets.[186] Short peptide segments of twisted or coiled β-sheet strands or small β-hairpin structures rather than extended anti-parallel β-sheets contribute to the 1680 cm^{-1} peak.[187] B-hordein with a large amount of proline is likely to form turns rather than large extended β-sheets because the proline side-chain is locked into a small ring that restricted flexibility, and it bent back again to the main chain.[188] However, short β-sheets could still be developed between turns and contribute to the re-organization of protein molecules at the interface upon compression. The peak at 1680 cm^{-1} was also referred to intermolecular β-sheets as reported previously.[77, 151] Development of such interactions upon protein adsorption at the interface contributed to the growth of a homogenous

and elastic 2D protein film at the interface.[151] The increase of β-sheets was also observed for lysozyme when compressed from 1 to 20 mN/m, changing from liquid expanded phase to liquid condensed phase.[78, 189] The amount of β-sheets developed in lysozyme monolayer during compression was less than that in B-hordein. The dilatational modulus and the shear modulus of the lysozyme interfacial film was also less than those of B-hordein at the same concentration.[53] From these two results, it was deduced that the interaction developed by intermolecular β-sheets could be one of the most important factors contributing to the interfacial properties of the protein monolayer. These conformational changes allowed interfacial B-hordein to develop intermolecular interactions, which subsequently contributed to the formation of elastic 'solid-like' B-hordein interfacial films.

2.3.3 The morphology of B-hordein at the air-water interface

2.3.3.1 The morphology

AFM was employed to observe the morphology of the B-hordein films formed and deposited at different surface tensions (Figure 2-4). The protein film deposited at 10 mN/m showed homogeneous morphology. B-hordein molecules showed disc-like structure and the average size was 20.1 ± 4.5 nm (mean ± standard deviation). B-hordein molecules were apart from each other. According to the result of π-A isotherm, the protein film at 10 mN/m was still at expanded liquid region, so the film was not compact yet. At 20 mN/m, protein film started to become compact and protein aggregates were observed due to a decrease in the surface area. The protein

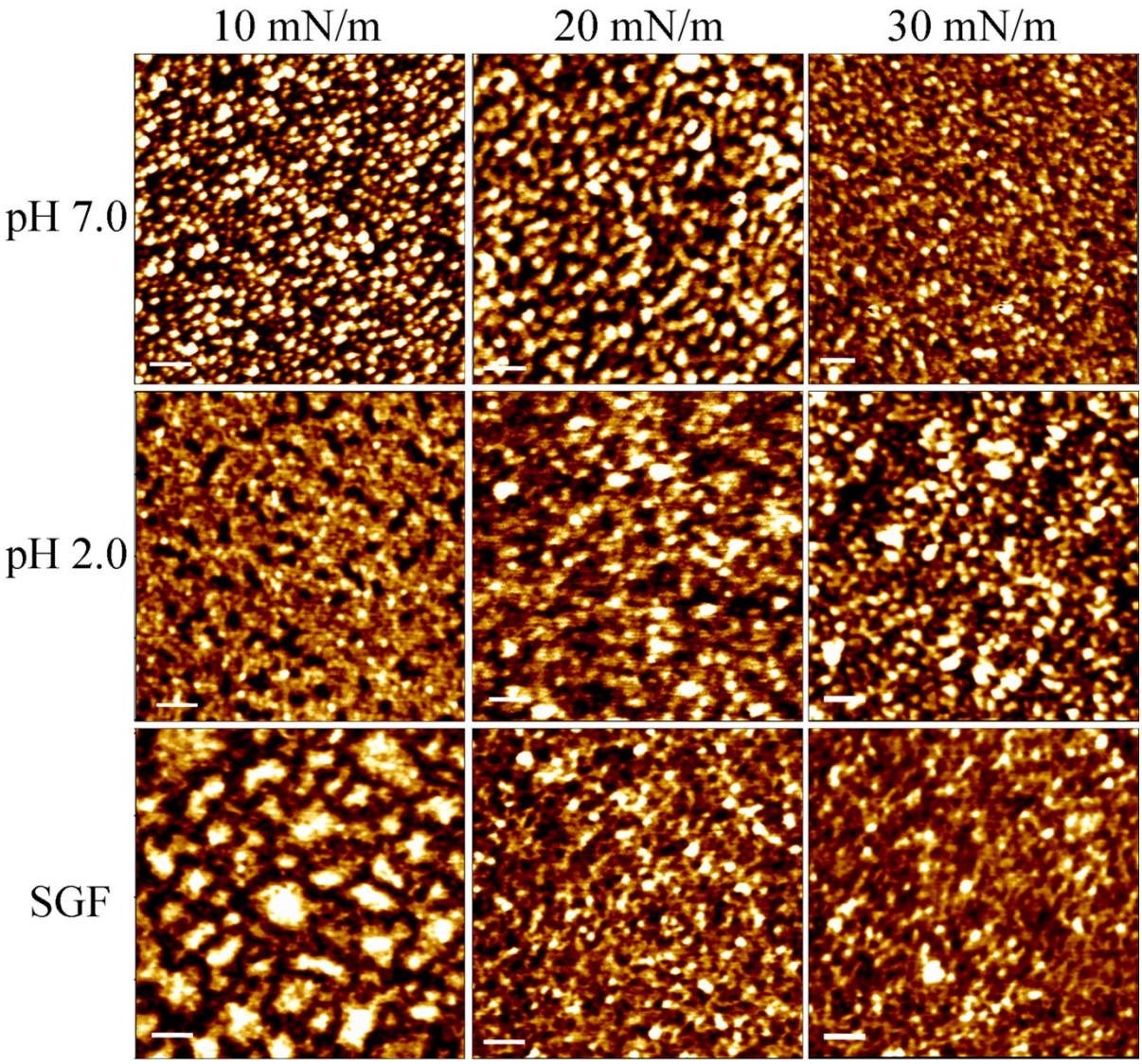

Figure 2-4 AFM images of the B-hordein films formed at 10, 20 and 30 mN/m after incubation at pH 7.0 (25˚C), pH 2.0 (37˚C) and in simulated gastric fluid (SGF, pH 2.0, 37˚C and pepsin). The scale bar is 100 nm. The AFM images exhibit vertical brightness ranges of 1.1 nm in this study.

aggregates were not connected to each other, confirming that the protein film was within condensed liquid region.[190] At 30 mN/m, the protein film became uniform, but much more compact with a low root-mean-square (rms) roughness of 0.2 nm. The low roughness of the protein film indicated that the protein film had a homogeneous height. Protein molecules were

more closed to each other. Collapse and wrinkle were not observed. The compact protein network corresponded to the phase transition from condensed liquid to solid-like film as shown in the π-A isotherm, which may also explain the high storage modulus showed by interfacial dilatational and shear rheology properties.

2.3.3.2 In situ digestion of the B-hordein films

The gastric environment (acidic pH, body temperature and pepsin enzyme exposure) may strongly modify the structure and integrity of the interfacial protein film. This may consequently influence the stability of the emulsion.[64] A major challenge to use protein stabilized emulsions as oral delivery systems is that they are prematurely degraded by gastric enzymes before reaching their absorption site. Firstly, the *in situ* digestion was conducted at pH 2.0 and 37^{o}C without pepsin. After 1 h incubation, morphology of the protein film prepared at 10 mN/m underwent significant changes. Some areas lower in height as indicated by darker color appeared on the AFM image. In AFM topographic images, the color corresponds to the vertical height. In this study, the topographic images exhibited vertical brightness ranges of 1.1 nm. One of the possible reasons for these phenomena may be the loss of protein molecules from the interface due to increased B-hordein solubility when the pH of the subphase was 2.0, which was far from the isoelectric point (pI) of hordein (pI is about 5.6).[174] The height and roughness of the interfacial protein film prepared at 20 mN/m remained similar as to those at pH 7.0. The particle size and height of the protein film prepared at 30 mN/m did not change significantly. By comparing films

incubated at pH 2.0, the B-hordein films formed at higher surface pressure were more resistant to gastric pH. As mentioned above, upon compression to 30 mN/m, the limited space between adjacent adsorbed B-hordein molecules allowed the building up of intermolecular interactions, which outstrip the electrical repulsion of charged amino acid residues at pH 2.0.[187] Moreover, the connections between molecules restricted the protein conformation and orientation change, which made B-hordein hardly dissolved in low pH buffer.[187]

Samples were further tested in the simulated gastric fluid with pepsin. As shown by AFM, protein film prepared at 10 mN/m changed after 1 h of incubation in SGF with pepsin. By comparing the B-hordein film incubated at pH 2.0 and in SGF, the pepsin digestion likely occurred. The rms roughness of the remaining protein film increased from 2.2 to 2.5 nm, indicating that the protein molecules might have slightly rearranged and stacked together to become more condensed. The protein films prepared at 30 mN/m remained uniform and compact after being treated with SGF. This suggests that B-hordein films compressed at a higher surface pressure were resistant to pepsin digestion even at relatively small thicknesses. As mentioned above, the hydrophobic domain of B-hordein tended to avoid the water phase upon compression, thus was "locked" in the compact solid-like film networks, which limited the accessibility of pepsin to the hydrophobic repetitive region.[191] Since pepsin was reported to preferentially bind to the hydrophobic site on the peptide before hydrolysis,[192] the digestion activity of pepsin on the protein film prepared at high surface pressure was inhibited.

2.4 Conclusions

In this work, the surface activities of B-hordein were systematically investigated for the first time. A B-hordein suspension could reduce the air-water surface tension rapidly to ~45 mN/m and form a solid-like coating at the interface. As compared to some other food proteins reported in the literature (such as soy proteins and whey proteins), the interfacial B-hordein film had high elasticity and compressibility. This made B-hordein a promising emulsion or foam stabilizer. Also, it is the first example to reveal how compression impacts protein interfacial network formation in relation to protein digestibility. When compressed from 10 to 30 mN/m, large amount of intermolecular β-sheets was developed, which contributed to the formation of the elastic B-hordein film at the interface, resulting in a low digestibility at stomach pH. Also, the major hydrophobic repetitive section of B-hordein titled away from the aqueous phase, which decreased its affinity to pepsin binding and reduce pepsin digestion. Thus, when compressed at 30 mN/m, a very strong elastic network was formed at the interface resistant to harsh gastric environment. B-hordein has the potential to develop encapsulations of bioactive compounds capable of bypassing the stomach intact and reaching small intestine for absorption. Generally speaking, the findings of this study can be widely applied in various industries to better utilize proteins as natural emulsifiers and micro/nano-encapsulation materials to obtain desired properties.

Chapter 3

Elaboration and Characterization of Barley Protein Nanoparticles as an Oral Delivery System for Lipophilic Bioactive Compounds

3.1 Introduction

Increasing scientific evidence has shown that bioactive compounds, such as polyunsaturated fatty acids, phytosterols, carotenoids and vitamins, have the potential to reduce the risk of chronic diseases and improve public health. Their efficacy depends on the dose, the preserved biological activity and the bioavailability.[193] However, many lipophilic bioactive compounds exhibit low bioavailability due to insufficient residence time in the gut, or low permeability and/or low solubility within the intestinal tract, which can limit their potential activity *in vivo*.[148] For example, of the total amount of carotenoids found in fruits and vegetables, only a small proportion is bioavailable.[194] These compounds exhibit antioxidant activities which can protect cells against oxidation to reduce the risk of cardiovascular disease, cancer, and aging-related diseases. Nanoencapsulation of nutraceuticals is emerging as a promising approach for delivering health promoting substances to wide populations without harming the sensory quality of food, while providing benefits of protection and improved bioavailability. Nanoparticles can dramatically prolong the formulation residence time by decreasing the influence of intestinal clearance mechanisms and by increasing the surface area to interact with the biological support. In addition, some of them are small enough to cross the epithelial lining of the gut and are

readily taken up by cells, allowing efficient delivery of active compounds to target sites in the body.[195] However, the application of nanotechnology in the food industry is still limited due to the lack of effective food grade materials along with safe and economic processing.[196]

Food grade proteins are interesting materials for nanoparticle preparation due to their excellent biocompatibility and biodegradability, as well as unique properties in forming gels, emulsions, and emulsion gels, thus offering the capacity of incorporating both hydrophilic and lipophilic bioactive molecules until release at the functional site. In spite of the promising potential, there are several formidable challenges which have to be overcome before they can be widely used as nutraceutical delivery systems. Firstly, nanoparticles prepared using protein materials involve processing such as emulsification-solvent evaporation, chemical or heat-induced crosslinking and coacervation. These normally demand heating and/or organic solvents, which cannot be applied to heat-labile bioactive compounds and may cause concerns about the potentially toxic residuals.[195] Secondly, feasible processing conditions for mass production of stable protein-based nanoparticles are lacking. In many cases, small molecule surfactants are required to stabilize food protein nanoparticles,[197] which may result in controversies about their health risks. Moreover, due to the digestibility of food proteins in gastric environments and the high surface-to-volume ratio of nanoparticles, the incorporated nutraceuticals are normally released rapidly in the stomach, resulting in a limited amount of nutraceutical compounds that can reach small intestine where they need to be absorbed to exert health benefits. Therefore, new protein materials and feasible processing conditions are required to address these challenges.

Barley proteins are one of the most abundant and inexpensive natural food protein sources. The major fractions are hordein (about 45 wt%) and glutelin (4 to 45%). Due to their unique molecular structures and high content of hydrophobic amino acid residues, barley proteins has been demonstrated good foaming,[21] emulsifying,[21] and film forming[23] capacities. Recently, microparticles from barley protein have been developed in our group by a pre-emulsifying process followed by microfluidizing without using organic solvent or cross-linking reagents. In addition, these microparticles exhibited the ability to protect the encapsulated lipid phase in simulated gastric fluid and release them under simulated intestinal conditions.[27] Therefore, it would be interesting to adapt this technology to create new nanoparticles from barley proteins for new or improved properties. This work aims to elaborate on barley protein based nanoparticles and study the impact of processing conditions on particle microscopic features including size, size distribution, morphology and surface charge. Subsequently, the *in vitro* release properties of the optimized barley protein nanoparticles were tested in the simulated gastro-intestinal tract using β-carotene as a model bioactive compound. Cytotoxicity and cellular uptake were also evaluated preliminarily by the Caco-2 cell model to study their biocompatibility and efficacy.

3.2 Materials and methods

3.2.1 Materials

Barley flour was milled from pearled barley grains (Falcon), which was kindly provided by Dr. James Helm, Alberta Agriculturel and Rural Development, Lacombe, AB, Canada. Barley

protein was extracted from barley flour by alkaline solution according to methods previously established [18]. Briefly, after pearling and milling, barley flour was passed through a sieve with mesh size of 0.08 mm. The barley flour was extracted by alkaline solution (pH 11.5). Then, the pH of supernatant from alkali extraction was adjusted to 5.4 to precipitate the barley protein. The protein content was 90 wt% (dry basis) as measured by combustion with a nitrogen analyzer (FP-428, Leco Corporation, St. Joseph, MI, USA). The canola oil used in the present work was purchased from a local supermarket. β-Carotene, pepsin (from porcine gastric mucosa, 424 U/mg), pancreatin (from porcine pancreas), 3-(4,5-Dimethylthiazol-2-yl)-2,5-diphenyltetrazolium bromide (MTT), dimethyl sulfoxide (DMSO) and Nile Red were purchased from Sigma-Aldrich Canada Ltd (Oakville, ON, Canada). Alexa Fluor dyes, 4',6-diamidino-2-phenylindole (DAPI) and mounting medium were from Life technologies (Burlington, ON, Canada). Other cell culture reagents including Dulbecco's Modified Eagle Medium (DMEM), fetal bovine serum (FBS), non-essential amino acids (NEAA), HEPES solution, trypsin-EDTA and Hank's balanced salt solution (HBSS) were purchased from GIBCO (Burlington, ON, Canada). Human colorectal adenocarcinoma cell line Caco-2 was purchased from the American Type Culture Collection (ATCC, Manassas, VA, USA). All chemicals used in this work were of reagent grade.

3.2.2 Nanoparticle preparation

Nanoparticles were prepared with barley protein as a coating material and canola oil as lipid phase. β-Carotene (0.05% w/v) was added in the lipid phase as a model lipophilic bioactive compound. The oil phase was added to the aqueous protein suspension, followed by high speed homogenization (30,000 rpm, PowderGen, Fisher Scientific International, Inc., CA, USA) to prepare a coarse emulsion. Then, the pre-mixed emulsion was passed through a high pressure homogenizer (NanoDeBee, Bee International, Inc., MA, USA) to form solid nanoparticles. Different processing pressures (4, 8, 12, 16 and 20 kpsi), recirculation numbers (1 to 6), protein concentrations (2, 3 and 5% w/v) and oil-to-protein ratios (0.2 to 5), respectively, were applied to prepare nanoparticle of various properties as characterized in section 3.2.3. The prepared nanoparticles were stored at 4°C with 0.025% (w/v) sodium azide until use.

3.2.3 Nanoparticle characterizations

The size, size distribution as indicated by polydispersity index (PDI), and zeta potential of the nanoparticles were measured at room temperature (23°C) by dynamic light scattering and laser Doppler velocimetry using a Zetasizer NanoS (model ZEN 1600, Malvern Instruments Ltd, UK). The protein refractive index (RI) was set at 1.45 and dispersion medium RI was 1.33.[27] The nanoparticle samples were diluted to appropriate concentration by phosphate buffer (pH 7) to avoid multiple scattering before analysis. The data were averaged from at least three batches. The storage stability of the nanoparticles was investigated by measuring particle size at different

time intervals during storage at 4°C in dark. Samples were diluted one time with deionized water before storage.

Methods used to quantitatively measure the surface oil percentage and encapsulation efficiency were adapted from Beaulieu, *et al*. [27] with modifications. Pure ethanol (7 mL) was added into 3 mL nanoparticle suspension to break the particles as a major component of barley protein, hordein, is soluble in 60-70% ethanol solution.[27] Then 10 mL of hexane was added and the mixture was shaken vigorously with a vortex mixer for another 1 min and allowed to stand for 1 min. These mixing and standing procedures were repeated twice. The final mixture was centrifuged at 8,000 g for 15 min at 20°C. After centrifugation, 5 mL hexane was transferred to a tube and evaporated under nitrogen to remove the solvent. The remaining oil was weighed to the nearest 0.1 mg. The oil extracted in this method was the oil in the nanoparticle suspension, including the surface oil and encapsulated oil. The surface oil amount was measured by a similar method, but only hexane was added into the nanoparticle suspension. The amount of encapsulated oil can be calculated by the amount of oil in the suspension subtracting the surface oil amount. The amount of oil added into the system before processing was called total oil.

The surface oil percentage was calculated by the following equation:

$$Surface\ Oil\% = \frac{W_{surface\ \ oil}}{W_{surface\ oil} + W_{encapsulated\ oil}} \times 100\% \qquad (1)$$

The encapsulation efficiency (EE) and loading capacity (LC) were calculated by the following equations:

$$EE\% = \frac{W_{encapsulated\ oil}}{W_{total\ oil}} \times 100\% \qquad (2)$$

$$LC\% = \frac{W_{encapsulated\ oil}}{W_{particles}} \times 100\% \quad (3)$$

where, $W_{surface\ oil}$, $W_{encapsulated\ oil}$ and $W_{total\ oil}$ represent the weight of oil attached on the surface, encapsulated in the protein matrix and the total oil added initially. $W_{particles}$ means the dry weight of the particles encapsulating oil inside. Nanoparticle suspension (3 mL) was added to a weighed tube and dried at 85°C. The remaining residues were weighed to the nearest 0.1 mg.

The morphology of the nanoparticles was observed by a transmission electron microscopy (TEM, Morgagni 268, Philips-FEI, Hillsboro, USA) at an accelerating voltage of 80 kV. Nanoparticles were negatively stained by 2% (w/v) sodium phosphotungstate (pH 7.4). One drop of nanoparticle sample was added to a copper grid covered with nitrocellulose and kept still for 3 min. Then, a drop of sodium phosphotungstate (2%, w/v) was applied to top of the nanoparticle droplet on the grid. Excess liquid was blotted from the grid, and then samples were air dried at 25°C.

3.2.4 *In vitro* protein matrix degradation

The *in vitro* protein matrix degradation assays were conducted in simulated gastric fluid (SGF, pH 1.5 with 0.1% w/v pepsin) and simulated intestinal fluid (SIF, pH 7.4 with 1.0% w/v pancreatin). Changes in nanoparticle morphology after incubating in SGF and SIF were observed using the TEM and the samples were treated in the same way as above. The size change of the nanoparticles in the SGF and SIF was also monitored using the Zetasizer NanoS instrument under the same conditions as indicated above.

3.2.5 *In vitro* release properties of barley protein nanoparticles

The release properties of barley protein nanoparticles were also measured in the simulated gastro-intestinal tract. Briefly, nanoparticles (containing 12 mg barley protein) were incubated in SGF at 37°C for 1 h. The digestion was stopped by heating the sample to 95°C for 3 min to inactivate enzymes. The released β-carotene was extracted with hexane and quantitatively determined by reading the absorbance at 450 nm with a UV-visible spectrophotometer (model V-530, Jasco, CA, USA).[198]

After incubation in SGF for 1 h, the pH of the mixture was adjusted to 7.5 with concentrated NaOH. Then pancreatin suspension was added to initiate the digestion and final pancreatin concentration was 1% (w/v). The mixture was incubated at 37°C and samples were taken at different time intervals. The digestion was stopped after 8 h by heating the sample to 95°C for 3 min. The degradation of nanoparticle and release of β-carotene was assessed by a lipid digestion model which was increasingly used to *in vitro* evaluate the lipid-based drug/nutraceutical delivery system.[199] The dynamic lipid digestion was measured through the methods described by Li *et al.* with slight modification. The products of pancreatin lipase were mainly 2-monoglyceride and fatty acids.[200] The released free fatty acid was titrated by 0.1 M NaOH to maintain the pH value at 7.5. The volume of NaOH added was recorded and used to calculate the concentration of free fatty acids generated during digestion. The cumulative released free fatty acid percentage was calculated using the following equations[200]:

$$V_{MAX} = 2 \times \left(\frac{W_{oil}}{MW_{oil}} \times \frac{1000}{C_{NaOH}} \right) \quad (4)$$

$$Free\ Fatty\ Acid\ Released\% = \frac{V_{EXP}}{V_{MAX}} \times 100\% \quad (5)$$

where, W_{oil} is the total weight of oil participated in the digestion (g) and MW_{oil} is the molecular weight of the oil (g per mol). For canola oil, MW_{oil} is 882.1 g/mol.[201] C_{NaOH} is the concentration of NaOH used (0.1 mol/L); V_{Max} is the volume of NaOH used to neutralize all the free fatty acid released from lipid when all the triglycerides were converted into two free fatty acids and one monoglycerides; and V_{Exp} is the actual volume of NaOH titrated during measurement.

3.2.6 *In vitro* cytotoxicity and Caco-2 cell uptake

Caco-2 cells were grown in T-75 flasks at 37°C in a humidified atmosphere of 5% CO_2. The cells were cultured in DMEM supplemented with 20% FBS (v/v), 1% NEAA and 25 mM HEPES. The medium was changed every other day until the cells reached 80% confluence, when the cells were removed with 0.25% trypsin in 1 mM EDTA solution at 37°C for 4-6 min and passaged with fresh medium.

The cytotoxicity of the nanoparticles was examined by MTT assay. Caco-2 cells were transferred onto 96-well plates at a density of 8,000 cells per well in 100 µl culture medium. The cells were grown for 24 h to allow attachment before the experiment. Nanoparticles were added into each well to reach a final concentration of 0.5, 0.25 and 0.125 mg/mL respectively, and incubated with the cells at 37°C for 6 h. 10 µl of MTT solvent (5 mg/mL in PBS) was then added to each well and incubated for a further 4 h at 37°C followed by removal of the medium from each well.

100 µl of DMSO was added to each well and followed by the measurement of the absorbance at 570 nm using a microplate reader (SpectraMax, Molecular Devices, USA). The viability was expressed by the percentage of living cells with respect to the control cells.

The uptake of the nanoparticles by Caco-2 cells was studied using fluorescence-labeled nanoparticles and confocal laser scanning microscopy (CLSM). Briefly, 0.025% (w/v) Nile red was dissolved in canola oil followed by centrifugation at 12,000 g for 10 min and the oil supernatant was used for nanoparticle preparation following the same process above. Caco-2 cells were transferred onto Glass bottom microwell dishes (P35G-1.5-14-C, MatTek Corp., USA) at a density of 1×10^5 cells/dish and cultured for 5-7 days until a confluent monolayer was formed. On the day of experiment, the medium was replaced with HBSS (without phenol red) and allowed to equilibrate at 37°C for 30 min. Following the removal of the buffer, nanoparticle suspension in HBSS at a concentration of 0.5 mg/mL was added and incubated with the cells for 1, 3, 6 h. The cells were then gently washed with PBS 3 times and fixed with 4% paraformaldehyde (w/v in PBS pH 7.2) at 37°C for 15 min. Cell membrane and nuclei were stained with wheat germ agglutinin (WGA) – Alexa Flour 488 conjugate and DAPI, respectively, and the cells were mounted with Prolong Gold Antifade Reagent. CLSM 510 Meta (Carl Zeiss, Jena, Germany) equipped with a diode, an Argon laser and a Helium/Neon laser, providing the excitation at 405 nm, 488 nm and 561 nm, respectively, was used for observation and imaging. Images were processed with ZEN 2009LE software (Carl Zeiss MicroImgaing GmbH, Germany).

3.2.7 Statistical analysis

All experiments were performed at least in three independent batches. Data were represented as the mean of three batches ± standard deviation. For data in figures, error bars showed standard deviations. Statistical evaluation was conducted by Student t-test and analysis of variance (ANOVA) using SAS (SAS Institute, Inc., Cary, NC). The multiple comparisons of the means was performed using Duncan's multiple-range test. Statistical differences between samples were performed with a level of significance at $p<0.05$.

3.3 Results and discussion

3.3.1 Barley protein nanoparticle preparation

For globular proteins such as soy and whey proteins, emulsions are normally generated after high pressure homogenization due to the fact that hydrophilic protein molecules usually form a gel-like viscoelastic thin film outside an oil droplet to stabilize it in aqueous phase.[202] Solid nanoparticles can be derived from its corresponding nanoemulsion through solidifying and/or hardening processes by adding a cross-linking reagent (e.g. glutaraldehyde, transglutaminase), or coacervating with oppositely charged polymers.[203] Interestingly, solid nanoparticles were generated from barley protein stabilized coarse emulsion directly after high pressure homogenization (Figure 3-1 A). Barley protein formed solid microparticles during the micro-fluidization process due to the surface hydrophobic nature of their molecular structures which enabled them to adhere and completely cover the oil droplets rapidly in the pre-emulsion

process.[27] These complexes tended to strongly aggregate due to the hydrophobic surface patches to form thick unruptured coatings after high pressure treatment. The morphology of the nanoparticles was shown by TEM images (Figure 3-1 B). The mean diameter of barley protein nanoparticles ranged from 50 to 200 nm with regularly spherical shapes and smooth surfaces. Figure 3-1 C also showed that small oil droplets were homogeneously trapped inside the protein matrix with honeycomb structure. This type of nanoparticle structure might better carry and protect the interior dispersed phase. Preliminary experiments indicated that processing conditions (number of passes and pressure) and particle formation solution (protein concentration, protein/oil ratio) dictated nanoparticle properties. Since the particle diameter played an important role in their physiological properties,[195] in this work the process parameters were optimized with an emphasis on the particle size and size distribution.

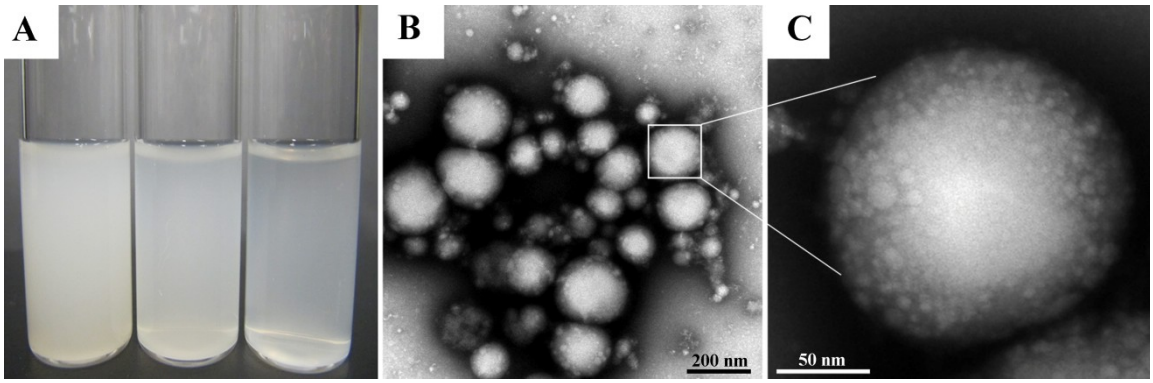

Figure 3-1 (A) Photograph of barley protein nanoparticles (from left to right, the nanoparticle concentrations are 0.2, 0.1 and 0.05 wt%); (B)TEM image of barley protein nanoparticle (2 wt% protein and 2.5% v/v oil) prepared at 16 kpsi with 14 kx magnification; (C) same sample observed with 110kx magnification.

3.3.1.1 The influence of homogenization parameters on the particle size

High pressure homogenization is a kind of high energy input emulsification technique, whose performance strongly depends on the amount of energy supplied to the reaction system. Numerous researches have shown that the particle size could be controlled by changing the pressure and recirculation number under a given set of emulsion compositions.[204] Thus, the effects of these two parameters on particle size were investigated.

Firstly, the particles were prepared with 2% (w/v) protein and 2.5% (v/v) oil under two selected pressures (12 and 16 kpsi) which allowed formation of well-dispersed nanoparticles with spherical shapes. Figure 3-2 demonstrates that with an increase of the recirculation number from 1 to 3, the diameter of particles prepared at 12 kpsi decreased from 494 to 246 nm, while particles prepared at 16 kpsi decreased from 264 to 162 nm. This result is in agreement with previous studies.[205, 206] Increasing recirculation time led to prolonged exposure of nanoparticles in the high pressure emulsification unit, which resulted in stronger energy input and higher degree of oil droplet disruption.[204] Even through a tendency to decrease particle size was observed as the recirculation number further increased, the reductions became modest after 4 passes and leveled off gradually. The smallest mean particle size was 195 nm for 12 kpsi and 147 nm for 16 kpsi after 6 passes. Since the efficiency of particle size disruption was limited by the emulsion composition and other emulsification conditions, it was no longer efficient to minimize particle size by increasing the number of passes. On the other hand, increasing the number of recirculation significantly narrowed the particle size distribution as indicated by decreased PDI

value (inset in Figure 3-2), which was reported to have important effects on nanoparticle applications.[207] PDI of the sample dropped from 0.55 to 0.33 and from 0.43 to 0.25 after 6 passes of homogenization under 12 and 16 kpsi, respectively, indicating that the particle size distribution was acceptably homogeneous after 6 passes, since a PDI value of less than 0.3 indicates a narrow size distribution.[206] This result was expected because a longer energy input duration and a stronger dispersive effect on the oil droplets could be achieved by increasing the recirculation number.[208] Thus, 6 times of recirculation was selected as the optimized condition for further experiments.

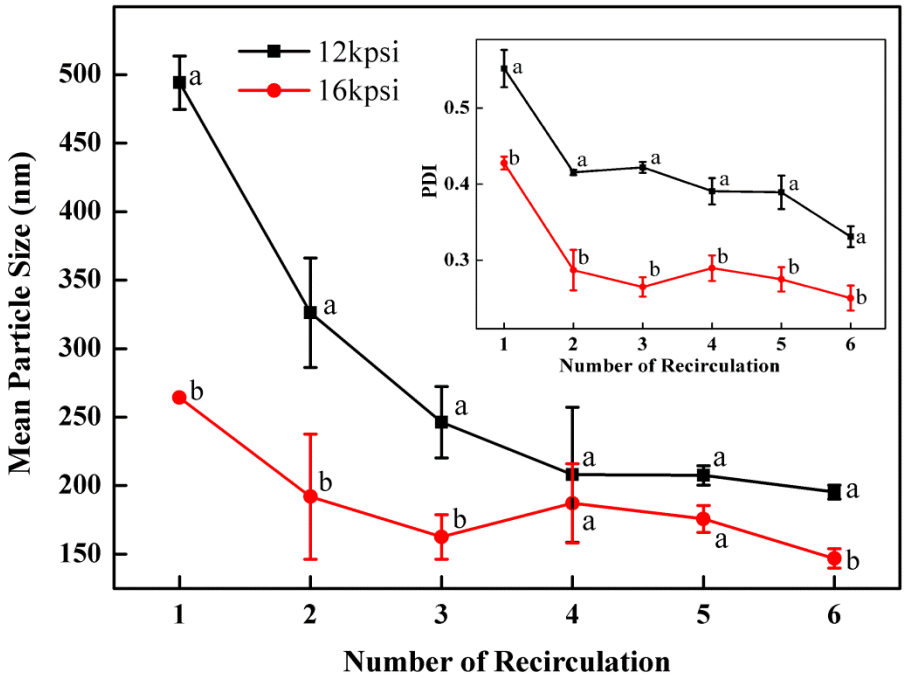

Figure 3-2 Effect of number of recirculation on the mean particle size of samples produced with 2 wt% barley protein and 2.5% (v/v) oil. The inset showed the effect of number of recirculation on particle size distribution as indicated by PDI. Different letters above or below the curve indicate significant difference (p<0.05) due to processing pressure.

The influence of processing pressure on particle size was shown in Figure 3-3. Here the particles were prepared with 2 and 3% (w/v) protein and 2.5% (v/v) oil. When particles were prepared with 2% protein, the mean particle diameter dropped from 339 to 147 nm with increasing homogenizing pressure from 4 to 16 kpsi. Higher pressure input could lead to higher degree of protein unfolding and oil droplet disruption, resulting in smaller particle sizes.[205, 206] On the contrary, samples prepared with 3% protein had modest changes at the tested pressure range, which indicated the emulsion formula significantly influence the particle size as well. An obvious transition point at 16 kpsi was observed for both samples. With pressure rising above 16 kpsi, particle sizes increased significantly. This 'over-processing' phenomenon was also observed in several emulsion systems using biopolymers as emulsifier.[209] During high pressure homogenization, the particle size distribution was determined by the equilibrium between two opposite actions happening at the same time: oil droplet disruption and re-coalescence. The excessive energy input at 20 kpsi might not result in additional protein adsorption to the disrupted oil surface. Inversely, shorter residence time of the emulsion in the emulsifying unit along with other reasons led to a higher re-coalescence rate. Furthermore, higher pressures also produced nanoparticles with more narrow size distributions due to the fact that higher energy input could disrupt the large particles which survived under low pressure. The PDI values decreased from 0.4-0.6 to 0.25 for the selected two samples when pressure increased from 4 to 16 kpsi as shown in insert of Figure 3-3. A further increase of the pressure to 20 kpsi resulted in

a significant increase in PDI, likely due to the re-coalescence between newly formed oil droplets.[204]

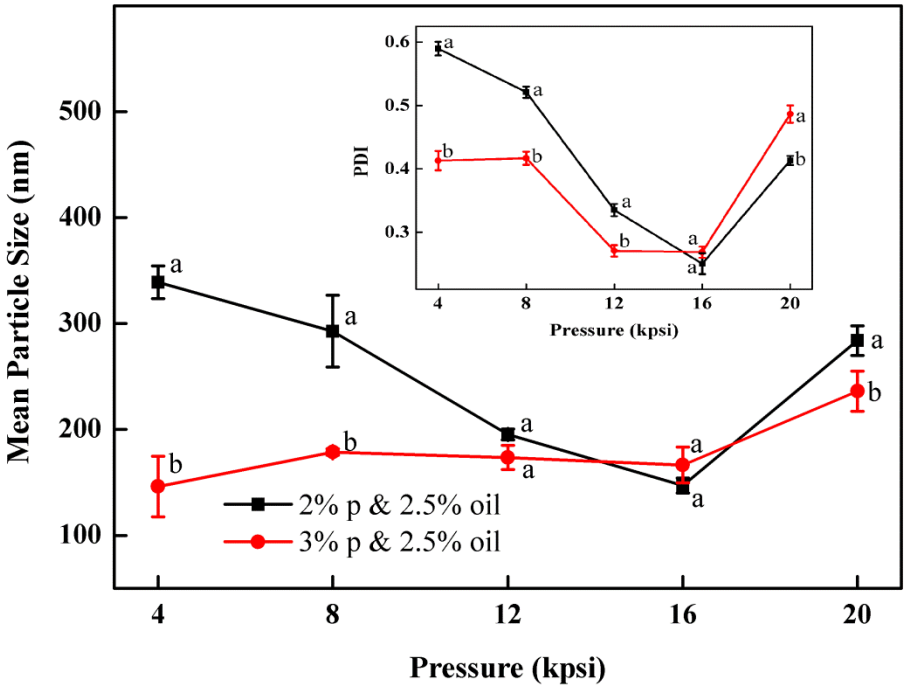

Figure 3-3 Effect of homogenizing pressure on the mean particle size of samples produced with 2 and 3 wt% barley proteins and 2.5% (v/v) oil by 6 passes. The inset shows the effect of homogenizing pressure on particle size distribution as indicated by PDI. Different letters above or below the curve indicate significant difference (p<0.05) due to protein concentration.

3.3.1.2 The influence of nanoparticle formula on the particle size

Trials were then carried out to determine how nanoparticle formation is affected by protein concentration and oil-to-protein ratio and the results were depicted in Table 3-1. The samples were prepared at 16 kpsi and 6 passes, which was determined to be optimal. Well dispersed nanoparticle suspensions were obtained at the oil-to-protein ratio of 1.25 to 2.5 for 2% protein

and 1.5 for 3% and 5% protein. Within this range, there was adequate protein around the oil droplet surface to form a solid coating during high pressure homogenization. When the oil-to-protein ratio was too high, there was insufficient protein to cover the oil-water interface, which resulted in high level of oil droplet coalescence and/or particle flocculation.[210] On the other hand, when the oil-to-protein ratio was too low, protein molecules would aggregate via interactions of excessive hydrophobic amino acid residues which would engage in protein-lipid interactions at higher oil-to-protein ratios, leading to protein precipitation.[204] The optimized formulas were then selected to study the impact of protein concentration and oil content on the particle size at 12 and 16 kpsi, respectively.

Table 3-1 Formation of stable nanoparticle suspension prepared with different formulas at 16kpsi

Protein Concentration	Oil Contents/ % (v/v)			
	1	2.5	5	7.5
2 wt%	Excessive Protein Precipitation	Formation of Particles	Formation of Particles	Particle Aggregation
3 wt%	Excessive Protein Precipitation	Formation of Particles	Formation of Particles	Particle Aggregation
5 wt%	Excessive Protein Precipitation	Excessive Protein Precipitation	Slight Protein Precipitation	Formation of Particles

As demonstrated in Figure 3-4, the mean particle diameter decreased with an increase of the initial barley protein concentration. For example, with oil concentration fixed at 2.5%, the mean

particle diameters were 195, 174 and 127 nm when prepared at 12 kpsi with 2%, 3% and 5% barley protein, respectively. This result was expected because higher protein concentrations led to thicker coatings outside oil droplets during high pressure homogenization, which reduced the surface tension and avoided the re-coalescence between disrupted oil droplets.[204] For the same reason, PDI of nanoparticle samples decreased as initial protein concentration increased. Samples prepared with 5% protein had PDI of 0.29 and 0.27 at 12 and 16 kpsi, respectively even when the oil concentration was as high as 7.5%. On the other hand, for the same protein concentration, particle size increased significantly with the rising oil ratio at both 12 and 16 kpsi, as shown in Figures 3-4 and 3-5. For example, at protein concentration of 5%, the particle size increased from 92 to 179 and 202 nm when oil content was raised from 2.5 to 5 and 7.5%, respectively. A higher ratio of the oil phase would increase the viscosity of the emulsion, and thereby more energy input was required for droplet disruption. Meanwhile, it led to higher frequency of oil droplet re-coalescence as there were not sufficient barley proteins to cover the disrupted oil droplets. The PDI of samples prepared with 3% protein at 16 kpsi increased from 0.22 to 0.44 when the oil content increased from 1% to 7.5%.

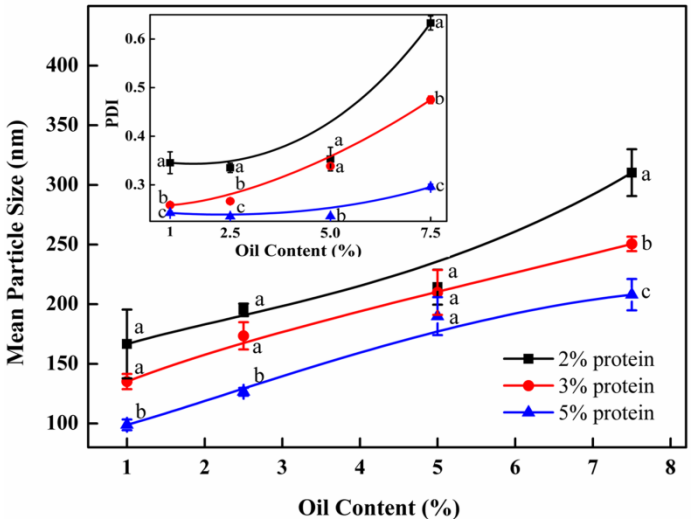

Figure 3-4 Effect of protein concentration and oil content on the mean particle size of samples produced at 12 kpsi by 6 passes. The inset shows the effect of protein concentration and oil content on particle size distribution as indicated by PDI. Different letters above or below the curve indicate significant difference (p<0.05) due to protein concentration.

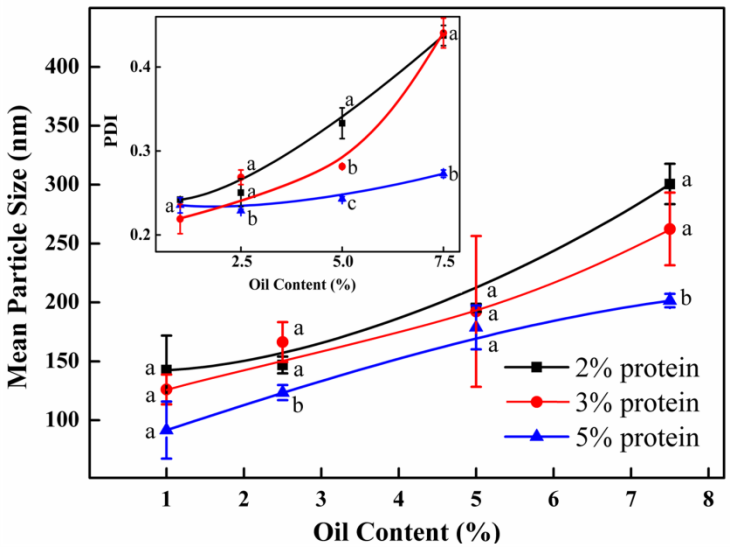

Figure 3-5 Effect of protein concentration and oil content on the mean particle size of samples produced at 16 kpsi using 6 passes. The inset shows the effect of protein concentration and oil content on particle size distribution as indicated by PDI. Different letters above or below the curve indicate significant difference (p<0.05) due to protein concentration.

Notably, nanoparticles with small sizes (90-150 nm) and narrow size distributions (PDI<0.3) can be achieved by up to 5 wt % protein concentration when the oil-to-protein ratio was maintained within a range from 1 to 1.5. Zein[211], gliadin[212], soy proteins[213] and milk proteins[198] can only form nanoparticles at protein concentrations of less than 2%. The more concentrated nanoparticles achieved in this study were a significant improvement as mass production of nanoparticles with narrow sizes in water is a challenge facing industry and academic researchers. Samples prepared with 2% protein and 2.5-5.0% oil, 3% protein and 5% oil, as well as 5% protein and 7.5% oil, prepared at 16 kpsi and 6 passes were selected for further study due to their small size and narrow size distribution.

3.3.2 Nanoparticle characterization

The surface oil content, encapsulation efficiency (EE) and loading capacity (LC) of the nanoparticle samples were demonstrated in Table 3-2. All samples demonstrated high EE (89.2-93.5%) and LC value (51.4-54.4%) except for that prepared with 2% protein and 5% oil which only showed an EE value of 83.3% and LC value of 56.1%. This is probably due to insufficient amount of protein available to form a thick coating around the lipid droplets when oil-to-protein ratio was high. The amount of surface oil is one important factor influencing the shelf life of the encapsulated oil and lipophilic bioactive compounds as it is openly exposed to the environment and has a high possibility of being oxidized or degraded. The oxidation and degradation of surface oil not only forms undesired products, but also triggers the oxidation reaction of bioactive compounds inside particles.[214] It is noticed that samples prepared with higher protein concentration exhibited significantly reduced surface oil. For example the nanoparticles prepared with 5% protein and 7.5% oil had only 1.92% of total added oil attached at the particle surface although the oil-to-protein ratio was relatively high. The surface charge is another important characteristic of nanoparticles as it plays an important role in the physiological properties and stability of nanoparticles.[215] The surface charge of nanoparticles is determined by the exposed side chains of the amino acid residues, the pH and the ionic strength of the environment. Barley protein nanoparticles exhibited a strong negative charge of around -35 mV in neutral aqueous solution as shown in Table 3-2. Negative charge is expected at neutral pH as

barley protein has an isoelectric point (pI) of around 5.[18] Nevertheless, it is interesting to notice that barley protein nanoparticles were much more negatively charged than many other protein nanoparticles (such as zein, gliadin and soy protein nanoparticles) which exhibited relatively low zeta-potential (-10 to -15 mV) at neutral pH.[211, 213, 216] It could be deduced that during high pressure homogenization, barley protein reoriented its conformation with the hydrophobic region towards the oil phase and hydrophilic region towards the aqueous phase. Therefore, the hydrophilic amino acid residues with negative charges, such as the carboxyl group from glutamic acid were exposed outside, rendering nanoparticles highly negatively charged. It has been shown that nanoparticles are more stable in suspension when their zeta-potential is above ± 30 mV due to the fact that the electrostatic repulsion between particles prevents them from aggregation.[217]

Table 3-2 Surface oil content, encapsulation efficiency, loading capacity and zeta potential for 4 selected samples prepared at 16kpsi

	Surface Oil Percentage (%)	Encapsulation Efficiency (%)	Loading Capacity (%)	Zeta Potential (mV)
2% Protein & 2.5% Oil	8.74 ± 1.59^{b}	89.19 ± 1.70^{ab}	46.55 ± 0.90^{a}	-33.83 ± 0.83^{a}
2% Protein & 5% Oil	8.79 ± 0.88^{b}	83.31 ± 1.53^{a}	56.12 ± 5.78^{a}	-37.63 ± 0.75^{b}
3% Protein & 5% Oil	4.80 ± 0.35^{ab}	92.53 ± 2.52^{b}	51.38 ± 1.40^{a}	-35.47 ± 0.95^{a}
5% Protein & 7.5% Oil	1.92 ± 1.30^{a}	93.52 ± 0.41^{b}	54.39 ± 0.24^{a}	-33.67 ± 0.51^{a}

Note: different letters next to the value indicate significant difference ($p<0.05$) due to different formulations.

The stabilities of the barley protein nanoparticles were tested for 15 days during storage at 4˚C in deionized water (Figure 3-6). All selected samples were rather stable during the storage period although a size increase trend was observed. The only exception was the sample prepared with 2% protein and 5% oil which underwent a more obvious size change from 196 to 289 nm due to its high surface oil content and insufficient protein coverage. The good storage stability of barley protein nanoparticles even at high protein concentrations without using surfactants was likely due to their small particle sizes, high surface charges and solid protein coatings.

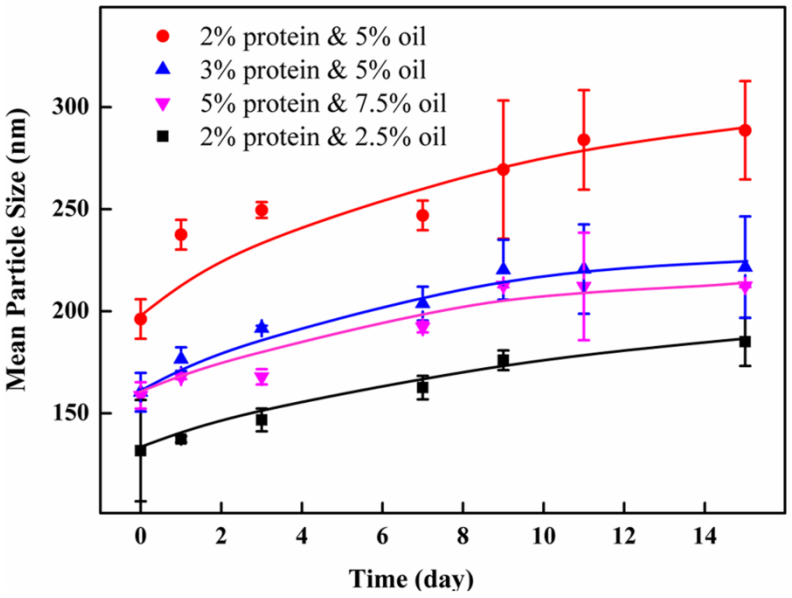

Figure 3-6 Mean particle size changes of 4 samples prepared at 16kpsi over 15 days

3.3.3 *In vitro* release and degradation in the simulated gastrointestinal tract

The release of incorporated ingredients from the protein matrix mainly involves three mechanisms, including diffusion from the matrix, enhanced diffusion through protein matrix swelling and liberation due to matrix degradation and erosion.[218] The encapsulated lipid phase in nanoparticles is more likely to be released through the degradation of the protein matrix in the gastrointestinal (GI) tract. β-Carotene was selected as a model lipophilic bioactive compound in this study, as β-carotene has the highest pro-vitamin A activity but its low water solubility and low bioavailability have severely limited its applications.[194] Nanoparticles prepared with 2% protein and 2.5% oil were selected for these tests because of their optimized characteristics.

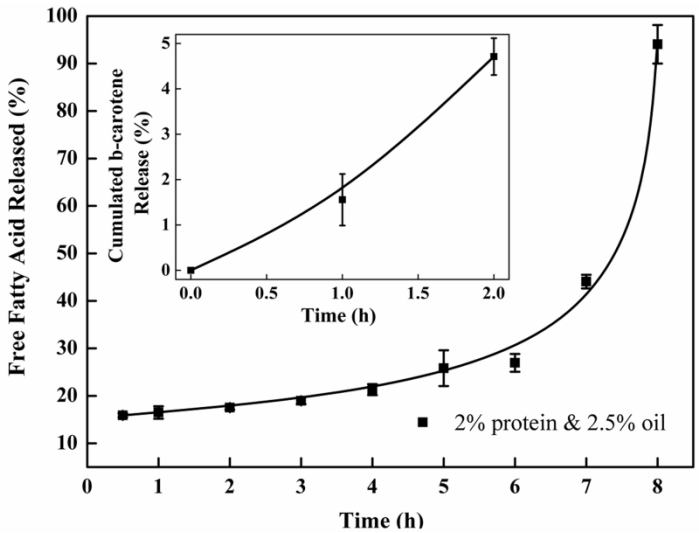

Figure 3-7 Release profile of cumulative free fatty acid from barley protein nanoparticles (2% protein and 2.5% oil in SIF for 8 h. The inserted graph showed the cumulative release percentage of β-carotene from the barley protein nanoparticles incubated in SGF for 2 h.

The inserted graph in Figure 3-7 displayed the cumulative release of β-carotene from barley protein nanoparticles incubated in SGF (pH 1.5 with pepsin) for 2 h. Less than 5% of the β-carotene was released. Actually no more than 10% of the β-carotene was released from the protein matrix even after 6 h of incubation in SGF in the presence of pepsin (data not shown). Such low release rates suggested that the barley protein nanoparticles could resist low pH and pepsin degradation, and thus provided protection for β-carotene against the harsh gastric environment. A morphology change of the nanoparticles after incubation in SGF was also observed by TEM. Interestingly, the original nanoparticles were degraded to form even smaller particles of 20-50 nm with regular spherical shapes (Figure 3-8 A&C). The decreased size was further supported by data from a dynamic light scattering evaluation, which showed an average

particle size of 43±7 nm after 1 h of incubation in SGF. This result indicates that the barley protein nanoparticle matrix was partially digested by pepsin to liberate the encapsulated oil droplets covered by a thinner but solid coating of barley protein which was indigestible by pepsin. This explained the low β-carotene release percentage in SGF. The majority of the hydrophobic amino acids on the protein chains were likely oriented towards the lipid phase, leaving the hydrophilic groups on the outside. As pepsin is most efficient in attacking peptide bonds involving hydrophobic amino acids,[219] the layer of barley protein coated on the lipid surface represented a substrate that was less vulnerable to pepsin digestion. On the other hand, barley protein has a high percentage of proline (16%)[18] which made degradation of the coating layer even slower as proteins with high proline content are generally more resistant to degradation by digestive enzymes in the GI tract.[220] β-Carotene was susceptible to the acid environment because β-carotene can be dissociated to form carotenoid carbonations.[221] Meanwhile, other common ingredients in the food matrix, such as iron, could also induce oxidation of the released β-carotene molecules, which adversely affects the bioactivity of β-carotene.[222] This issue was also reported for other lipophilic bioactive compounds, such as α-tocopherol.[223] Thus, maintaining the bioactive form of β-carotene until absorption is important. The resistance of barley protein nanoparticles to the stomach environment is a favourable property to improve the bioavailability of β-carotene.

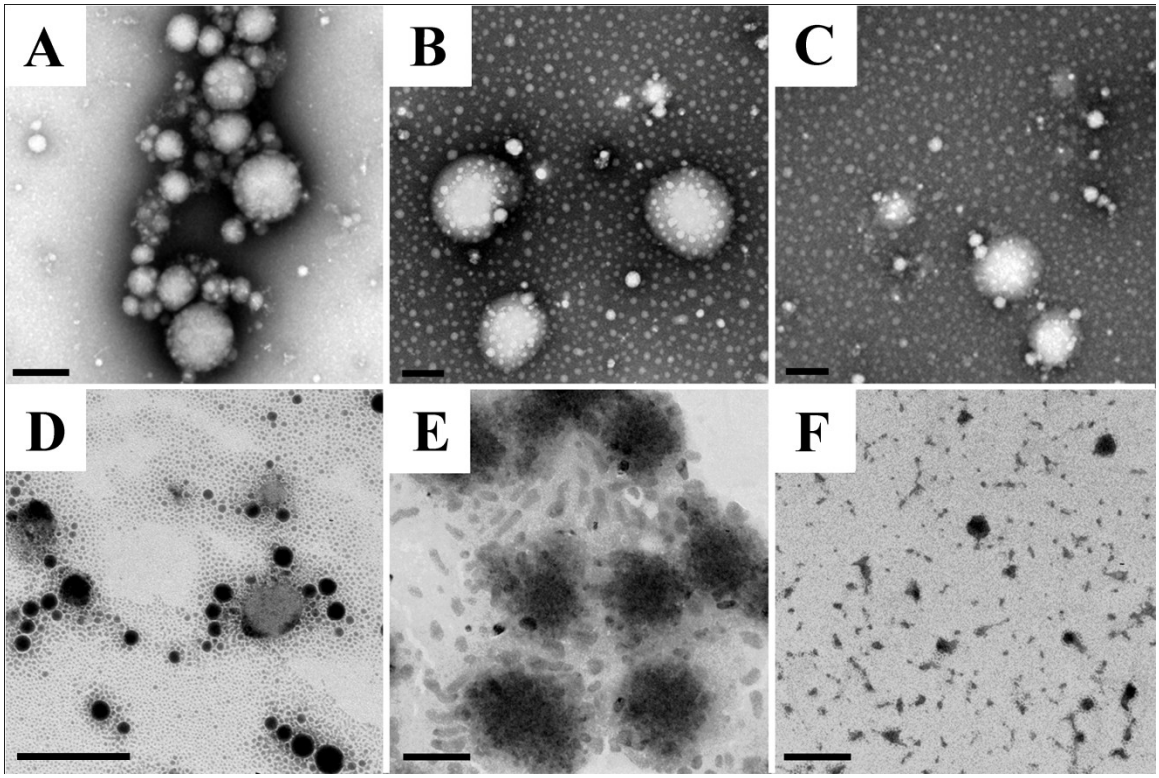

Figure 3-8 TEM images of nanoparticle morphology changes during digestion in SGF and SIF for different time: (A) original nanoparticles prepared with 2% protein & 2.5% oil, (B) in SGF with pepsin for 20min, (C) in SGF with pepsin for 1h, (D) in SIF with pancreatin for 1 h, (E) in SIF with pancreatin for 3 h and (F) in SIF with pancreatin for 7 h. Scale bars: 200 nm.

After incubation in SGF for 1 h, the nanoparticle samples were transferred into SIF for another 8 h. It was attempted to obtain the release profile of nanoparticles in SIF by hexane extraction. Nevertheless, the result was not consistent, which may be due to the incomplete extraction of β-carotene [198, 224]. Thus, the release profile of nanoparticles in SIF was measured by a method based on a pH-stat model which has been widely used in the pharmaceutical and food industries to rapidly screen lipid based formulations.[199] Since the pancreatin in SIF contained appropriate concentrations of the major lipid digestive enzymes, pancreatin lipase digestion led to the

generation of free fatty acids and 2-monoglyceride from triglyceride molecules. Therefore, it was reasonable to quantitatively measure the release of the lipids by analyzing liberated free fatty acids in SIF media. Meanwhile, this result also indirectly demonstrated the degradation behaviour of the protein coating, since the ability of lipase to come in close proximity to lipid molecules governs the rate of lipid digestion. Although measuring the liberated free fatty acids cannot directly show the release profile of the encapsulated lipophilic bioactive compounds, this *in vitro* digestion result in combination with TEM (showing the morphology changes) and a Caco-2 cell model (showing the nanoparticle uptake) can provide valuable information with respect to the nanoparticle degradation and release behaviour in the simulated GI tract. As indicated in Figure 3-7, over the first 7 h of incubation, the cumulative release increased from ~5 to 40% and then >90% of free fatty acids were detected in the release media at 8 h, indicating that ~50% of the free fatty acids was liberated in the last hour of incubation. The degradation behaviour of the above liberated smaller nanoparticles was also observed with TEM in SIF (Figure 3-8 D-F). After 1 h of incubation in SIF, the liberated nanoparticles (mainly 20-50 nm) were further digested into nano-sized lipid droplets, indicating that the barley protein solid coating was further degraded in SIF. Meanwhile, there was no evidence of oil droplets aggregating or coalescing at this stage, which was expected since they were covered by a thin layer of protein or protein hydrolysates. The mean particle size of samples incubated in SIF for another hour was 47±1 nm. Then, nano-scaled structures were observed when sample was incubated in SIF for 3 h (Figure 3-8 E). These colloidal structures could be vesicles, mixed

micelles and micelles which were able to internalize the undigested lipid molecules and β-carotene inside.[199, 225] It was reported that β-carotene is likely to be absorbed through the small intestine in the form of mixed micelles and/or vessels.[194] Therefore, barley protein nanoparticles have the potential to improve the adsorption of β-carotene in small intestine. After incubation in SIF for 7 h, the nanoparticles were further degraded into small irregular fragments. Nanoparticles with 3% protein & 5% oil and 5% protein & 7.5% oil had similar release profile as the one shown above (data not shown).

3.3.4 Cytotoxicity and cell uptake

Both the cytotoxicity and the cell uptake of barley protein based nanoparticles were evaluated on a Caco-2 intestinal cell line which was derived from a human adenocarcinoma cell line. When grown on plastic dishes or filters, the confluent monolayer formed by Caco-2 cells exhibits tight junction complexes and possesses similar morphological, functional and electrical properties to human small intestinal cells. Thus, Caco-2 cells have been widely used as an *in vitro* model to investigate the uptake and transportation of materials through the small intestinal epithelium.[226] Nanoparticles prepared with 2% protein and 2.5% oil were used in these tests.

The viability of Caco-2 cells was measured by MTT assay after incubation with nanoparticles and the digested nanoparticle samples. As shown in Figure 3-9, the cell viability was 88.4, 95.3 and 92.9% for samples incubated with 0.5, 0.25 and 0.125 mg/mL nanoparticles, respectively. High cell viability (about 90%) was also observed for nanoparticle samples digested by SGF for

1 h and subsequently by SIF for 1, 3 and 6 h. These results indicated that barley protein nanoparticles were biocompatible and had low toxicity even at high concentrations of 0.5 mg/mL.

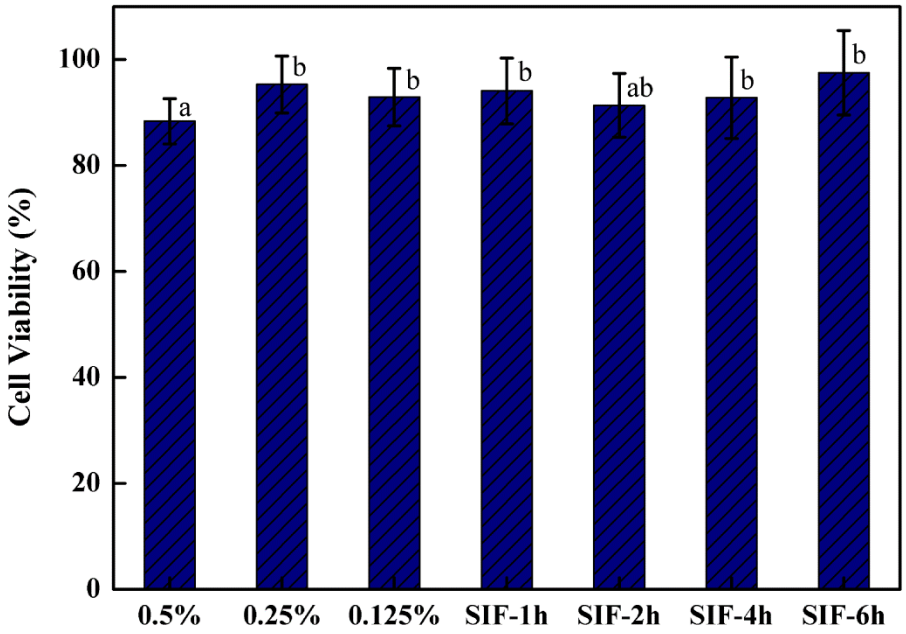

Figure 3-9 Percentage of cell viability evaluated by MTT assay on Caco-2 cells treated with increasing concentration of barley protein nanoparticles for 6 h and with pancreatin digested nanoparticles for 1 to 6 h. Different letters above the bars indicate significant difference (p<0.05) due to nanoparticle concentration and digestion condition.

Confocal microscopy was used to measure the amount of nanoparticles taken up by Caco-2 cells (Figure 3-10). Nanoparticles were prepared with 2.5% canola oil containing 0.025% Nile Red which was used as a model of lipophilic bioactive compounds and is also a fluorescent stain for oil. As mentioned above, barley protein nanoparticles and their digested products were different

in many physiochemical properties such as size, morphology and surface properties which governed their uptake in the small intestine.[227] Therefore, intact nanoparticles and 4 selected digested products were incubated with Caco-2 cells to investigate their uptake properties. As displayed in Figure 3-10 A-E, red signals were clearly observed in all five samples, indicating that the encapsulated oil phase (containing Nile Red) was able to be effectively internalized and accumulated in the Caco-2 cell cytoplasm. Although intact nanoparticles, liberated nano-sized lipid droplets and micelles had different physiochemical properties, they all have potential to facilitate the adsorption of the encapsulated lipophilic compounds *in vivo*.

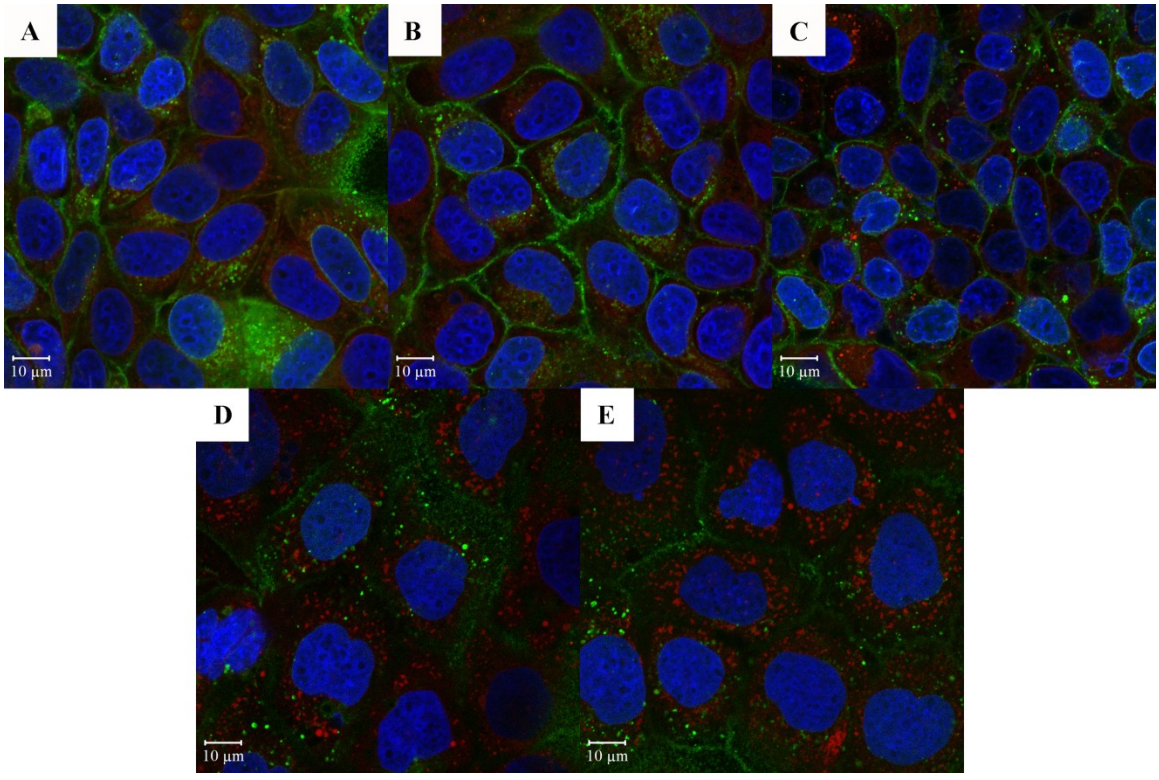

Figure 3-10 Confocal micrographs of Caco-2 cells after 6 h incubation with (A) initial nanoparticles; (B) particles after 1 h digestion in SGF with pepsin; (C) to (E) particles after

another 1, 3 and 6 h digestion in SIF with pancreatin respectively. Blue and signals represents cell nucleus and membrane, respectively.

3.4 Conclusions

Nanoparticles with small sizes (90-150 nm) and narrow size distributions were prepared from barley protein without the use of any organic solvents or cross-linking reagents. These nanoparticles demonstrated good storage stability in the absence of surfactants and contained a high payload (51.4-54.4%) of lipophilic nutraceutical compounds with limited surface oil. Interestingly, release experiments showed that even smaller particles (20-50 nm) were formed as a result of pepsin degradation of barley protein nanoparticle matrices. These smaller nanoparticles provided sufficient protection of the model nutrient in the SGF. Moreover, sequential lipophilic micro-domains were formed within the simulated intestinal environment, which helped stabilize water insoluble nutraceuticals in solution and may benefit their adsorption. Complete release of the model nutrients occurred after 7 h of degradation by pancreatin. Both original barley nanoparticles and the liberated smaller ones after pepsin digestion exhibited low cytotoxicity through *in vitro* study using Caco-2 cell models and they could be accumulated in the cytoplasm after being uptaken into Caco-2 cells. Meanwhile, nanoparticles have a unique colloidal nature whereby their charge as well as their Brownian motion can cause the dispersion to be stable, thus they can be administered by both parenteral and non-parenteral routes, enabling wider applications. Thus, these barley protein nanoparticles have strong potential to be used as delivery systems of bioactive compounds for food, pharmaceutical and cosmetic applications.

Moreover, this study provides meaningful justification for further *in vivo* studies to evaluate the safety and efficacy of barley protein nanoparticles as a delivery system.

Chapter 4

Creation of 3D Hierarchical Porous Nitrogen-Doped Carbon Fibers for Supercapacitors from Plant Protein and Lignin Electrospun Fibers

4.1 Introduction

Supercapacitors have attracted extensive attention in recent years due to their high power densities, rapid charging time and long cyclic stability.[122] They show promise to meet the increasing power demand for energy storage systems in various applications, such as portable electronics, mobile electric systems, hybrid electric vehicles and industrial power management.[100] Supercapacitors can be classified into two categories by different energy storage mechanisms: electrical double-layer capacitors (EDLCs) and pseudocapacitors.[113] EDLCs are based on the adsorption of electrolyte ions on the surface area of conductive materials, while pseudocapacitors store energy faradaically by electrosorption, reduction-oxidation reaction and intercalation processes.[102] EDLCs are favourable in commercial utilization currently due to their superior cycle stability. Though the power density of supercapacitor is much higher than that of battery, the capacitance and energy density of supercapacitor are needed to be improved.

Carbon materials are widely used to produce EDLCs because of their good electrical conductivity and relatively low cost. The capacitance of EDLC is related to the specific area of the electrodes. Therefore, to make high performance EDLCs from carbon materials they must have a large specific surface area and a highly porous structure, fitting the size of electrolyte ion.

Extensive investigations are being conducted to develop nano-structured porous carbon materials, such as active carbon, carbon particles, carbon areogel, graphene, carbon nanotube, carbon fibers, carbide-derived carbons and template carbon. More recently, carbon materials with an hierarchical porous structure, namely, macropores in combination with meso and micro pores,[117] have been shown to have advantages as they not only provide large surface area to store energy, but also possess a shortened ion transport time.[228] Activated carbon fibers have attracted interest due to their ability to build up hierarchical porous structures with a large length/diameter ratio, large surface area and large pore volume.[141] Activated carbon fibers show excellent electrical conductivity along the fiber axis, but their contact resistance remains to be a problem due to the large distance between fibers.[100] Interconnected fiber networks that provide shorter and more continuous electron transport pathways can favourably reduce the contact resistance of an activated carbon fiber electrode.[129] Currently, template casting, solvo-thermal synthesis and chemical vapour deposition methods are applied to prepare carbon fiber precursors. However, these methods have limitations such as material restrictions, high cost and process complexity.[96] Electrospinning is a relatively new, simple and convenient method to directly fabricate fiber networks where the electrospun fiber composition, diameter and alignment can be modulated to achieve carbon materials of desirable structure and performance.[229]

Incorporating heteroatoms such as nitrogen and oxygen into the carbon framework is an effective strategy to improve the EDLCs performance. For example, nitrogen doping has been shown to induce pseudocapacitance to carbon materials by additional faradaic redox reaction and/or

chemisorption.[126, 230, 231] Nitrogen functional groups are normally added into the carbon nanostructures by *in situ* doping during carbon synthesis using nitrogen-rich synthetic polymers such as polyaniline and polypyrrole, or nitrogen-containing ionic liquid. This can also be achieved through post-treatment of carbon materials with nitrogen containing reagents such as ammoniate.[119, 232] Carbonizing nitrogen-rich biomass has provided an environmentally sensitive and efficient alternative to prepare nitrogen-doped carbon materials since nitrogen-rich biomass can be converted to N-doped carbon through one-step pyrolysis. Proteins, rich in N and O, are one of the most abundant biomaterials on earth. Previous reports showed that the carbon samples derived from biomass rich in proteins, such as hair[122], silk cocoon[141], gelatine[142] and chicken eggshell membranes[138], possess high capacitance of more than 200 F/g. However, to the best of our knowledge, protein-based carbon fibers with a hierarchical porous structure have not been reported as supercapacitor material.

Zein and hordein are the major alcohol soluble storage proteins (prolamins) in corn and barley, respectively. Zein is the by-product of corn starch processing and the major coproduct of corn fermentation to produce ethanol.[233] Hordein is largely available as the by-product of barley starch and β-glucan extraction industries.[2] Development of a value-added product of zein and hordein would commercially benefit cereal growers and processors as well as reduce the wastes. Nano-fiber fabrics based on the mixture of zein and hordein have been developed already by some previous work with electrospinning.[28, 30, 93] Such fabrics contain a large amount of nitrogen in the polypeptide chains and show good tensile strength, controllable diameter and continuous

fiber network.[28, 30, 93] In this study, it was proposed that these were important attributes to create interconnected 3D hierarchical porous nitrogen-doped carbon fibers with superior capacitive performance.

This study aims to explore this new area of research to create energy storage materials with electrospun zein/hordein protein nanofiber fabrics. The challenge is to maintain a fibrous protein mat structure due to the thermoplastic nature of proteins. To overcome this challenge, lignin is added to the plant protein spin dope since this common and abundant natural material has a large content of aromatic components to maintain the fibrous structure. Under proper heating conditions, lignin can be converted to a thermosetting material,[234, 235] that would aid with the development of a hierarchical porous structure.[129]

The objective of this study is to develop plant proteins-lignin based electrospun nanofibers fabric and to convert them into N-doped carbon fibers with 3D interconnected hierarchical porous structure as electrode materials for supercapacitor. In this study, the effects of protein/lignin ratio and the carbonization temperature on carbon fiber morphology and electrochemical performance were systematically evaluated and discussed. The surface N functionalities were studied by X-ray photoelectron spectroscopy (XPS), and the morphology and the porous structure were observed by scanning electron microscopy (SEM).

4.2 Materials and methods

4.2.1 Materials

Barley grains (Falcon) were kindly provided by Dr. James Helm, Alberta Agriculture and Rural Development, Lacombe, AB, Canada. Hordeins were extracted from barley grains using an ethanol solution according to a procedure reported in previous work.[18] Zein (F4000, 92% protein content) was kindly provided by Freeman Industries LLC (New York, NY, USA) and used without further purification. Alkali lignin, polyvinylidene fluoride (PVDF), molecular weight ~275,000 by gel permeation chromatography), N-methyl-2-pyrrolidone (NMP), potassium hydroxide and acetic acid were purchased from Sigma-Aldrich Canada Ltd (Oakville, ON, Canada). Dimethylformamide (DMF) and Carbon black Super P was obtained from Fisher Scientific (ON, Canada) and Alfa Aesar (Ward Hill, MA, US), respectively. All chemicals were used as received unless otherwise specified. Ultrapure water treated with a Milli-Q Advantage A10 system (EMD Millipore Corporation, MA, US) was used to prepare electrolyte solution.

4.2.2 Preparation of plant protein-lignin electrospun fibers

Lignin and plant protein (hordein:zein = 50:50, w/w) powders were dissolved in a mixed solution of acetic acid and DMF (90 and 10%, v/v) and stirred for 12 h. The total content of polymers was 36% (w/v). The lignin and protein blending ratios were 20/80, 50/50 and 80/20 (w/w). Correspondingly, their electrospun fiber samples were coded as L2P8, L5P5 and L8P2, respectively. The electrospinning experiments were carried out on a customized digital

electrospinning apparatus EC-DIG (IME Technologies, Eindhoven, Netherlands) at 25°C. Solutions were forced through a blunt needle with a diameter of 0.8 mm at the flow rate of 1 mL/h. The spinning voltage was fixed at 20 kV and the needle to collector distance was 20 cm. The electrospun fiber fabrics were collected on a rotary collector with a rotating speed of 1 rpm.

4.2.3 Carbonization and activation

The carbon fibers were synthesized by carbonizing the protein and lignin electrospun fiber fabrics in a tubular furnace (GSL-1100X-NT-UL, MTI Corporation, CA, US), followed by a carbon dioxide activation step. In a typical experiment, the carbonization step was operated with the following heating procedure under continuous purge of argon: (1) temperature raised from 25˚C to 200˚C at a rate of 5˚C/min; (2) temperature held at 200˚C for 2 h to stabilize the protein-lignin electrospun fibers; (3) temperature increased from 200˚C to 300˚C at a rate of 1˚C/min to slow down the thermo decomposition of protein to maintain the fibrous structure; (4) temperature continued to increase from 300˚C to a final carbonization temperature (750 or 900˚C) at 5˚C/min; (5) carbonization temperature held for 2 h; (6) sample cooled down naturally under argon flow. A number following the sample code was added for each carbon fiber sample to indicate its carbonization temperature. For example, L2P8-750 represents carbon sample prepared with 20% lignin and 80% protein, and carbonized at 750˚C. Then, the selected carbon fibers were activated at 800˚C in a CO_2 atmosphere for 3 h to generate porous structure on the

carbon fiber surface. The temperature increased from 25˚C to 200˚C at a rate of 5˚C/min and the activated carbon fibers cooled down naturally under CO_2 flow.

4.2.4 Fiber size and morphology observation

The size and morphology of both the original and carbonized fibers were observed by a Hitachi X-650 scanning electron microscope (SEM, Hitachi, Japan) at 20 kV. The original fiber samples were sputtered with gold for 2 min before observation. The surface pores of the activated carbon fiber were observed by SEM equipped with a cold field emission gun at 15 kV (S-4800 FE-SEM, Hitachi, Japan). High resolution transmission electron microscope (HRTEM, JEOL 2100, JEOL Inc., US) was further employed to study the microstructure of carbon fiber samples. For this, samples were ground into powders and then deposited onto the 300 mesh Cu/Pd grids.

4.2.5 Fiber textural characterization and chemical analysis

AutosorbiQ (Quantachrome Instruments, Boynton Beach, FL, US) was employed to measure the nitrogen adsorption-desorption isotherm, specific surface area and the porous texture at 77 K. The specific surface area and pore size distribution were calculated based on the Brunauer-Emmett-Teller (BET) theory and nonlocal density functional theory, respectively. The micropore and external pore surface area was calculated by *t*-plot method. These analyses were done by the AutosorbiQ's associated software (ASiQWin). X-ray powder diffraction (XRD) patterns were obtained to show the crystallinity of carbon by using a Bruker AXS D8 Discover diffractometer (Bruker Coperation, East Milton, ON, CANADA) with the Cu Kα radiation (λ =

1.541841 Å) at 40 kV and 44 mA (2θ was from 10 to 80°). Raman spectra were obtained to examine carbon sample structure by a Nicolet Omega XR Raman microscope (Thermo Fisher Scientific, Waltham, MA, US). The excitation near infrared laser wavelength was set at 532 nm and data points were recorded at 0.5 cm^{-1} intervals. The nitrogen and carbon contents of the original fibers were measured by Leco nitrogen analyzer (FP-628, Leco, St. Joseph, MI, US). X-ray photoelectron spectroscopy (XPS) was applied to analyze the chemical composition of carbon surface using an Axis Ultra spectrometer (Kratos Analytical, Manchester, UK). X-radiation Al Kα (hυ = 1486.6 eV) was used. The C 1s and N 1s core levels were fitted using the CasaXPS software to reveal C and N configuration. The thermogravimetric analysis (TGA) of the original protein fibers was conducted by a thermogravimetric analyzer (TA Instruments, Q500, New Castle, DE, US) under argon at a heating rate of $2^{o}C$/min. The Fourier transform infrared spectra (FTIR) of the original protein fibers and those after heating treatment to $200^{o}C$ for 2 h (under Argon) were obtained by a Nicolet 6700 spectrophotometer (Thermo Fisher Scientific, Waltham, MA, US) to analyze protein conformations. An attenuated total reflectance (ATR) accessory with a Ge crystal was used for measurement. Spectra were collected in the range of 4000-800 cm^{-1} as an average of 256 scans at 4 cm^{-1} resolution.

4.2.6 Electrochemical performances

The activated carbon samples were ground and mixed with 10 wt % carbon black and 10% PVDF binder (10 wt% in NMP) to form a paste. The paste with 8mg of carbon sample was cast

onto a piece of nickel foam in an area of 1.0 cm^2 and dried under vacuum at 120^oC for 12 h, and then pressed under 2000 psi by a benchtop laboratory press (model 3851, Carver Inc., Wabash, IN, US) to fabricate an electrode. To assemble a three-electrode cell, the above prepared nickel foam, a Pt wire and an Hg/HgO were used as working, counter and reference electrodes, respectively. All the electrochemical properties were analyzed by a Solartron 1287 electrochemical interface (Solartron Analytical, Berwyn, PA, US). Cyclic voltammetry studies were performed in the potential window of -1.0 to 0 V vs. reference electrode at various scan rate from 5 to 100 mV/s. Galvanostatic charge-discharge curves were measured with current density from 0.5 to 10 A/g. The specific capacitance of carbon materials was calculated by the following equation:

$$C = \frac{I\Delta t}{m\Delta V}$$

Where I (A) is the discharge current, Δt stands for the discharging time, m (g) is the weight of carbon sample loaded on the working electrode and ΔV represents the potential window. Electrochemical impedance spectroscopy (EIS) was performed in a frequency range from 10^{-2} to 10^5 Hz with 5 mV amplitude.

4.2.7 Statistical analysis

All experiments were performed at least in three independent batches. For SEM and TEM results, one typical image was presented respectively. For nitrogen adsorption-desorption isotherm, TGA,

FTIR, Raman spectroscopy, XRD, XPS and electrochemical analysis, one typical curve was presented respectively.

4.3 Results and discussion

4.3.1 Morphology of carbon fibers

It was challenging to maintain the interconnected protein fiber networks during the carbonization process up to 750°C. Proteins are thermoplastic materials and often melt and lose their original structure at carbonization temperatures. The amorphous regions of protein molecule become mobile above the glass transition temperatures. Crystalline regions then melt above the melting temperature before decomposition at even higher temperatures.[236] To overcome this problem, lignin was added to sustain the fiber structure because it can transform from a thermoplastic to a thermosetting character during a continuous heating process.[235] Continuous fibers with smooth surfaces and uniform diameters were successfully prepared from a protein-lignin mixture formula as shown in Figure A1-1 in Appendix A1. The alkali lignin solution alone showed poor electrospinning properties since alkali lignin molecules had insufficient chain structure, intermolecular interactions and/or entanglements.[131] Thus, the formation of continuous electrospun fibers was attributed to the good electrospinnability of prolamin proteins.[28] Previous experiments showed that hordein/zein mixture at the ratio of 1:1 exhibited stable assembled network structure and improved the tensile strength.[28] Carbon fiber samples with different protein-lignin ratios showed significantly different morphologies after heat treatments at 750 and

900˚C (Figure 4-1). A balanced protein-lignin ratio strongly influenced the compatibility of these two biopolymers to determine the structures of the carbon products. Samples from 100% protein melted during heating and no fiber structure was formed. Samples prepared with 20% lignin and 80% protein (L2P8) created short fibrous-like structures, but the fiber network did not maintained. L5P5 samples showed continuous and smooth fiber structure after carbonization. This was likely due to compatibility between protein and lignin, allowing both of them to be homogenously distributed within the fiber network[237] so that lignin could maintain the structure of the nanofiber mats. When the protein-to-lignin ratio decreased to 20:80 (L8P2), the fiber network broke down during carbonization due to melting of the protein backbone. A large lignin concentration can lead to the immiscibility of protein with lignin,[237] thus in our case, the protein phase was likely to be separated from, and embedded in, the lignin phase. The melting and expansion of embedded protein aggregates in the lignin matrix during carbonization contributed to the disorder structure of L8P2-900. Notably, L5P5-900 showed a continuous and interconnected carbon fiber network structure. This morphology can facilitate electron transportation of the electrode; thus L5P5-900 was chosen for further experiments.

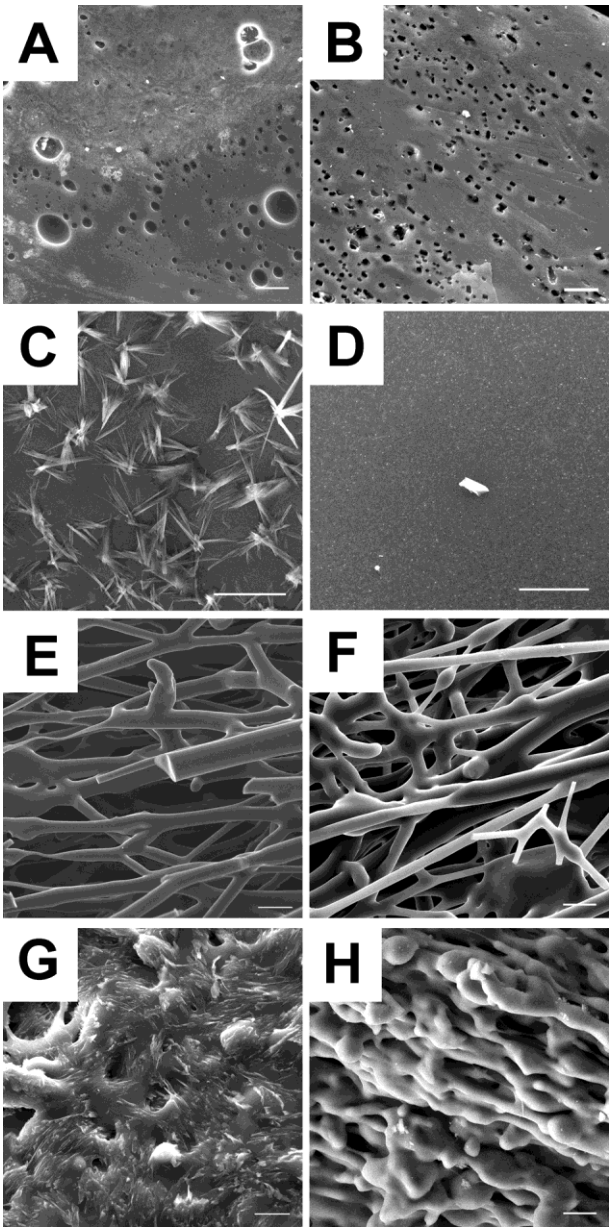

Figure 4-1 SEM images of carbon samples derived from plant protein and plant protein-lignin electrospun fibers at 750 and 900°C: (A) Pro-750;(B) Pro-900; (C) L2P8-750; (D) L2P8-900;(E) L5P5-750; (F) L5P5-900; (G) L8P2-750 and (H) L8P2-900. Scale bar: 5 μm.

4.3.2 Morphology and porous texture of L5P5-900-ACT

Methods to increase the specific surface area of carbon materials include chemical activation (using sodium hydroxide, potassium hydroxide, zinc chloride and phosphoric acid, *etc.*) and physical activation (thermal treatments under steam, air, carbon dioxide, *etc.*).[100] Heating under CO_2 gas flow is an efficient treatment to improve the pore volume and surface area as well as to control the pore-size distribution and surface chemistry of carbon materials by partial gasification of carbon surface.[238, 239] As compared to chemical activation methods, no post-treatment is required after CO_2 activation, which makes it an environmentally-friendly activation method. To further improve the structure and properties of plant protein-lignin based carbon fibers, they were pyrolyzed at 800˚C for 3 h under CO_2 atmosphere. The activated sample is suffixed with ACT in the sample code. Figure 4-2 demonstrated the hierarchical porous network formed after carbonization and activation of the L5P5-900-ACT sample. As shown in Figure 4-2 A, the carbon material maintained a continuous and interconnected fiber network after CO_2 activation. The 1D carbon microfibers with a diameter of around 5 μm interlaced together to form a unique 3D structure. The interconnected large macropores formed by fiber interlacement could facilitate the ion transportation by serving as ion-buffering reservoirs and providing low resistance for ion transportation from bulk electrolyte solution into carbon inner porous structures.[117, 240] This could subsequently contribute to the high rate capability and high power density of carbon materials.[117] Under higher magnification (Figure 4-2 B), the carbon fiber

surface was porous and composed of a large number of mesopores (around 10 nm), likely formed during the CO_2 activation step.[241] These numerous open pores not only can greatly increase the surface area, but also can improve the electrolyte ion accessibility by providing larger transport pores for diffusion from surface to inner porous structures.[100] It was interesting that the carbon fiber was comprised of multiple layers of graphene-like nanosheets, as demonstrated in the high resolution TEM (HR-TEM) images (Figures 4-2 C & D). Figure 4-2 D showed the graphene-like nanosheets stacked and folded together with the layer-to-layer distance (*d*-spacing) between sheets being 0.37 nm, similar to the spacing of the (002) distance of the graphitic carbon lattice (0.34 nm).[242] Due to the intrinsic properties of graphene, these nanosheets could improve the electrode performance by speeding up the transport of electrons and by increasing the in-plane conductivity.[243] Traditionally, the production of graphene materials has been challenging, including the high production cost and the demand for high energy input and the corrosive reagents, which limited its application as a commercial material for supercapacitors.[137, 244] This study provided a convenient and environmentally sustainable method to prepare carbon materials. It was demonstrated that porous graphene-like nanosheet structures can be created at a lower temperature (<1000°C) without the use of a catalyst.

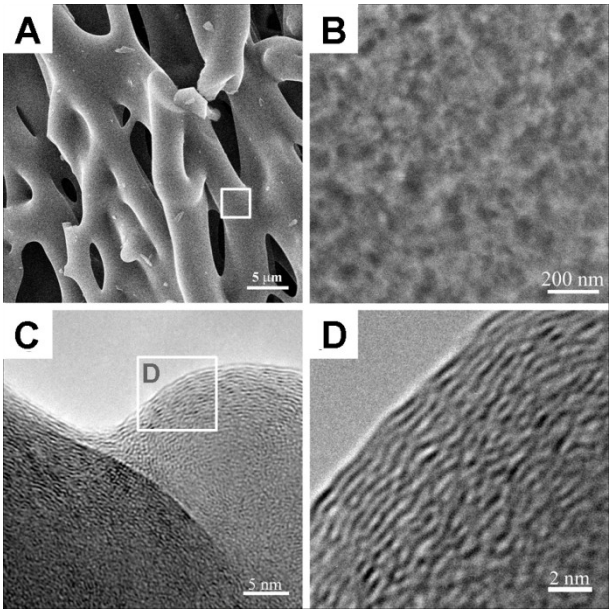

Figure 4-2 FE-SEM (A and B) and HR-TEM (C and D) images of L5P5-900-ACT sample.

The carbon precursor and the carbonization conditions both determine the structure of the final carbon material.[100] The addition of lignin can transform the product from amorphous carbon to nanocrystalline graphite, since it permits nucleation, growth and clustering of aromatic rings during pyrolysis from 600 to 1000°C.[234] However, it has not been reported so far that alkali lignin can form well-aligned graphene-like nanosheets after heating. On other hand, proteins may have the potential to form partially aligned graphitic layers.[142, 245] As shown by thermogravimetric analysis (TGA) (Figure A1-2 A), the decomposition of the original protein electrospun fibers began at around 200°C, above the glass transition temperatures of hordein and zein. At this temperature, the Fourier transform infrared (FTIR) spectra (Figure A1-2 B) showed that the protein denatured and its secondary structure dramatically changed. The amide I band (1700-1600 cm^{-1}) in the FTIR spectra is the prominent vibrational band of the protein backbone

and is correlated to protein secondary structures.[69] Protein electrospun fibers possessed one major peak at 1652 cm^{-1} which was assigned to α-helix. After heating to 200°C for 2 h, α-helix decreased while β-sheet structure increased as indicated by rising peaks at 1692, 1683 and 1623 cm^{-1}.[246, 247] The β-sheets are considered as crystal-dominant lamellar structures since they consist of polypeptide backbones connected and organized into pleated sheets by inter/intramolecular hydrogen bonds. β-sheets can transform into aligned hexagonal poly-aromatic structure with pseudographitic crystalline lattice through cyclization or aromatization by intermolecular dehydration or condensation between adjacent polypeptide chains.[140, 245, 248] Thus, it is possible that plant proteins form graphene-like nanosheets based on their β-sheet secondary structure during carbonization. However, the synergistic effects of protein and lignin are needed to be investigated further to better understand the formation mechanism of these graphene-like nanosheets.

Figure 4-3 showed the nitrogen adsorption-desorption isotherm of the L5P5-900-ACT sample; the inset depicted the pore size distribution. The total specific surface area of L5P5-900-ACT was calculated to be 771.5 m^2/g, which was comparable to other carbon fibers reported in the literature.[118, 123, 129, 141] Micropores (pores less than 2 nm) and external pores contributed 663 and 108 m^2/g to the total BET surface area, respectively. The total pore volume was 0.38 cm^3/g according to the adsorption amount at a relative pressure P/P_0 of 0.98 and the average pore diameter was 19.96 Å. The adsorption behaviour of nitrogen on L5P5-900-ACT surface showed an initial large uptake in the low pressure region ($P/P_0<0.1$), followed by a gradual increase in

the mid P/P_0 region and then a slight increase in the high pressure region (P/P_0>0.9). The carbon sample had high nitrogen adsorption at very low relative pressure (P/P_0<0.1), which was a typical indicator of the existence of micropores.[122] The isotherm continuously increased till high P/P_0 value and did not saturate even at P/P_0 of about 1, which meant that this carbon material consisted of abundant mesopores and/or macropores.[141] The hysteresis loop of nitrogen adsorption-desorption isotherm is associated with the capillary condensation of nitrogen in the pores, thus the shape of the hysteresis loop is usually used to exhibit the specific pore structures.[136, 249] Since the adsorption and desorption branches were approximately parallel to each other over an appreciable range of P/P_0, the hysteresis loop was classified as type *H4*, which was known to be related to the narrow slit-like pores.[249] The Type I isotherm with Type *H4* loop was an indicator of the existence of microporosity.[249] The hysteresis loop was observed from P/P_0 of about 0.1 to 0.95, which proven the coexistence of micropore, mesopore and macropore structures in the carbon fiber mats.[123] The pore size distribution curve showed that the L5P5-900-ACT sample had large volume of micropores with major size peaks at 1.1 and 1.5 nm, respectively, and mesopores with the diameter of 3.8 and 7.8 nm, respectively. The results from nitrogen sorption isotherm were in agreement with the observation by SEM, both confirming that L5P5-900-ACT had well-developed hierarchical pore structures at all micro, meso and macro scales.

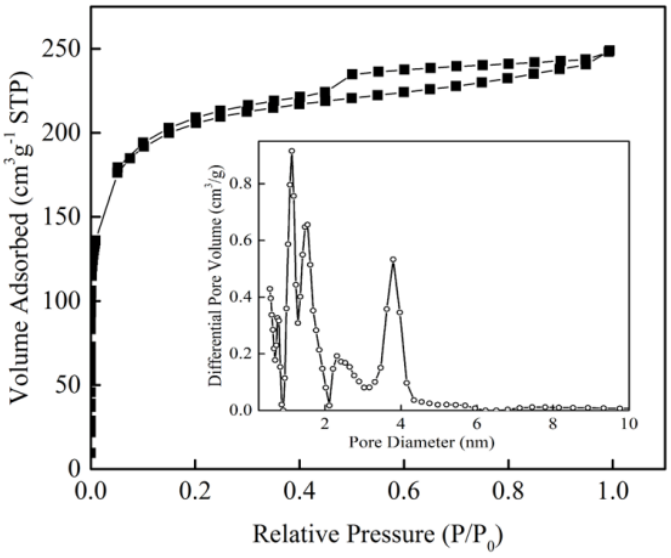

Figure 4-3 Nitrogen adsorption and desorption isotherm and pore size distribution (inset) of L5P5-900-ACT.

4.3.3 Chemical characterization of L5P5-900-ACT.

X-ray diffraction (XRD) in wide angle region was used to evaluate the structure arrangement of the L5P5-900-ACT carbon sample (Figure 4-4 A). The wide and broad peak at 23.85° (002 lattice plane) indicated the existence of layer-by-layer graphitic stacking,[250] further confirming the graphene-like nanosheet structure observed by HR-TEM. The d_{002} (interlayer spacing of 002 plane) can be calculated by the following equation $d_{002} = \lambda/(2\sin\theta_{002})$, where λ is the wavelength of X-ray used. Thus, d_{002} of L5P5-900-ACT was 0.37 nm, which was greater but rather close to the pristine graphite of 0.34 nm.[242] The increase of d-spacing was possibly caused by the presence of oxygen and nitrogen functional groups.[250] The insertion of O and/or N caused changes in the reacting carbon atoms from sp^2 to sp^3. The out of planar C-N or C-O covalent

bonds resulted in the atomic scale roughness, thus, increased the distance between graphene layers.[251, 252] Furthermore, the peak at 44° corresponded to the graphitic (100) crystal plane.[130] L5P5-750 and L5P5-900 also had peaks at about 24° and 44° as shown in Figure A1-3.

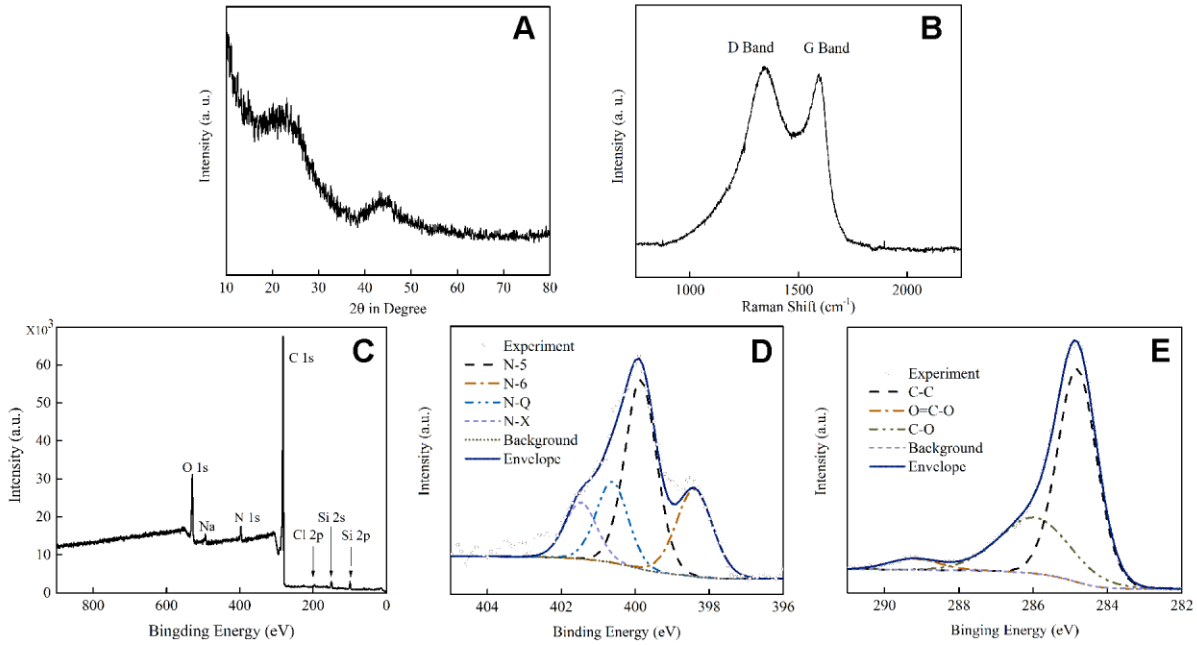

Figure 4-4 XRD pattern (A), Raman spectrum (B) and XPS spectra (C, D and E) of L5P5-900-ACT sample. D and E are the deconvoluted N 1s and C 1s peaks respectively.

Raman spectroscopy was employed to reveal the graphitic structure of L5P5-900-ACT. As shown in Figure 4-4 B, two major bands appeared in the 500-2500 cm^{-1} region, including the D band at 1344 cm^{-1} and G band at 1595 cm^{-1}. The intensity of D band is related to the vibration of C atoms with dangling bonds in planar terminations of defective and/or disordered graphite. The G band, on the other hand, is an indicator of the 2D graphite, corresponding to the vibration of

sp^2 C in a 2D hexagonal lattice.[253] Thus, the ratio of D/G band intensities illustrates the crystalline degree of carbon materials. I_D/I_G of L5P5-900-ACT was 1.04, indicating the existence of graphite carbon in L5P5-900-ACT, albeit with disorder. The I_D/I_G value of L5P5-900-ACT was greater than the pristine natural graphite which can be attributed to the introduction of oxygen and nitrogen functional groups into carbon network.[129, 254]

Cereal proteins hordein and zein contain about 16 wt% of nitrogen. Thus, the plant protein-lignin electrospun fiber is a nitrogen-rich carbon fiber precursor. In the original L5P5 fiber, the nitrogen and carbon contents were 7.0 and 56.7 wt%, respectively, as analyzed by combustion. Carbon materials doped with heteroatoms, such as nitrogen, are expected to have an enhanced surface wettability, electronic conductivity and capacitance.[230] X-ray photoelectron spectroscopy (XPS) analysis was conducted to evaluate the chemical composition of the developed carbon fibers. As shown in Figure 4-4 C and Figure A1-4, nitrogen and oxygen still maintained in the carbon networks of sample L5P5-750, L5P5-900 and L5P5-ACT after carbonization. Specifically, carbon 1s, oxygen 1s and nitrogen 1s were the three major peaks in the XPS spectrum of L5P5-900-ACT sample (Figure 4-4 C), which consisted of 4 wt% nitrogen, 13 wt% oxygen and 83 wt% carbon, respectively. Meanwhile, trace amount of impurities, such as sodium (~497 eV), chloride (~199 eV) and silicon (~99 eV) were also presented, which came from plant protein extraction. The nitrogen functional groups were further investigated after deconvolution of the N 1s spectrum. As demonstrated in Figure 4-4 D, four overlapped peaks centered at 398.4, 399.9, 400.6 and 401.5 eV were observed and assigned to N-6 (pyridinic N), N-5(pyrrolic N and/or

pyridonic N), N-Q (quaternary N) and N-X (oxidized N), respectively.[255, 256] N-5 contributed 44% of all nitrogen functional groups. N-6, N-5 and N-X were considered the nitrogen groups located at the edge of graphene layers,[257] which represented 81% of nitrogen functional groups. N-Q represents nitrogen bonded to 3 carbon atoms and was more likely to be found in the central position of graphene sheets.[121] Plentiful edge N groups were reported to be more active in contributing to the electrochemical performance. Pyridinic (N-6) and pyrrolic N (N-5) were assumed to be the main configurations introducing pseudocapacitance to the carbon materials while N-Q was beneficial to their conductivities.[119] Moreover, the C 1s spectrum consisted of 3 carbon configurations: sp^2 C=C/sp^3 C-C (284.8 eV, 64.9 at%, atomic percentage), C-O/C=N (286 eV, 30.8 at%) and O=C-O (289.2 eV, 4.3 at%).[258] The C-O type oxygen groups were shown to have positive contribution to the carbon capacitance due to their high stabilities.[120]

4.3.4 Electrochemical performance of L5P5-900-ACT.

The unique structure and chemical feature of carbon materials derived from protein-lignin electrospun fiber fabrics triggered our interest to further investigate its electrochemical performance. Thus, the cyclic voltammetry (CV), galvanostatic charge-discharge profile and electrochemical impedance spectroscopy (EIS) were used to test the feasibility of L5P5-900-ACT to performing as a supercapacitor electrode material using 6 M KOH as the electrolyte. Figure 4-5 A exhibited the CV curves of L5P5-750, L5P5-900 and L5P5-900-ACT, at a scan rate of 50 mV/s. Significant differences between these three samples were observed.

The CV curves of carbon materials without activation had a triangle shape, with greater specific current observed for L5P5-900 than L5P5-750. The triangle shape indicated that pronounced ion sieving effect occurred in these two samples.[259] In such a case, the micro range pores were too small and excluded out the electrolyte ions during scanning. After activation, the CV curve was turned into rectangular shape and had significantly increased specific current, demonstrating good capacitive behaviour. This showed that CO_2 activation opened up pores that were closed, clogged or obstructed and created meso and macropores at the surface of the carbon fibers. As shown in Figure 4-3, the major micropore diameters of L5P5-900-ACT were 1.1 and 1.5 nm, which were larger than that generally required for the accommodation of aqueous electrolytes (0.4 – 0.8 nm).[259, 260] Moreover, the mesopores and macropores at the fiber surface facilitated the transport of electrolyte and increased the accessibility of electrolyte to pores in the fiber. The small humps in the CV curve of L5P5-900-ACT were attributed to the pseudocapacitance induced by the heteroatom functional groups such as nitrogen and oxygen. Figure 4-5 B showed that the current density continuously increased as a function of scan rate for L5P5-900-ACT. The CV curve still maintained a quasi-rectangular shape even at a scan rate as high as 100 mV/s, exhibiting excellent ion transport behaviour and rapid charge propagation capability. This favourable characteristic was likely to be related to its interconnected pore structure and partial graphitization. The interconnected pore structure provided a rapid ion transport pathway.[117] Graphene-like nanosheets endowed carbon fibers with high electron mobility due to its zero-gap semiconductor nature.[261]

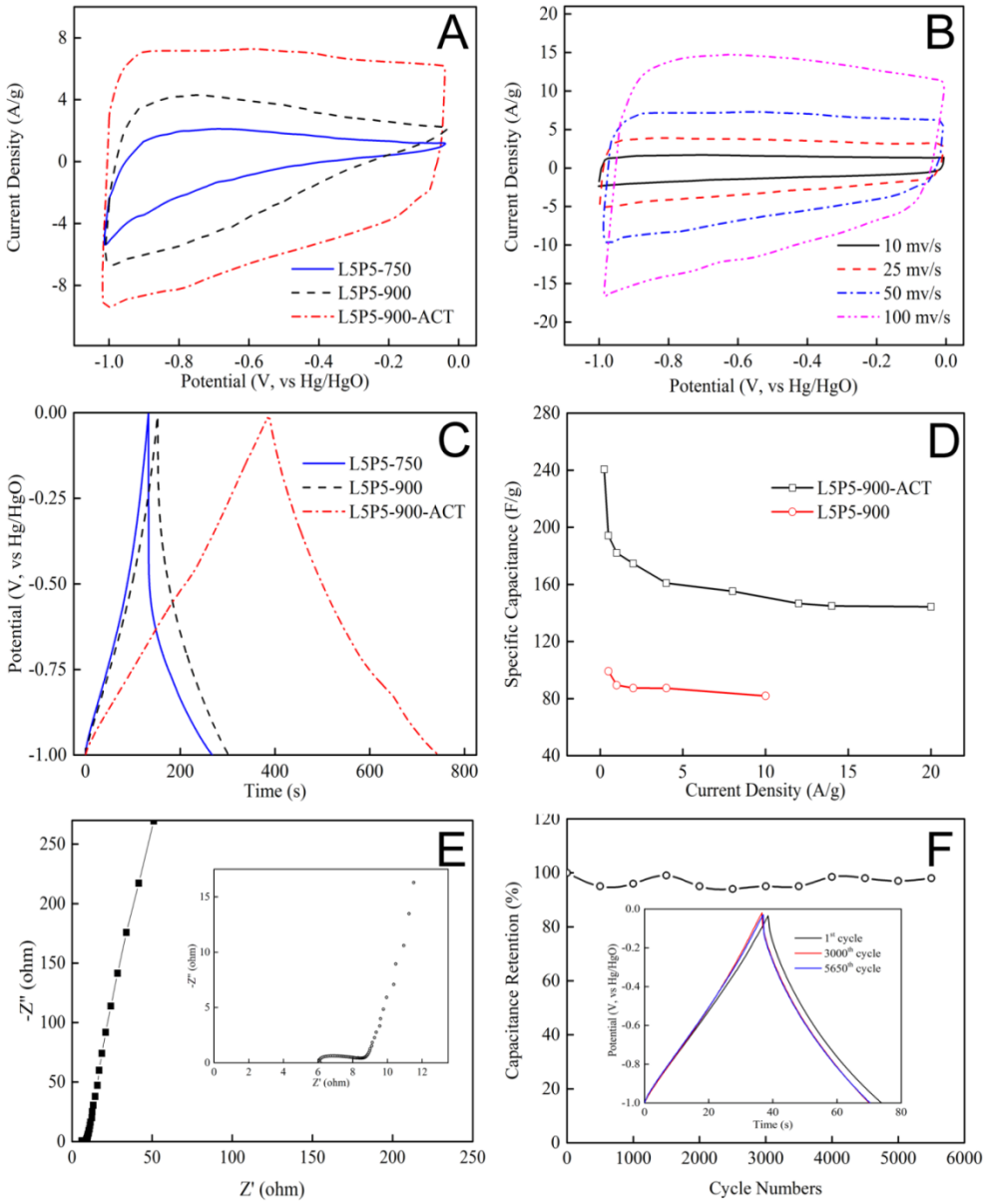

Figure 4-5 (A) CV curves of L5P5-750, L5P5-900 and L5P5-900-ACT at scan rate of 50 mV/s; (B) CV curves of L5P5-900-ACT at different scan rates from 10 mV/s to 100 mV/s; (C) galvanostatic charge-discharge curves of L5P5-750, L5P5-900 and L5P5-900-ACT at current density of 0.5 A/g; (D) specific capacitance of L5P5-900 and L5P5-900-ACT as a function of current density; (E) EIS Nyquist plots of L5P5-900-ACT (inset is the high and medium frequency regions); (F) cyclic stability of L5P5-900-ACT at current density of 4 A/g.

The electrochemical performance was further evaluated by the galvanostatic charge-discharge test. The charge-discharge curves of L5P5-750, L5P5-900 and L5P5-900-ACT were obtained at a current density of 1 A/g within -1 to 0 V in 6 M KOH solution. The symmetrical triangle shape of the charge-discharge curve demonstrated the reversible capacitive behaviour of L5P5-900-ACT. The specific capacitances were further calculated based on the discharging time at different current densities. The specific capacitance of L5P5-900-ACT was about 240 F/g at a current density of 250 mA/g. The capacitance per surface area of L5P5-900-ACT was calculated to be 31.2 $\mu F/cm^2$, which surpassed many carbon materials with similar loading weight of active materials per area reported recently as shown in Table 4-1 and also the theoretical EDLC capacitance of carbon (10-25 $\mu F/cm^2$).[105, 115, 134, 141] The nitrogen content of L5P5-900-ACT was 4%. Among these, 68% of nitrogen atoms belonged to pyridinic N and pyrrolic N which significantly contributed pseudocapacitance to the carbon surface.[119] L5P5-900-ACT is especially favourable for large scale applications, especially for design of highly compact electric power source, since L5P5-900-ACT can provide higher capacitance per surface area.[105] The specific capacitance decreased as the current density increased and reached a platform at about 4 A/g. This was due to the limited diffusion of electrolyte ion into the deep pores at high current rate.[122]

Table 4-1 Comparison of the specific capacitances of some carbon fibers materials reported previously

Samples	Electrolytes	Specific capacitance
KOH activated graphene [262]	BMIM BF_4 /AN	6.9 μF/cm^2 at 1.4 A/g
Carbon from pistachio nutshell [263]	1 M $TEABF_4$ EC-DEC	20.1 μF/cm^2 at 2 mV/s
N-doped hollow carbon nanofibers [264]	6 M KOH	28.1 μF/cm^2 at 0.2 A/g
N-doped carbon fibers from protein-lignin (This work)	6 M KOH	31.2 μF/cm^2 at 0.5 A/g

Electrochemical impedance spectroscopy (EIS) is a powerful technique for characterizing the properties of electrode-electrolyte interfaces of supercapacitors and provides information about the internal resistance of the electrode materials and the resistance between electrode and electrolyte.[123] The EIS of L5P5-900-ACT was tested from 10^{-2} to 10^5 Hz and the resulting Nyquist plots of L5P5-900-ACT were shown in Figure 4-5 E. In the low frequency region, a straight vertical line was obtained, indicating a capacitive behaviour of L5P5-900-ACT carbon sample. The projected length of Warburg-type line (the slope of the 45° portion of the Nyquist plots) on Z' axis was widely accepted to demonstrate the characterization of ion diffusion process in the electrode. The Warburg-type line of L5P5-900-ACT was rather short, directly proving that the carbon material had a short electrolyte diffusion pathway due to its hierarchical porous structure, which is important for a low ion-transport resistance, high rate capability and power density.[117]

To explore the potential of L5P5-900-ACT as supercapacitor material, the charge-discharge cyclic stability of L5P5-900-ACT was tested at a current density of 4 A/g. As exhibited by Figure 4-5 F, 95% of the initial capacitance was maintained after over 5,500 charge and discharge cycles and the shapes of the galvanostatic charge-discharge curves varied only slightly. This result indicated that L5P5-900-ACT carbon material had excellent long term charge-discharge cyclic stability, which would make it feasible for use in many industrial and personal applications.

4.4 Conclusions

This is the first time that a convenient method has been developed to prepare nitrogen-doped carbon fibers from plant proteins (hordein and zein) and lignin with a high energy storage capacity. These carbon fibers possessed a specific capacitance of 31.2 $\mu F/cm^2$ in 6 M KOH and 95% capacitance retention after 5,500 charge-discharge cycles. These excellent electrochemical properties were due to the well-engineered characteristics of the materials, including a hierarchical porous texture, an interconnected fiber network, a large amount of heteroatomes (nitrogen and oxygen), and the graphene-like nanosheet structure. Carbon fibers derived from plant protein and lignin electrospun fabrics have the potential to be used as new and effective energy storage devices. Environmentally sustainable industrial applications could be developed from this technology, such as portable electronic devices, hybrid electric vehicles and the management of large scale power systems.

Chapter 5

Plant proteins - nitrogen-doped porous graphitic carbon fibers for supercapacitor

5.1 Introduction

Rapidly growing markets for portable electronic devices and hybrid electric vehicles are demanding components be made from renewable and recyclable materials. High performance energy storage systems made from natural materials have attracted attention accordingly, in both academic and industrial fields. A supercapacitor is an electrochemical energy storage device with high power density and rapid charge-discharge rate, and has the potential to fill the gap between the battery and the conventional capacitor. However, the energy density of supercapacitor still needed to be improved.[100, 122] Among supercapacitors, the electrochemical double layer capacitor (EDLC) is popular and commercially available, and stores energy by reversible electrostatic accumulation of ions on the surface of porous electrodes.[104]

Carbon is widely used as a supercapacitor material, especially the EDLC, due to its high cyclic stability, good electronic conductivity, low cost, and wide operating temperature range.[105] Versatile carbon structures, such as carbon fibers, aerogels, tubes, sheets and particles,[105] have been developed to adapt to various applications and achieve better energy storage performance.[123] Porous graphitic carbons possess excellent features for both porous carbon and graphene, and show promise for use as supercapacitor electrode materials. The porous structure

provides a high specific surface area and increases the accessibility of electrolytes to the micropores, whereas the graphitic structure endows excellent intrinsic in-plane electrical conductivity and low resistance ion transport pathways.[262, 265, 266] Porous graphitic carbons are normally prepared by 'top-down' methods, which usually require several steps of exfoliation and activation. These processes may result in high cost, low yields and contamination of strong acid and/or alkaline reagents in the final products.[137, 262] More recently 'bottom-up' methods have been applied to generate porous graphitic carbons from graphitizable precursors through a high temperature treatment (>2500°C) or from graphitizable/non-graphitizable materials with moderate thermal treatments and catalysts, such as Fe, Ni, Co.[133, 244, 266] Raw materials include various biomass and synthetic precursors, such as coconut shell[137], corn stalk[267] and resin[244] that can all form graphitic structures after carbonization.

Besides a well-tailored architecture, surface chemistry also plays an important role in determining the capacitance of carbon-based EDLCs.[102] Introducing heteroatoms, such as nitrogen, oxygen, boron and sulfur, to the carbon matrix has proven effective to enhance the specific power density and energy density of EDLCs. Here, the heteroatomic functional groups serve to provide pseudocapacitance by Faradic redox reactions and/or chemisorptions, as well as to increase the wettability of the carbon surface.[102, 122, 123] Nitrogen - one of the most popularly studied heteroatoms - can be incorporated by *in situ* synthesis using N-rich precursors and/or by chemically treating carbonaceous materials with N-reagents.[119]

Proteins are one of the most abundant biomaterials around the world, and the N and O on the polypeptide chains can be preserved and embedded in the carbon matrix during the carbonization procedure. Thus, proteins are interesting materials to prepare heteroatom-doped carbon by facile and eco-friendly methods.[122, 138] Cho *et al.* [245] recently revealed that silk proteins can form a sp^2-hybridized carbon hexagonal structure at 350°C with a highly ordered graphitic structure after high temperature treatments, such as 2800°C. This phenomenon may be attributed to the secondary structure of protein. For example, intermolecular β-sheets are formed by two or more polypeptide chains through hydrogen bonds between the amide proton and carbonyl oxygen on adjacent chains. During carbonization, chains in β-sheet structures may achieve aromatization through intermolecular dehydration and/or condensation between adjacent chains.[140, 245] In spite of their theoretical potential, practical attempts to develop carbon materials with porous graphitic structure from proteins have been unsuccessful.

Zein and hordein are two of the most abundant and affordable cereal proteins, and are stored in corn and barley grains, respectively. Zein is a by-product of corn starch processing and a major co-product of corn fermentation.[233] Hordein is a by-product of barley starch and β-glucan extraction.[2] Both of these proteins are hydrophobic and can be dissolved in acetic acid. Their mixture can form electrospun nanofibers with good tensile strength without the addition of synthetic polymers - a feature conferring these proteins an advantage compared to most other plant proteins.[28] One challenge using proteins as a carbon precursor is to be able to maintain the nanofiber structure during carbonization without unfolding and melting the structure during

pyrolysis.[245] In the leather manufacturing industry dating back to ancient times, metal ions were added to 'fix' the leather. This process is now known to involve a metal-collagen protein interaction that gave the product better mechanical strength and thermal stability.[268-270] As inspired by metal stabilization concept of leather processing, this study proposed to add calcium salt to the plant protein electrospinning dope. During electrospinning, hordein molecules have an extended and flexible conformation and interact with each other to form nanofibers.[93] Ca^{2+} may modify the protein nanofiber bundles to increase their thermal stability during carbonization, as metal ions do in leather preparation. Also, the addition of Ca^{2+} may influence the conductivity and viscosity of the protein electrospinning dope and consequently modulate the diameter of the protein fibers.[271, 272] Calcium acetate can serve as a template to generate pores on carbon samples and is easily washed away after carbonization. For these reasons, calcium acetate was selected to facilitate the conversion of protein nanofibers into carbon nanofibers in this research.

The objective of this study is to convert barley proteins based electrospun nanofibers fabric into N-doped carbon fibers with 3D interconnected hierarchical porous structure as electrode materials for supercapacitor. The influence of Ca^{2+} on protein nanofiber diameter and morphology was investigated, and X-ray photoelectron spectroscopy (XPS) was used to study N and O functional groups on the carbon surface. The feasibility of using these carbon samples as supercapacitor electrode materials is evaluated and discussed.

5.2 Materials and methods

5.2.1 Materials

Barley grains (Falcon) were kindly provided by Dr. James Helm of Alberta Agriculture and Rural Development, Lacombe, AB, Canada. Hordeins were extracted from barley grains using an ethanol solution according to a procedure reported in our previous work.[18] Zein (F4000, 92% protein content) was kindly provided by Freeman Industries LLC (New York, NY, USA) and used without further purification. Calcium hydroxide, polyvinylidene fluoride (PVDF, molecular weight ~275,000 by gel permeation chromatography), N-methyl-2-pyrrolidone (NMP) and acetic acid were purchased from Sigma-Aldrich Canada Ltd (Oakville, ON, Canada). Glutaradehyde solution (50%) and carbon black Super P was obtained from Fisher Scientific (ON, Canada) and Alfa Aesar (Ward Hill, MA, US), respectively. All chemicals were used as received unless otherwise specified. Ultrapure water purified using a Milli-Q Advantage A10 system (EMD Millipore Corporation, MA, USA) was used to prepare electrolyte solution.

5.2.2 Preparation of plant protein-calcium electrospun fabrics

To prepare the protein-calcium acetate mixture for electrospinning, a desired amount (2 to 12%, w/v) of calcium hydroxide was slowly added to 2 mL acetic acid solution (90%, v/v) and stirred for 2 h to form calcium acetate. Plant protein solutions (18%, w/v) were then prepared by dissolving protein powders (hordein:zein=50:50, w/w) in the acetic acid solution with calcium acetate, and stirred for 12 h at 25°C. The electrospinning experiments were carried out by a

customized digital electrospinning apparatus EC-DIG (IME Technologies, Eindhoven, Netherlands) at 25°C. Solutions were forced through a blunt needle with a diameter of 0.8 mm at the flow rate of 1 mL/h. The spinning voltage was fixed at 20 kV and the needle to collector distance was 20 cm. The electrospun fiber fabrics were collected on a rotary collector with a rotating speed of 1 rpm. The electrospun protein-calcium fibers were cross-linked by placing on a pan flowing above 200 mL of 25% (v/v) glutaraldehyde solution in a sealed glass container for 6 h at room temperature.[273]

5.2.3 Carbonization

The carbon fibers were synthesized by one-step carbonization of the protein and calcium acetate electrospun fiber fabrics by heating in a tubular furnace (GSL-1100X-NT-UL, MTI Corporation, CA, US). In a typical experiment, the carbonization step was operated under continuous argon flow with the following heating procedure: (1) the temperature was raised from 25 to 200˚C at a rate of 5˚C/min; (2) the temperature was held at 200˚C for 2 h to stabilize the protein-Ca^{2+} electrospun fibers; (3) the temperature increased from 200 to 300˚C at a rate of 1˚C/min to have a slow thermo decomposition of proteins and calcium acetate; (4) the temperature continued to increase from 300 to 850˚C at 5˚C/min; (5) the carbonization temperature was held for 2 h; (6) the sample was cooled down naturally under argon flow. Finally, the carbon sample was immersed in 2 mol/L hydrochloride solution to remove the calcium oxide and other soluble substrates, and then rinsed with water and dried at 100˚C under vacuum. The carbon samples

derived from electrospun fiber fabrics with varied amounts of calcium hydroxide were coded as P-4%Ca, P-8%Ca, P-10%Ca and P-12%Ca, respectively. The cross-linked sample was suffixed with CL. For example, the carbon fiber sample derived from cross-linked electrospun fabric made with 10% $Ca(OH)_2$ was named P-10%Ca-CL.

5.2.4 Fiber size and morphology observation

The exterior morphology of the original fiber and the carbon fiber samples were observed by a Hitachi X-650 scanning electron microscope (SEM, Hitachi, Japan) at 20 kV. The original fiber samples were sputtered with gold before observation. High resolution transmission electron microscope (HRTEM, JEOL 2100, JEOL Inc., US) was used to study the inner microstructure of carbon fiber samples. For this, samples were ground into powder before deposition onto the 300 mesh Cu/Pd grids for observation.

5.2.5 Fiber textural characterization and chemical analysis

Thermogravimetric analysis (TGA) of the original protein fibers was conducted by a thermogravimetric analyzer (TA Instruments, Q500, New Castle, DE, US) under argon with a heating rate of 2^{o}C/min. For analysis of chemistry composition of the carbon surface, X-ray photoelectron spectroscopy (XPS) was obtained by an Axis Ultra spectrometer (Kratos Analytical, Manchester, UK) with X-radiation Al Kα ($h\nu$ = 1486.6 eV). The C 1s, O 1s and N 1s core levels were fitted using the CasaXPS software. The N and C contents of the original fibers were measured by the Leco nitrogen analyzer (FP-628, Leco, St. Joseph, MI, US). AutosorbiQ

(Quantachrome Instruments, Boynton Beach, FL, US) was employed to measure the N adsorption-desorption isotherm, specific surface area and the porous texture at 77 K. The specific surface area and pore size distribution was calculated based on the Brunauer-Emmett-Teller (BET) theory and the Barrett-Joyner-Halenda (BJH) model, respectively with the AutosorbiQ's associated software (ASiQWin). To analyze the crystallinity of carbon sample, X-ray powder diffraction (XRD) patterns were obtained using a Bruker AXS D8 Discover diffractometer (Bruker Coperation, East Milton, ON, CANADA) with the Cu Kα radiation (λ = 1.541841 Å) at 40 kV and 44 mA (2θ was from 10 to 80°). Raman spectra were obtained to analyze the carbon structure by a Nicolet Omega XR Raman microscope (Thermo Fisher Scientific, Waltham, MA, US). The excitation wavelength of the near infrared laser was set at 532 nm and data points were recorded at 0.5 cm^{-1} interval.

5.2.6 Electrochemical performance in 6 M KOH

To measure the electrochemical properties, each activated carbon sample derived from plant protein electrospun fiber fabrics was ground and mixed with a 10 wt% carbon black and 10% PVDF binder (10 wt% in NMP) to form a paste. The paste with 8mg active carbon sample was cast onto a 1.0 cm^2 piece of nickel foam. Then, the carbon sample was dried under vacuum at 120^oC for 12 h and pressed under 2,000 psi by a bench top laboratory press (model 3851, Carver Inc., Wabash, IN, US) to fabricate an electrode. To assemble a three-electrode cell, the above nickel foam, a Pt wire, and an Hg/HgO were used as working, counter and reference electrodes,

respectively. All electrochemical properties were analyzed by a Solartron 1287 electrochemical interface (Solartron Analytical, Berwyn, PA, US). Cyclic voltammetry studies were performed in the potential window of -1.0 to 0 V vs. reference electrode at various scan rate from 5 to 100 mV/s. Galvanostatic charge-discharge curves were measured with current density from 0.5 to 10 A/g. The specific capacitance of carbon materials were calculated by the following equation:

$$C = \frac{I\Delta t}{m\Delta V}$$

Where I(A)is the discharge current, Δt stands for the discharging time, m (g) is the weight of carbon sample loaded on the working electrode, and ΔV represents the potential window. Electrochemical impedance spectroscopy (EIS) was performed in a frequency range from 10^{-2} to 10^{5} Hz with 5 mV amplitude.

5.2.7 Statistical analysis

All experiments were performed at least in three independent batches. For SEM and TEM results, one typical image was presented respectively. For nitrogen adsorption-desorption isotherm, TGA, Raman spectroscopy, XRD, XPS and electrochemical analysis, one typical curve was presented respectively. For data in figures, error bars represents the standard deviation (n = 100). Statistical evaluation was conducted by analysis of variance (ANOVA) using SAS (SAS Institute, Inc., Cary, NC). Statistical differences between samples were performed with a level of significance of p<0.05.

5.3 Results and discussion

5.3.1 Morphologies of the plant protein-calcium fibers

Figures 5-1 A-D show the morphologies of the plant protein-calcium nanofibers and the mean diameter of the fibers were summarized in Figure 5-1 F. Plant proteins can be fabricated into nanofibers with a smooth surface and controllable diameter by electrospinning in the presence of 4-10% of Ca^{2+}, although some tiny flocculent fibers appeared as the calcium concentration increased to 8 and 10%. Increasing Ca^{2+} to 12% resulted in a conspicuous irregular beads-on-string structure in the nanofiber fabrics. The mean diameters of fibers decreased from 992 to 413 nm as Ca^{2+} increased from 4 to 10% and then leveled off from 10 to 12%. Similar to some synthetic polymers, such as poly(acrylic acid) and poly(lactic acid) the addition of ions can lead to an increase of the charge density in the spinning dope causing the electrospinning jet to carry more electric charge. Thus, in the strong electric field, the spinning jet may bear stronger elongation forces and produce fibers with smaller diameters.[272, 274]

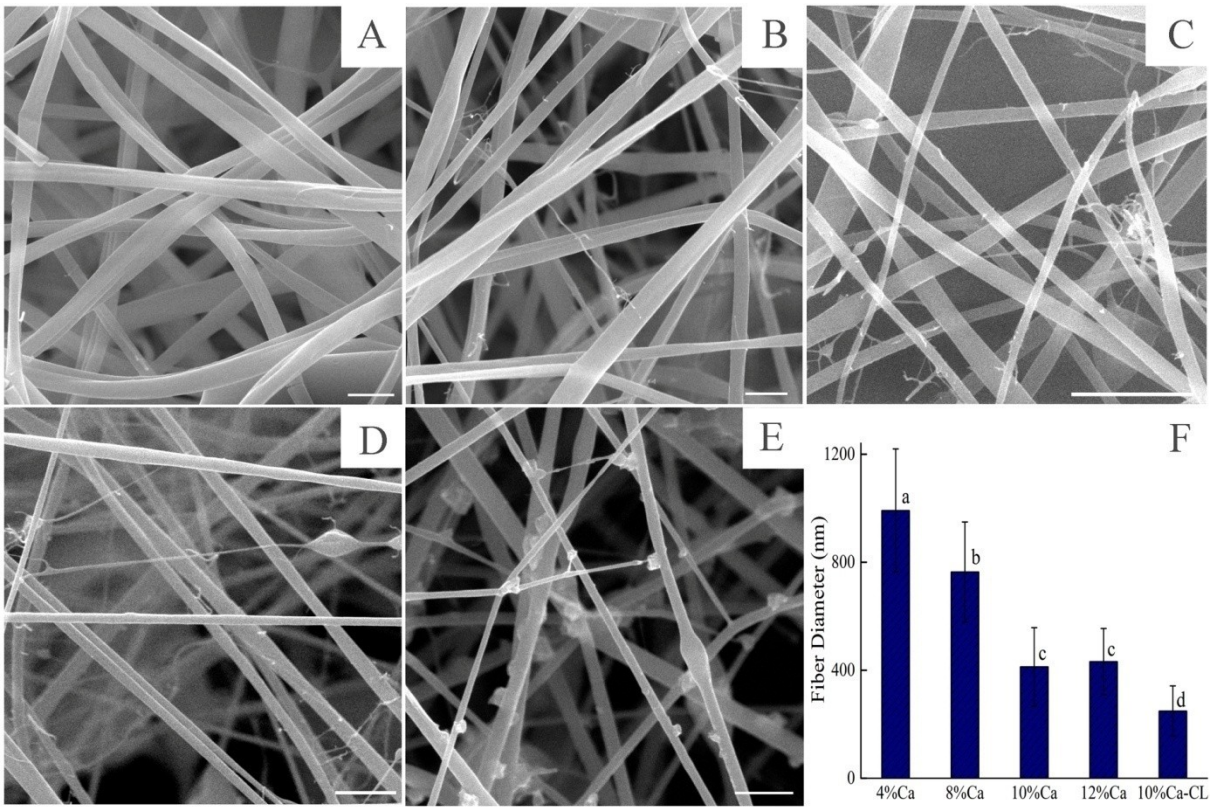

Figure 5-1 SEM images of original plant protein-calcium electrospuns fibers: (A) protein-4%Ca; (B) protein-8%Ca; (C) protein-10%Ca; (D) protein-12%Ca; (E) protein-10%Ca after cross-linked by glutaraldehyde. Scale bars are 5 μm. Figure 5-1 F shows the mean fiber diameter of 5 original fibers. Different letters above bars indicate significant difference (p<0.05) in fiber diameters.

Protein fibers with 10% Ca^{2+} were selected for cross-linking since they had smallest mean diameter with minimal beads providing a higher specific surface area. The porous nanofiber fabric structure was well maintained after glutaraldehyde treatment and the mean fiber diameter decreased. Small particles were observed on the cross-linked fibers, which may represent the hygroscopic calcium acetate. Glutaraldehyde can chemically bond two adjacent amino acid residues by reacting with several functional groups such as amines, thiols, phenol and

imidazoles.[275] Glutaraldehyde vapour has been applied to protein electrospun fibers, such as collagen and gelatine, to achieve better mechanical properties and lower their swelling ratio in aqueous solution.[273, 276] In this study, cross-linking of protein-Ca fibers by glutaraldehyde may have beneficial effects by sustaining the fibrous structure during the carbonization process and increasing protein-protein interactions.[142]

5.3.2 Morphologies of the carbon samples derived from protein-calcium fibers

The TGA test was conducted to determine the influence of Ca^{2+} on the conversion of protein fibers to carbon fibers and their subsequent morphology. As shown in Figure A2-1 in Appendix A2, the protein-calcium nanofibers experienced several steps of decomposition during heating from 25 to 850˚C. For protein nanofibers alone, the decomposition started at around 200˚C and the rate levelled off at about 500˚C with approximately 80% of the initial weight loss. A more complex decomposition process was observed for the protein-calcium fibers, due to the multiple-step conversion of calcium acetate (CA) into calcium oxide.[277] CA dehydrates and loses crystal water from 90 to 180˚C, and then decomposes into calcium carbonate and acetone in the second step at around 300 to 400˚C, together with the decomposition of protein. Finally, the calcium carbonate decomposes into calcium oxide and carbon dioxide at about 590˚C. Carbon dioxide and other volatiles molecules gradually released during heating may partially oxidize adjacent carbon[278] and create pores on the fibers, leading to an increased specific surface area of the carbon sample.

As shown in Figure 5—2, after carbonization, proteins melted and most of fibers fused together when Ca^{2+} was 4%. When the Ca^{2+} increased to 8%, the nanofiber structure was partially sustained, although some fibers were fused and swollen. Notably, P-10%Ca showed homogeneous, smooth and flexible carbon fibers after carbonization. No fibrous structure was observed when the Ca^{2+}concentration was further raised to 12%. This indicates that Ca^{2+} plays an important role in maintaining the protein fibrous structure during the carbonization process at high temperatures. When dissolved in the electrospinning solution, hordein unfolded into an extended conformation in acetic acid, which exposed carboxyl groups to the protein surface.[93] This promoted protein intra and intermolecular interactions[279, 280] bridged by Ca^{2+} during electrospinning. The increased protein-protein interactions resulted in an increase of activation energy and consequently improved the thermal stability of plant protein nanofibers.[281] Moreover, during the increase of carbonization temperature, calcium acetate decomposed into calcium carbonate and further into calcium oxide. Calcium carbonate and calcium oxide sintered into a solid fibrous framework, which may have restricted the melting of protein.[282-284] Thus, calcium could help proteins convert into solid carbonaceous materials without melting to shapeless liquefaction and losing fibrous structure. However, excess of calcium led to the formation of large salt particles which expanded extensively during carbonization and destroyed the continuous protein fiber network, resulting in irregular fiber morphology.[282, 285] As compared to P-10%Ca, the carbon material obtained from glutaraldehyde cross-linked protein-10% Ca^{2+} fibers (P-10%Ca-CL) had a more continuous and interconnected structure with less rupture. The

3D interconnected fibrous network of P-10%Ca-CL is more favourable than the separated fiber network of P-10%Ca since a continuous network facilitates the electron transportation and reduces the contact resistance. Usually, carbon fibers have excellent electronic conductivity along the fiber axis. However, due to the large distance among fibers, carbon fibers have contact resistance, which can limit their performance.[100] Meanwhile, the macropores formed by interlaced carbon fibers can serve as ion-buffering reservoirs and can minimize the diffusion distances of ions to the interior surfaces.[240] This then contributes to a lower diffusive resistance, higher rate capacitance and power density of the carbon materials.[117] For these reasons, the structure of P-10%Ca-CL was superior to P-10%Ca and was selected for the further experiments.

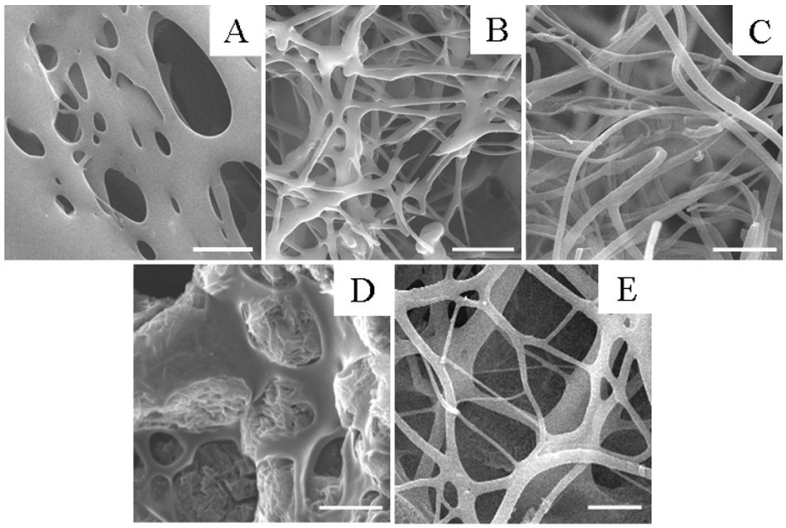

Figure 5-2 SEM images of carbon samples derived from plant protein-calcium electrospun fibers at 850°C: (A) P-4%Ca; (B) P-8%Ca; (C) P-10%Ca; (D) P-12%Ca and (E) P-10%Ca-CL. Scale bars: 2.5 μm.

5.3.3 Chemical characterization and porous structure of P-10%Ca-CL

A large proportion of heteroatoms, such as nitrogen, improves the wettability, electronic conductivity and capacitance of carbon.[102, 123] X-ray photoelectron spectroscopy (XPS) was used to verify whether N and O originally from protein could be retained in the carbon samples after carbonization. The survey spectra in Figure 5-3 A and Figure A2-2 in Appendix A2 indicates that C 1s, N 1s, O 1s and trace amount of unwashed Ca (at around 347 eV) existed in the P-10%Ca-CL, P-10%Ca and P-12%Ca carbon samples, respectively.[286] The percentages of C, N and O in carbon samples were summarized in Table 5-1 as measured by XPS. The N content of the original fibers was around 15 wt% as measured by combustion using the Leco nitrogen analyzer. During carbonization, part of the heteroatoms, including N, O, H and S in the amino acid residues turned into volatile molecules. In P-10%Ca-CL sample, 6-7 at% (atomic percentage) (7-8 wt%) of N was retained after carbonization. P-10%Ca-CL had higher C content and lower N content than P-10%Ca. This could be explained by the incoperation of glutaraldyhyde ($C_5H_8O_2$) which does not contain any nitrogen. The N content in the P-10%Ca-CL sample is lower in nitrogen than carbon fibers made from synthetic polymer polypyrrole (10%), but surpasses those made from raw biomass such as human hair[122], silk cocoon[141] and gelatine[142], indicating that carbonization of plant-protein is an effective method to prepare nitrogen-doped carbon fibers.

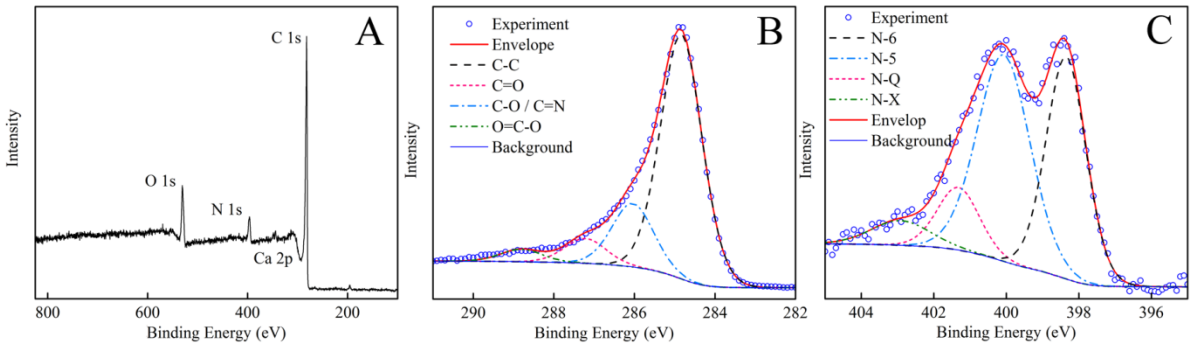

Figure 5-3 XPS of P-10%Ca-CL sample. A is the survey spectra. B and C are the deconvoluted C 1s and N 1s peaks, respectively.

Table 5-1 Element composition information of plant protein-calcium derived carbon samples.

Samples	C (%)*	O (%)*	N (%)*
P-10%Ca	84.3	8.2	7.5
P-10%Ca-CL	85.9	7.7	6.4
P-12%Ca	91.2	2.3	6.5

* atomic ratio from XPS

The nitrogen functional groups of P-10%Ca-CL were further investigated by deconvolution of the N 1s peak. As shown in Figure 5-3 C, four types of N groups were observed in the P-10%Ca-CL sample, namely pyridinic N (N-6) at 398.4 eV, pyrrolic/pyridine N (N-5) at 400.0 eV, quaternary N (N-Q) at 401.1 eV and oxidized N (N-X) at 402.6 eV.[256, 287] N-6 and N-5 contributed 41.7 and 35.6% of the total N, respectively, followed by N-Q (17.6%). N-6, N-5 and N-X are the N groups located at the edges of graphite plane, which are more active than those in the middle of graphite plane (N-Q).[256] Moreover, it has been reported that N-6 and N-5

contributed positively to the capacitance performance of carbon materials through faradaic reaction based pseudocapacitance, while N-Q enhanced the electronic conductivity by assisting electron transfer through the carbon.[119, 120] Additionally, C 1s spectrum could be fitted into 4 peaks centered at 284.8 eV (70.8 at%), 286.0 eV (18.4 at%), 287.2 eV (7.2 at%) and 288.8 eV (3.6 at%), which are assigned to sp^2 C=C/sp^3 C-C graphitized carbon, carbon in phenolic alcohol ether (C-O), carbon in carbonyl or quinone group (C=O), carbon in carboxyl group (O=C-O) and carbon in carbonate groups, respectively. Based on their hydrophilic nature, oxygen functional groups could improve the wettability between electrode and electrolyte.[119] Also, the quinone group (C=O) contributed to the capacitance of carbon materials through reversible oxidation/reduction reactions.[119, 120]

Figure 5-4 and Figure A2-3 in Appendix A2 show the microstructure of the ground P-10%Ca-CL and P-10%Ca samples, respectively. Amorphous porous structure and aligned graphitic layers structure were both observed on carbon fibers with HR-TEM. The inset of Figure 5-4A clearly showed the existence of pores in meso and micro range with split or irregular shapes. The interconnected split-shape pores worked as channels for transportation and penetration of electrolyte ions inside the carbon fibers. It is interesting to observe both ordered stacking graphitic nanosheet structure and onion-like carbon structure in the P-10%Ca-CL sample, as shown in Figure 5-4 B. The onion-like carbon structure is considered to be quasi-spherical nanoparticles consisting of concentric graphitic shells.[288] Protein based biomaterials had the potential to form partially aligned graphitic structure as shown in Chapter 4, as well as one study

on silk protein based carbon materials,[142, 245] but this is the first time that such highly ordered spherical graphitic structure is reported within carbon fibers derived from biomass. For onion-like carbon, the surface area is fully accessible to ion absorption.[289] The large graphitic nature and abundant external surface area provides onion-like carbon high potential to be used for fast charge and discharge applications.[104] Also, due to the positive surface curvature, the onion-like carbon structure facilitates electrical double layers and a reduced electrical field near the spherical surfaces and can lower the driving force for counter-ion absorption and co-ion desorption.[104, 290] Thus, the onion-like carbon electrode may have the potential to exhibit high power density.[104] The graphitic structure can further benefit the carbon electrode with its excellent intrinsic in-plane electrode conductivity.[291] As compared to the conventional methods for making porous graphitic materials, which use high energy input and/or corrosive chemicals, this study has provided a convenient and cost-effective route to prepare porous graphitic structure at a relatively low temperature of 850°C.

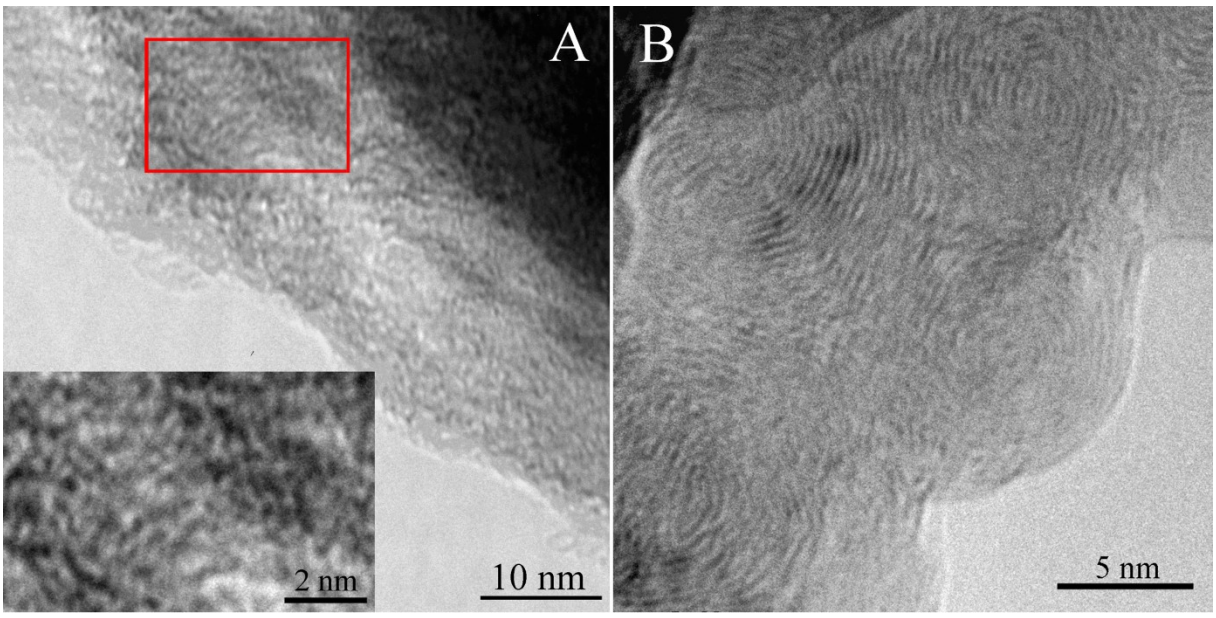

Figure 5-4 TEM images of ground P-10%Ca-CL carbon nanofibers of different magnifications. Inset of Figure 5-4 A is the magnified image of the selected area.

Figure 5-5 shows the X-ray powder diffraction (XRD) patterns and Raman spectra of the P-10%Ca-CL carbon sample. Both results provided support to the conclusion that the graphitic structure existed in the P-10%Ca-CL sample. Two major peaks were observed on the XRD pattern (Figure 5-5 A). The peak centered at a 2θ of 24.3° was assigned to the (002) plane of graphite, while the peak at about 44.0° corresponded to the (100) crystal plane.[130, 292] Based on the θ of (002) plane, the layer-to-layer distance (d-spacing) between bent graphitic layers was calculated by the following equation:

$$d_{002} = \lambda/(2\sin\theta_{002})$$

Here, λ is the wavelength of X-ray used in experiments. Thus, the d_{002} of the graphitic layers in P-10%Ca-CL is 0.37 nm, which is slightly higher than that of natural graphitic carbon lattice at

0.34 nm.[242] The larger spacing could possibly be due to the presence of oxygen and nitrogen functional groups on the graphitic plane or other structural defects.[250] The insertion of O and/or N causes changes of the reacting carbon atoms from sp^2 to sp^3. The out of plane C-N or C-O covalent bonds resulted in the atomic scale roughness, thus, increased the distance between graphene layers.[251, 252] Despite this, the graphitic layers were in good order along the stacking direction. P-10%Ca and P-12%Ca carbon samples also showed similar peaks (Figure A2-4 in Appendix A2), indicating the existence of a similar graphitic structure. Hence, it was concluded that the formation of the graphitic structure was independent of glutaraldehyde cross-linking and the carbon sample morphology.

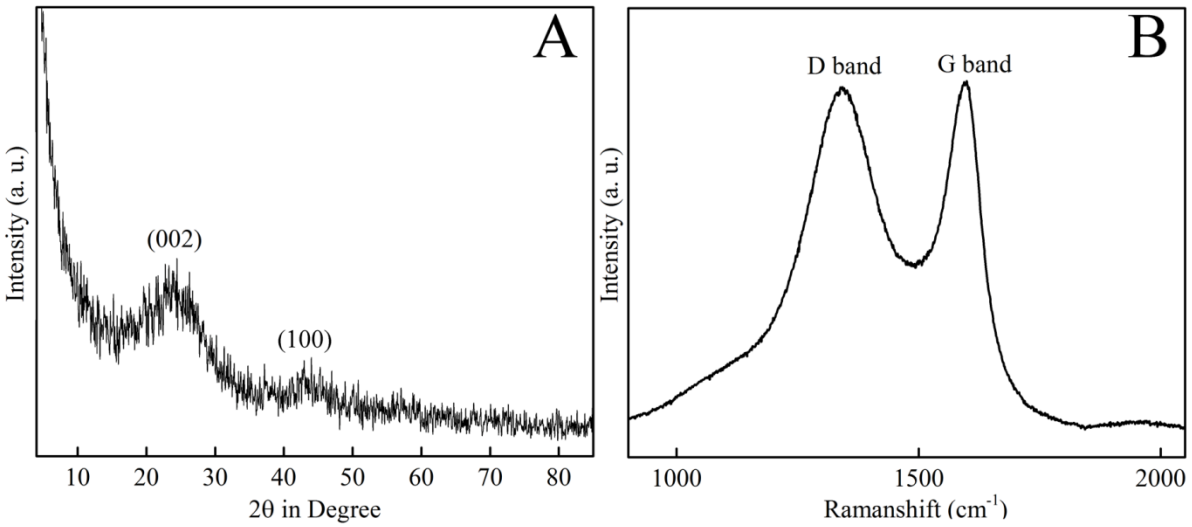

Figure 5-5 XRD pattern (A) and Raman spectra (B) of P-10%Ca-CL carbon nanofibers.

A Raman spectrum was conducted to demonstrate the distinguished ordered and disordered crystal structures of P-10%Ca-CL.[254] The G band located at about 1598 cm^{-1} and the D band at

1346 cm^{-1} were the two typical features as illustrated in Figure 5-5 B. The D band is related to defective sites or disordered sp^2 hybridized carbon of graphite, while G band corresponded to the E_{2g} phonon of sp^2 carbon atoms and serves as an indicator of graphitic structure.[266] Thus, the ratio between intensities of G and D bands, namely I_G/I_Dvalue, is proportional to the degree of crystallization of the carbon materials. The I_G/I_D of P-10%Ca-CL was calculated to be 1.02, indicating a smaller size of in-plane sp^2 domains and/or partially ordered crystal structure as compared to natural graphite. As demonstrated in Figure A2-5 in Appendix A2, P-8%Ca, P-10%Ca and P-12%Ca have G bands and D bands at similar wavenumbers. As the calcium amount increases from 8 to 10%, the I_G/I_Dvalue increases from 0.95 to 1.07, indicating that calcium may help in the formation of graphitic structure. However, when the calcium amount was increased to 12%, I_G/I_Dvalue dropped to 0.93, which may be explained by the smaller size of the in-plane sp^2 domains due to the disruptive influence of excessive calcium salt on the carbon materials.[254]

The specific surface area of P-10%CA-CL was also measured. The nitrogen adsorption-desorption isotherm and the pore size distribution are displayed in Figure 5-6. The nitrogen absorption increased largely at low relative pressure region ($P/P_0<0.01$), suggesting the existence of micropores (<2 nm).[129] Then, the isotherm continued to gradually rise in the mid pressure region. Finally, a sharp uptake occurred at a relative pressure of 0.8-1.0 and the absorption was not saturated even at P/P_0 of 0.98.There was a clear hysteresis loop at P/P_0 between 0.4 and 1.0. These results indicate the co-existence of plentiful mesopores (2-50 nm)

and macropores (>50 nm) in the fiber matrices.[141] The hysteresis loop is correlated to the capillary condensation in the mesopore structures[136, 249] and the shape of the hysteresis loop is associated with the specific pore structures.[249] Since the adsorption and desorption branches were parallel to each other from 0.4 to 0.8, the hysteresis loop of P-10%Ca-CL was considered to be Type H3, which is usually observed for samples with slit-shaped pores based on aggregates of plate-like particles.[249] The specific surface area of P-10%Ca-CL was 348.4 m^2/g as calculated by the Brunauer-Emmett-Teller (BET) method. The total volume was about 1.73 cm^3/g according to the maximum amount absorbed at P/P_0 of 0.98. The average pore diameter was around 9.9 nm. The specific surface area of P-10%Ca-CL nanofibers is comparable to some carbon nanofibers such as the carbon fibers made from lignin[131] and carbon fibers made from polyacrylonitrile[271], but smaller than those of active carbons (on the order of 1000 m^2/g).[102] This may be due to the formation of granular like graphitic structure. It is known that graphitization could reduce the specific surface area of carbon materials dramatically.[289, 293] The pore size distribution was analyzed based on the desorption branch of the isotherm by the Barrett-Joyner-Halenda (BJH) method. In the micropore region, a sharp peak is located at round 1.9 nm followed by a smaller peak at 8.7 nm in the mesopore region. The macropores formed by the interlaced fibers was too large to be calculated by this model. This result is in agreement with the observations based on SEM and TEM images, confirming that P-10%Ca-CL has well developed hierarchical pore structures at micro, meso and macro range. This hierarchical pore structure can enhance the supercapacitance performance since micro and mesopores provide high accessible surface area

for larger capacitance, while interconnected meso and micropores facilitate ion transport to ensure high rate capability and power density.[117]

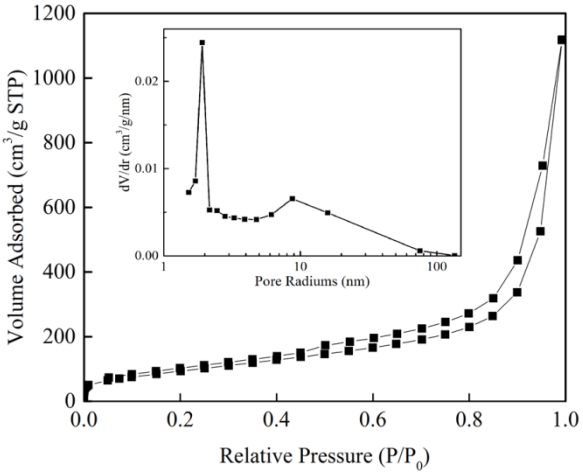

Figure 5-6 Nitrogen adsorption and desorption isotherm and pore size distribution (inset) of P-10%Ca-CL.

5.3.4 Electrochemical properties

The electrochemical properties of the carbon samples were evaluated in 6 M KOH to test their performance as supercapacitor electrode materials. Figure 5-7A shows the cyclic voltammetry (CV) curves of carbon samples prepared with different amounts of calcium. CV curves of all five samples at a scan rate of 50 mV/s are in quasi-rectangular shape, indicating a double-layer capacitor nature of the charge-discharge process.[122] Also, broadened humps were observed on the CV curves of all the samples, which are considered to be caused by the redox reactions of various oxygen and nitrogen functional groups.[294] When the Ca^{2+} was increased from 4 to 10%, the specific current increased. This phenomenon could be explained in two ways: firstly, a larger amount of calcium salt led to a greater degree of activation during carbonization; secondly,

P-4%Ca did not maintain fibrous structures after carbonization, while P-10%Ca possessed a well-developed nano-fibrous structure, which permitted a greater specific surface area and hierarchical porous structure. The interconnected macropores and 3D fibrous structure of P-10%Ca facilitated the penetration and transport of electrolyte ions. On the other hand, the capacitance of P-4%Ca was limited by the poor accessibility of electrolyte ions to the pores inside the carbon. At a scan rate of 50 mV/s, P-10%Ca-CL showed the greatest specific current among all 5 carbon samples, attributed to a large ion-accessible specific surface area, a large amount of heteroatoms and interconnected nanofiber network. The CV curves of P-10%Ca-CL obtained at different scan rates are shown in Figure 5-7 B. The current density increased with the scan rate. The quasi-rectangular shape of the CV curve was maintained even at scan rates as high as 150 mV/s without distortion, which is associated to the rapid ion transport pathway formed by plentiful meso and macropores.

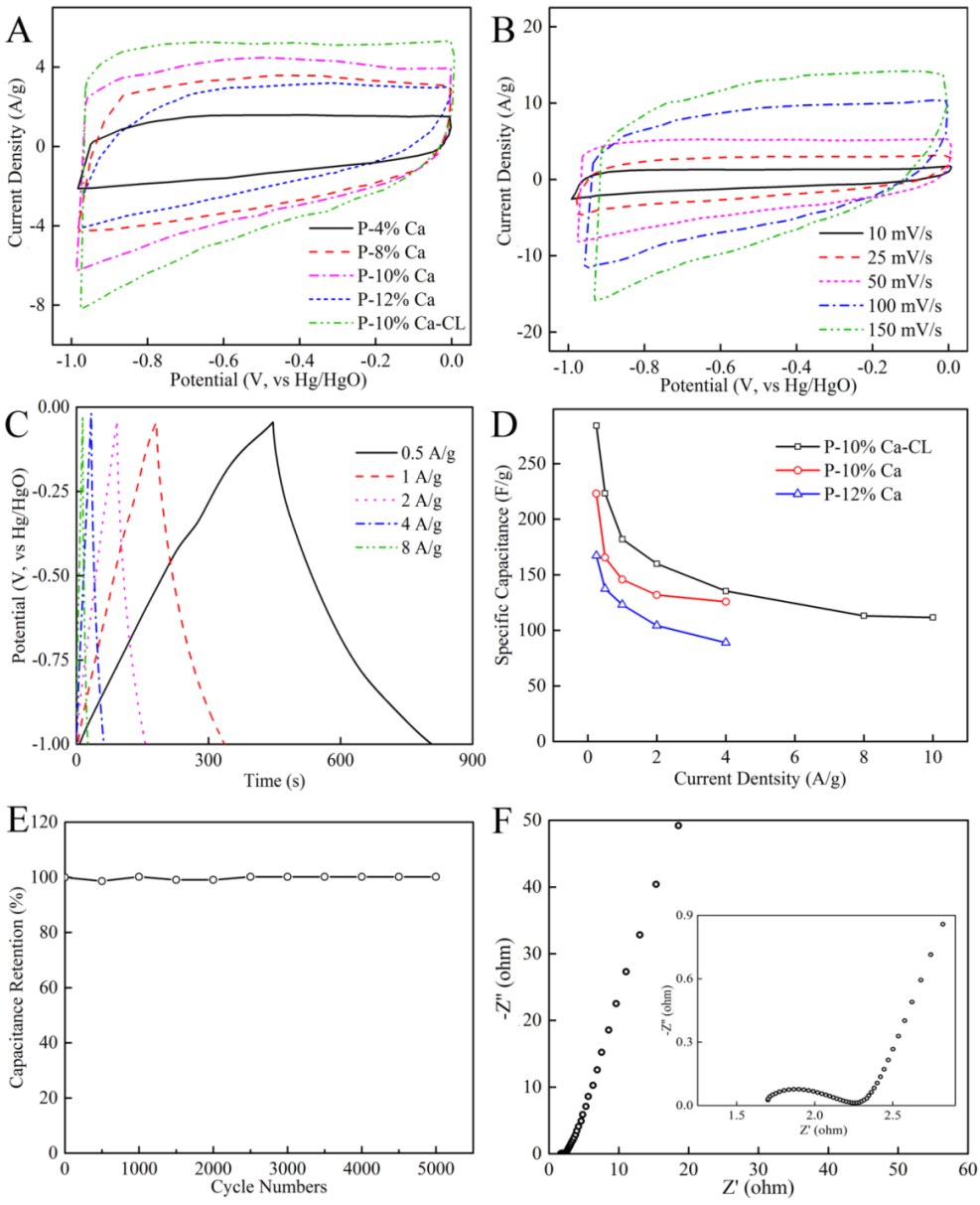

Figure 5-7 (A) CV curves of P-4%Ca, P-8%Ca, P-10%Ca, P-12%Ca and P-10%Ca-CL at a scan rate of 50 mV/s; (B) CV curves of P-10%Ca-CL at different scan rates from 10 to 150 mV/s; (C) galvanostatic charge-discharge curves of P-10%Ca-CL at different scan rates from 0.5 to 8 A/g; (D) specific capacitance of P-10%Ca-CL as a function of current density and (E) cyclic stability and capacitance retention of P-10%Ca-CL at current density of 10 A/g; (F) EIS Nyquist plots of P-10%Ca-CL (inset is the high and medium frequency regions).

A galvanotatic charge-discharge test was also conducted in 6 M KOH at room temperature. The galvanostatic charge-discharge curves of P-10%Ca-CL at different current densities were shown in Figure 5-7 C. The quasi-linear nature for P-10%Ca-CL also indicates the presence of graphitization and improvement in conductivity.[122, 295] The slight deviation at around -0.5 V and at -0.2 to -0.1 V was attributed to the pseudocapacitance effects of N and O functional groups.[122, 296] The specific capacitance of P-10%Ca-CL was calculated to be 223.4 F/g at a current density of 0.5 A/g based on the galvanostatic charge-discharge test. This is among the best capacitive performances from carbon fibers derived from synthetic polymers and/or biomass in aqueous electrolyte solutions reported in the literature.[98, 123, 124, 141, 264, 271] The areal specific capacitance of P-10%Ca-CL was calculated to be 64.1 $\mu F/cm^2$, which is greater than the theoretical capacitance of carbon (10-25 $\mu F/cm^2$)[138] and other carbon materials reported recently, such as carbon aerogels (~10 $\mu F/cm^2$), glass carbons (20 $\mu F/cm^2$) and multiwall carbon nanotubes (8.7 $\mu F/cm^2$).[100] Given the relatively small specific surface area of P-10%Ca-CL, pseudocapcitance induced by redox reaction of N and O functional groups played a major contribution to this excellent specific capacitance.[102] This is in agreement with many recent studies that showed not only specific surface area, but also the surface heteratomic functional groups, play essential roles in determining the specific capacitance of carbon materials.[102, 120, 138] The high areal specific capacitance of P-10%Ca-CL suggest its potential application on large scale devices, such as highly compact electric power sources.[105] As shown in Figure 5-7 D, with the decrease of the specific capacitance the current density increased and then levelled off at 4 A/g. Moreover,

P-10%Ca-CL had about 98% of capacitance retained after 5,000 cycles of charging-discharging, exhibiting its excellent cyclic stability and potential lifetime in an alkaline electrolyte (Figure 5-7 E). This makes P-10%Ca-CL favourable for industrial and household applications.

Nyquist plots of P-10%Ca-CL obtained from electrochemical impedance spectroscopy (EIS) test between 10^{-2} to 10^{5} Hz are shown in Figure 5-7 F, and provide information about the internal resistance of the electrode materials and the resistance between electrode and electrolyte.[131] The fast ion and electrode transport can be further confirmed by the Nyquist plots.[137] In the low-frequency region, the Nyquist plots of P-10%Ca-CL were close to vertical, confirming its electrochemical double layer capacitance nature.[297] In the middle frequency, the projected length of the Warburg-type line (the portion of Nyquist plots with a slope of 45°) on the real axis represents ion diffusion process from electrolyte to the electrode surface.[128] The Warburg lines of P-10%Ca-CL were rather short, meaning that it had short electrolyte diffusion pathways due to its partial graphitic structure[137] facilitating ion transport and the macropores serving as electrolyte reservoirs.[298] In the mid and high frequency region, the intercept on the real axis is the equivalent series resistance (ERS) and the depressed semi-circle is associated to the charge transfer impedance at the electrolyte and electrode interfaces.[137] The semi-circle of P-10%Ca-CL has a small intercept of about 1.75 ohm on the real axis. The small semi-circle was an indicator of the low charge-transfer resistance in the electrode materials, showing that P-10%Ca-CL was favourable for ion access. Both the good wettability resulting from heteroatomic functional

groups at P-10%Ca-CLsample surface[298] and its porous graphitic structure benefit the effective ion migration into the electrode.[137]

5.4 Conclusions

This work demonstrates for the first time that plant protein electrospun fabric can be converted into nitrogen-doped porous carbon nanofibers with a highly ordered granular graphitic structure by one-step pyrolysis. With the intention of supercapacitor applications, this method is cost-effective and eco-friendly since hordein and zein are abundant by-products of cereal processing industries. Also, the graphitic structure is formed at a relatively low temperature without the use of a catalyst. The optimized sample P-10%Ca-CL exhibited an interconnected carbon nanofiber network, a relatively large amount of N (7%) mainly in the form of pyridinic and pyrrolic N, and a well aligned granular graphitic structure. Due to the unique morphological and chemical properties, this carbon fiber material demonstrated excellent capacitor performance: an areal specific capacitance of 64 $\mu F/cm^2$ and a cyclic stability of 98% retention after 5,000 charge-discharge cycles. Nitrogen-doped porous graphitic carbon nanofibers derived from plant protein have the potential to be used as capacitors in industrial applications and household electronic products. The synthesis strategy developed in this study opens up a novel, effective and green approach to prepare functional carbon capacitor materials from a protein based biomass.

Chapter 6

Final Remarks

6.1 Summary and conclusions

Barley is the fourth most important crop around the world and contains 8-15% protein in the dried grain. However, the utilization of barley is limited to feed and malt industries. Studies on barley protein applications are far from sufficient. In this PhD research program, the interfacial behaviour of barley proteins was systematically investigated (*Objective 1, Chapter 2*). Grounded on the generated knowledge, barley protein based nanoparticles were successfully developed (*Objective 2, Chapter 3*). To further explore value-added application opportunities, barley protein based electrospun fibers were converted to carbon fiber network as energy storage materials for the first time (*Objectives 3&4, Chapters 4&5*). This section highlights the findings and conclusions made in each study.

6.1.1 Conclusions of study 1

Interfacial property is one of the most important functionalities of food proteins. Though the foaming, emulsifying and encapsulating capabilities of barley proteins were presented in some previous studies, interfacial properties of barley proteins were not clear yet. Thus, study 1 investigated the behaviour of barley proteins at the interface. B-hordein was selected to be a representative of barley proteins in this fundamental work since hordein was the largest component of barley proteins and B-hordein was the major fraction of hordein. The results

revealed that B-hordein adsorbed to the air-water interface rapidly and 1 mg/mL B-hordein solution was able to reduce the surface tension to ~45 mN/m within 2 h. As shown by the interfacial dilatation and shear rheology, B-hordein molecules formed a solid-like film at the interface. With longer aging time, the B-hordein interfacial network became stiffer and more elastic. The result obtained from Longmuir-Blodgett trough revealed that B-hordein molecules changed from expanded liquid to solid-like phase without collapse when the surface pressure was increased to 30 mN/s, which was interesting as compared to many other hydrophilic food proteins reported in the literature. Also, polarization modulation-infrared reflection absorption spectroscopy (PM-IRRAS) showed that B-hordein molecules tilted their hydrophobic repetitive region away from the aqueous phase toward air phase upon continuous compression. The intermolecular β-sheets developed upon compression might contribute to the formation of the highly elastic B-hordein film at the interface. Finally, the *in situ* pepsin digestion test showed that the B-hordein film formed at 30 mN/s was resistant to gastric environment degradation, which might be attributed to the hydrophobic region being hidden from the aqueous phase through protein conformation and orientation changes as mentioned above. Overall, the fundamental knowledge of study 1 demonstrated that B-hordein had excellent interfacial properties and had potential to be used to stabilize emulsions and encapsulations with controllable gastric digestibility. Thus, barley proteins can be utilized in many applications such as small intestine targeted delivery system of bioactive compounds.

6.1.2 Conclusions of study 2

Based on the interfacial properties of B-hordein and its resistance to the gastric environment, barley protein based nanoparticles were successfully developed at ambient temperature without the addition of organic solvent and surfactant in study 2 as a delivery system for lipophilic bioactive compounds. Canola oil with 0.05% (w/v) β-carotene was used as the lipid phase to be encapsulated in the coating of barley proteins. The lipid phase was mixed with aqueous protein suspension to prepare a coarse emulsion, followed by passing it through high pressure homogenization to form solid nanoparticles. The optimized nanoparticles had regular spherical shape, smooth surface, small size of 90-150 nm, narrow size distribution (PDI<0.3) and high zeta-potential of -35 mV. The influences of processing pressure, number of recirculation and formulation on particle size and size distribution were investigated. With increasing circulation times and pressure, particle size decreased and size distribution became narrow. Increasing the pressure above 16,000 psi, particle size increased significantly due to 'over-processing' phenomenon. When oil-to-protein ratio was increased, mean particle size increased. Stable nanoparticle suspension could be obtained at a protein concentration of up to 5% when the oil-to-protein ratio was maintained within 1 to 1.5. Release test showed that the bulk protein coating was degraded in SGF, but a thin layer of barley protein covering the oil-droplet surface was resistant to pepsin digestion. Complete release of the oil phase occurred in SIF. *In vitro* test

exhibited that barley protein based nanoparticles had low cytotoxicity and could be internalized by Caco-2 cells.

6.1.3 Conclusions of study 3

Electrospinnability is another important functionality of hordein. In study 3, hordein/zein based electrospun nanofibers were prepared in the presence of lignin, which were then converted into carbon fibers by carbonization and CO_2 activation. The influences of protein-lignin ratio and carbonization temperature on the morphology of carbon products were investigated. The optimal carbon sample (L5P5-900-ACT) with hierarchical pores and interconnected carbon fiber network was prepared with protein-lignin ratio of 50:50 at 900 °C, followed by CO_2 activation at 800°C for 3 h. Nitrogen adsorption-desorption isotherm showed that the specific surface area of L5P5-900-ACT was 771.5 m^2/g. Macro, meso and micropores coexisted on the fiber. The interconnected large macropores formed by interlaced fiber as well as the macro and mesopores on the fiber surface facilitated the transport of electrolyte ions. The meso and micropores endowed fibers high specific surface area and high capacitance. L5P5-900-ACT had 4% nitrogen atoms, which are mainly pyridinic and pyrrolic nitrogen. Nitrogen functional groups can enhance carbon fiber capacitance through faradaic reactions. TEM, XRD pattern and Raman spectrum confirmed the existence of graphene-like nanosheet structure on the L5P5-900-ACT carbon fiber. Electrochemical tests demonstrated that L5P5-900-ACT had excellent capacitance of 240 F/g and 31.2 $\mu F/cm^2$ in 6 M KOH at 0.25 A/g. L5P5-900-ACT also showed good conductivity and

high cyclic stability with 95% retention after 5,500 charge-discharge cycle. L5P5-900-ACT had potential to be used as electrode material for supercapacitors.

6.1.4 Conclusions of study 4

In study 4, a facile and green one-step pyrolysis method was developed to prepare nitrogen-doped porous graphitic carbon nanofibers from plant protein (hordein and zein) electrospun fabrics. Calcium acetate was added to the electrospinning dope to modulate the diameter of electrospun fibers. When Ca^{2+} was increased from 4 to 10%, the fiber diameter decreased from 992 to 413 nm. The carbon sample prepared with 18% protein and 10% Ca^{2+} exhibited a homogeneous, smooth and flexible fiber structure. The optimized sample P-10%Ca-CL had 6.4% of nitrogen, which was higher than the nitrogen content of carbon materials made from other biomass reported in the literature. Well aligned stacking graphitic nanosheet structure and onion-like carbon structure were observed in the P-10%Ca-CL carbon sample. This is the first time that such highly ordered granule-like graphitic structure was found within carbon fibers derived from biomaterials. Due to these morphological and chemical features, the carbon fiber sample demonstrated ultrahigh areal specific capacitance of 64 $\mu F/cm^2$ and excellent cyclic stability of 98% retention after 5,000 charge-discharge cycles. The approach developed in this study provided a convenient and environmentally friendly way to prepare porous graphitic carbon fibers from renewable biomaterials.

6.2 Significance of this work

There is a growing market demand on products made from biomaterials which are renewable, biocompatible and biodegradable. Based on the large production of barley, barley proteins are abundant and affordable biomaterials. However, the value of barley proteins has been underestimated and their utilization is still not fully explored, which might be due to the insufficient fundamental knowledge available on barley protein.

This PhD research is the first to investigate the interfacial properties of barley proteins systematically at molecular level. By employing B-hordein as a model protein, this study demonstrated how conformation and orientation changes of protein molecules at the interface upon compression influenced the digestibility of the protein network. Fundamental knowledge gained from this study helps the rational design of barley protein based functional food and delivery systems for bioactive compounds. Grounded on this, barley protein based nanoparticles were successfully prepared through high pressure homogenization as delivery systems to improve the bioavailability of lipophilic nutraceuticals, which significantly extended the applications of barley protein to food and pharmaceutical area. Also, this finding deepened our understanding on protein-based emulsion digestion, guiding us towards improved control of dietary intake.

Moreover, this work is the first to report that protein based electrospun fibers can be successfully converted into carbon nanofibers. Carbon fibers either derived from protein-lignin or

protein-Ca^{2+} fibers showed excellent capacitance and cyclic stability, which made them promising to be used as electrode materials. These findings opened up new applications of barley proteins in high technology area, such as energy storage systems and power management. It is also a part of the research effort to develop electrical devices from renewable and green biomaterials.

Overall, results obtained in this work provide brand new applications of barley proteins, which can broaden the application of barley and commercially benefit the Canadian barley producers and processors.

6.3 Recommendations for future work

This PhD research brings up some interesting ideas which may be valuable for future studies. Here, a few possible points are listed.

(1) This study systematically investigated the interfacial properties of barley proteins at model air-water interface. It is also necessary to confirm these finding at an oil-water interface. The *in situ* digestion test was conducted in a simulated gastric environment. The influences of intestinal conditions, such as bile salts, pH and enzymes, on the protein interfacial network are still not clear yet. This gap should be filled in the near future to direct us for rational design of protein-based emulsion with desired digestibility.

(2) Barley protein based nanoparticles have been successfully prepared in this work at lab scale. The potential of using barley protein nanoparticles as delivery system has been preliminarily

proven. However, pilot scale experiments are needed to optimize the processing conditions before barley protein nanoparticles can be used at industrial scale. Also, barley protein nanoparticles showed good storage stability in this study. It is interesting to test the compatibility of barley protein nanoparticles with various real food systems, such as milk, juice, snacks *etc*. Also, the influence of the addition of barley protein nanoparticles on the food sensory properties are necessary to be explored. Sequential *in vivo* tests are needed to evaluate the bioavailability of the encapsulated nutraceuticals and confirm the safety of the barley protein nanoparticles.

（3）Carbon fibers derived from plant proteins (hordein and zein) were observed to have highly ordered graphene-like nanosheet or granule-like graphitic structure. This finding is very valuable since graphene endows carbon materials some useful features, such as good electrical conductivity. This graphitic structure was formed at a relatively low temperature (<1000°C) without catalysis. This may be related to the secondary structures of protein. However, the detailed mechanism is far from clear.

(4) It was exciting to find that Ca^{2+} can facilitate the conversion of protein fibers to carbon fibers. More efforts are needed to fabricate this flexible carbon fiber mat into novel devices, such as supercapacitor, sensors, electronic devices, artificial scaffolds and smart textiles.

References

1. Mohamed, A.; Hojilla-Evangelista, M. P.; Peterson, S. C.; Biresaw, G. Barley protein isolate: Thermal, functional, rheological, and surface properties. *J. Am. Oil Chem. Soc.* 2007, 84, 281-288.

2. Jadhav, S. J.; Lutz, S. E.; Ghorpade, V. M.; Salunkhe, D. K. Barley: Chemistry and value-added processing. *Crit. Rev. Food Sci. Nutr.* 1998, 38, 123-171.

3. Izydorczyk, M. S.; Dexter, J. E. Barley beta-glucans and arabinoxylans: Molecular structure, physicochemical properties, and uses in food products-a review. *Food Res. Int.* 2008, 41, 850-868.

4. Wood, P. J. Cereal beta-glucans in diet and health. *J. Cereal Sci.* 2007, 46, 230-238.

5. Finnie, C.; Svensson, B. Barley seed proteomics from spots to structures. *J. Proteomics* 2009, 72, 315-324.

6. Fukushima, D. Structures of plant storage proteins and their functions. *Food Rev. Int.* 1991, 7, 353-381.

7. Celus, I.; Brijs, K.; Delcour, J. A. The effects of malting and mashing on barley protein extractability. *J. Cereal Sci.* 2006, 44, 203-211.

8. Anderson, O. D.; Scoles, G. J. The B-hordein prolamin family of barley. *Genome* 2013, 56, 179-185.

9. Linko, R.; Lapveteläinen, A.; Laakso, P.; Kallio, H. Protein composition of a high-protein barley flour and barley grain. *Cereal Chem.* 1989, 66, 478-482.

10. Lange, M.; Vincze, E.; Wieser, H.; Schjoerring, J. K.; Holm, P. B. Suppression of C-hordein synthesis in barley by antisense constructs results in a more balanced amino acid composition. *J. Agric. Food Chem.* 2007, 55, 6074-6081.

11. Williamson, M. P. The structure and function of proline-rich regions in proteins. *Biochem. J.* 1994, 297, 249.

12. Burley, S. K.; Petsko, G. A. Aromatic-aromatic interaction: a mechanism of protein structure stabilization. *Science* 1985, 229, 23-28.

13. Tatham, A. S.; Drake, A. F.; Shewry, P. R. A conformational study of a glutamine-and proline-rich cereal seed protein, C hordein. *Biochem. J.* 1985, 226, 557.

14. Tatham, A. S.; Shewry, P. R. The S-poor prolamins of wheat, barley and rye: Revisited. *J. Cereal Sci.* 2012, 55, 79-99.

15. Field, J. M.; Tatham, A. S.; Baker, A. M.; Shewry, P. R. The structure of C hordein. *FEBS Lett.* 1986, 200, 76-80.

16. Baik, B. K.; Ullrich, S. E. Barley for food: Characteristics, improvement, and renewed interest. *J. Cereal Sci.* 2008, 48, 233-242.

17. Wilde, P.; Mackie, A.; Husband, F.; Gunning, P.; Morris, V. Proteins and emulsifiers at liquid interfaces. *Adv. Colloid Interface Sci.* 2004, 108, 63-71.

18. Wang, C.; Tian, Z.; Chen, L.; Temelli, F.; Liu, H.; Wang, Y. Functionality of barley proteins extracted and fractionated by alkaline and alcohol methods. *Cereal Chem.* 2010, 87, 597-606.

19. Bilgi, B.; celik, S. Solubility and emulsifying properties of barley protein concentrate. *Eur. Food Res. Technol.* 2004, 218, 437-441.

20. Zhao, J.; Tian, Z.; Chen, L. Effects of deamidation on aggregation and emulsifying properties of barley glutelin. *Food Chem.* 2011, 128, 1029-1036.

21. Zhao, J.; Tian, Z.; Chen, L. Effects of deamidation on structure and functional properties of barley hordein. *J. Agric. Food Chem.* 2010, 58, 11448-11455.

22. Kapp, G. R.; Bamforth, C. W. The foaming properties of proteins isolated from barley. *J. Sci. Food Agric.* 2002, 82, 1276-1281.

23. Xia, Y.; Wang, Y.; Chen, L. Molecular structure, physicochemical characterization, and *in vitro* degradation of barley protein films. *J. Agric. Food Chem.* 2011, 59, 13221-13229.

24. Gibbs, F. B.; Kermasha, S.; Alli, I.; Mulligan, C. N. Encapsulation in the food industry: a review. *Int. J. Food Sci. Nutr.* 1999, 50, 213-224.

25. Chen, L.; Remondetto, G. E.; Subirade, M. Food protein-based materials as nutraceutical delivery systems. *Trends Food Sci. Technol.* 2006, 17, 272-283.

26. Wang, R.; Tian, Z.; Chen, L. A novel process for microencapsulation of fish oil with barley protein. *Food Res. Int.* 2011, 44, 2735-2741.

27. Wang, R. X.; Tian, Z. G.; Chen, L. Y. Nano-encapsulations liberated from barley protein microparticles for oral delivery of bioactive compounds. *Int. J. Pharm.* 2011, 406, 153-162.

28. Wang, Y. X.; Chen, L. Y. Fabrication and characterization of novel assembled prolamin protein nanofabrics with improved stability, mechanical property and release profiles. *J. Mater. Chem.* 2012, 22, 21592-21601.

29. Wang, Y.; Chen, L. Cellulose nanowhiskers and fiber alignment greatly improve mechanical properties of electrospun prolamin protein fibers. *ACS Appl. Mater. Interfaces* 2014, 6, 1709-1718.

30. Wang, Y.; Yang, J.; Chen, L. Convenient fabrication of electrospun prolamin protein delivery system with three-dimensional shapeability and resistance to fouling. *ACS Appl. Mater. Interfaces* 2015, 7, 13422-13430.

31. Li, D.; Xia, Y. Electrospinning of nanofibers: reinventing the wheel? *Adv. Mater.* 2004, 16, 1151-1170.

32. Bos, M. A.; van Vliet, T. Interfacial rheological properties of adsorbed protein layers and surfactants: a review. *Adv. Colloid Interface Sci.* 2001, 91, 437-471.

33. Dalgleish, D. G. Adsorption of protein and the stability of emulsions. *Trends Food Sci. Technol.* 1997, 8, 1-6.

34. Mitropoulos, V.; Mütze, A.; Fischer, P. Mechanical properties of protein adsorption layers at the air/water and oil/water interface: A comparison in light of the thermodynamical stability of proteins. *Adv. Colloid Interface Sci.* 2014, 206, 195-206.

35. Wang, R.; Tian, Z.; Chen, L. A novel process for microencapsulation of fish oil with barley protein. *Food Res. Int.* 2011, 44, 2735-2741.

36. MacRitchie, F. Protein adsorption/desorption at fluid interfaces. *Colloids and Surf.* 1989, 41, 25-34.

37. Haynes, C. A.; Norde, W. Globular proteins at solid/liquid interfaces. *Colloids Surf., B* 1994, 2, 517-566.

38. Fowkes, F. M. Additivity of intermolecular forces at interfaces. i. determination of the contribution to surface and interfacial tensions of dispersion forces in various liquids1. *J Phys Chem* 1963, 67, 2538-2541.

39. Eastoe, J.; Dalton, J. S. Dynamic surface tension and adsorption mechanisms of surfactants at the air-water interface. *Adv. Colloid Interface Sci.* 2000, 85, 103-144.

40. Absolom, D. R.; Van Oss, C. J.; Zingg, W.; Neumann, A. W. Determination of surface tensions of proteins II. surface tension of serum albumin, altered at the protein-air interface. *Biochim. Biophys. Acta, Protein Struct.* 1981, 670, 74-78.

41. Srisankar, E. V.; Shah, J. P.; Narayan, K. S. A simple apparatus for measuring dynamic surface tension. *J. Chem. Educ.* 1987, 64, 378.

42. Chen, P.; Prokop, R. M.; Susnar, S. S.; Neumann, A. W. Interfacial tensions or protein solutions using axisymmetric drop shape analysis. In *Proteins at liquid interfaces; D. Möbius, R. Miller, Eds.; Elseview: Philadelphia,* 1998; pp 303-309.

43. Beverung, C. J.; Radke, C. J.; Blanch, H. W. Protein adsorption at the oil/water interface: characterization of adsorption kinetics by dynamic interfacial tension measurements. *Biophys. Chem.* 1999, 81, 59-80.

44. Tripp, B. C.; Magda, J. J.; Andrade, J. D. Adsorption of globular proteins at the air/water interface as measured via dynamic surface tension: concentration dependence, mass-transfer considerations, and adsorption kinetics. *J. Colloid and Interface Sci.*1995, 173, 16-27.

45. Langevin, D. Influence of interfacial rheology on foam and emulsion properties. *Adv. Colloid Interface Sci.* 2000, 88, 209-222.

46. Fainerman, V. B.; Miller, R. Equilibrium and dynamic characteristics of protein adsorption layers at gas-liquid interfaces: theoretical and experimental data. *Colloid J.* 2005, 67, 393-404.

47. Di Lollo, A. B. Thermal and surface properties of crystalline and non-crystallinen legume seed proteins (Doctoral dissertation). *Macdonald College of McGill University* Canada 1990. Retrieved from http://digitool.library.mcgill.ca/.

48. Suttiprasit, P.; Krisdhasima, V.; McGuire, J. The surface activity of α-lactalbumin, β-lactoglobulin, and bovine serum albumin: I. Surface tension measurements with single-component and mixed solutions. *J. Colloid and Interface Sci.* 1992, 154, 316-326.

49. Damodaran, S. Water activity at interfaces and its role in regulation of interfacial enzymes: a hypothesis. *Colloids Surf., B* 1998, 11, 231-237.

50. Franses, E. I.; Basaran, O. A.; Chang, C. H. Techniques to measure dynamic surface tension. *Curr. Opin. Colloid Interface Sci.* 1996, 1, 296-303.

51. Murray, B. S. Interfacial rheology of food emulsifiers and proteins. *Curr. Opin. Colloid Interface Sci.* 2002, 7, 426-431.

52. Freer, E. M.; Yim, K. S.; Fuller, G. G.; Radke, C. J. Shear and dilatational relaxation mechanisms of globular and flexible proteins at the hexadecane/water interface. *Langmuir* 2004, 20, 10159-10167.

53. Baldursdottir, S. G.; Fullerton, M. S.; Nielsen, S. H.; Jorgensen, L. Adsorption of proteins at the oil/water interface - observation of protein adsorption by interfacial shear stress measurements. *Colloids Surf., B* 2010, 79, 41-46.

54. Freer, E. M.; Yim, K. S.; Fuller, G. G.; Radke, C. J. Interfacial rheology of globular and flexible proteins at the hexadecane/water interface: Comparison of shear and dilatation deformation. *J. Phys. Chem. B* 2004, 108, 3835-3844.

55. Cascão Pereira, L. G.; Théodoly, O.; Blanch, H. W.; Radke, C. J. Dilatational rheology of BSA conformers at the air/water interface. *Langmuir* 2003, 19, 2349-2356.

56. Kim, D. A.; Cornec, M.; Narsimhan, G. Effect of thermal treatment on interfacial properties of beta-lactoglobulin. *J. Colloid and Interface Sci.* 2005, 285, 100-109.

57. Maldonado-Valderrama, J.; Gunning, A. P.; Ridout, M. J.; Wilde, P. J.; Morris, V. J. The effect of physiological conditions on the surface structure of proteins: Setting the scene for human digestion of emulsions. *Eur. Phys. J. E: Soft Matter Biol. Phys.* 2009, 30, 165-174.

58. Maldonado-Valderrama, J.; Gunning, A. P.; Wilde, P. J.; Morris, V. J. *In vitro* gastric digestion of interfacial protein structures: Visualisation by AFM. *Soft Matter* 2010, 6, 4908-4915.

59. Maldonado-Valderrama, J.; Miller, R.; Fainerman, V. B.; Wilde, P. J.; Morris, V. J. Effect of gastric conditions on beta-lactoglobulin interfacial networks: Influence of the oil phase on protein structure. *Langmuir* 2010, 26, 15901-15908.

60. Murray, B. S. Rheological properties of protein films. *Curr. Opin. Colloid Interface Sci.* 2011, 16, 27-35.

61. Reis, P.; Watzke, H.; Leser, M.; Holmberg, K.; Miller, R. Interfacial mechanism of lipolysis as self-regulated process. *Biophys Chem.* 2010, 147, 93-103.

62. Maldonado-Valderrama, J.; Woodward, N. C.; Gunning, A. P.; Ridout, M. J.; Husband, F. A.; Mackie, A. R.; Morris, V. J.; Wilde, P. J. Interfacial characterization of beta-lactoglobulin networks: Displacement by bile salts. *Langmuir* 2008, 24, 6759-6767.

63. Lefèvre, T.; Subirade, M. Molecular structure and interaction of biopolymers as viewed by Fourier transform infrared spectroscopy: model studies on β-lactoglobulin. *Food Hydrocoll.* 2001, 15, 365-376.

64. McClements, D. J. Protein-stabilized emulsions. *Curr. Opin. Colloid Interface Sci.* 2004, 9, 305-313.

65. Graham, D. E.; Phillips, M. C. Proteins at liquid interfaces: I. Kinetics of adsorption and surface denaturation. *J. Colloid and Interface Sci.* 1979, 70, 403-414.

66. Mezzenga, R.; Fischer, P. The self-assembly, aggregation and phase transitions of food protein systems in one, two and three dimensions. *Rep. Prog. Phys.* 2013, 76, 046601.

67. Anderson, R. E.; Pande, V. S.; Radke, C. J. Dynamic lattice Monte Carlo simulation of a model protein at an oil/water interface. *J. Chem. Phys.* 2000, 112, 9167-9185.

68. Lefevre, T.; Subirade, M. Formation of intermolecular beta-sheet structures: a phenomenon relevant to protein film structure at oil-water interfaces of emulsions. *J. Colloid and Interface Sci.* 2003, 263, 59-67.

69. Kong, J.; Yu, S. Fourier transform infrared spectroscopic analysis of protein secondary structures. *Acta Biochim. Biophys. Sin.* 2007, 39, 549-559.

70. Bandekar, J. Amide modes and protein conformation. *Biochim. Biophys. Acta, Protein Struct. Mol. Enzymol.* 1992, 1120, 123-143.

71. Lefevre, T.; Subirade, M. Structural and interaction properties of beta-lactoglobulin as studied by FTIR spectroscopy. *Int. J. Food Sci. Technol.* 1999, 34, 419-428.

72. Meinders, M. B. J.; van den Bosch, G. G. M.; de Jongh, H. H. J. IRRAS, a new tool in food science. *Trends Food Sci. Technol.* 2000, 11, 218-225.

73. Gallant, J.; Desbat, B.; Vaknin, D.; Salesse, C. Polarization-modulated infrared spectroscopy and X-ray reflectivity of photosystem II core complex at the gas-water interface. *Biophys J.* 1998, 75, 2888-2899.

74. Desroches, M. J.; Chaudhary, N.; Omanovic, S. PM-IRRAS investigation of the interaction of serum albumin and fibrinogen with a biomedical-grade stainless steel 316LVM surface. *Biomacromolecules* 2007, 8, 2836-2844.

75. Boncheva, M.; Vogel, H. Formation of stable polypeptide monolayers at interfaces: controlling molecular conformation and orientation. *Biophys J.* 1997, 73, 1056-1072.

76. Fang, Y.; Dalgleish, D. G. Conformation of beta-lactoglobulin studied by FTIR: effect of pH, temperature, and adsorption to the oil in water interface. *J. Colloid and Interface Sci.* 1997, 196, 292-298.

77. Banc, A.; Desbat, B.; Renard, D.; Popineau, Y.; Mangavel, C.; Navailles, L. Structure and orientation changes of omega- and gama-gliadins at the air-water interface: a PM-IRRAS spectroscopy and Brewster angle microscopy study. *Langmuir* 2007, 23, 13066-13075.

78. Thakur, G.; Leblanc, R. M. Conformation of lysozyme Langmuir monolayer studied by infrared reflection absorption spectroscopy. *Langmuir* 2009, 25, 2842-2849.

79. Doshi, J.; Reneker, D. H. In *Electrospinning process and applications of electrospun fibers*, Industry Applications Society Annual Meeting, 1993., Conference Record of the 1993 IEEE, IEEE: 1993; pp 1698-1703.

80. Huang, Z. M.; Zhang, Y. Z.; Kotaki, M.; Ramakrishna, S. A review on polymer nanofibers by electrospinning and their applications in nanocomposites. *Compos. Sci. Technol.* 2003, 63, 2223-2253.

81. Bhardwaj, N.; Kundu, S. C. Electrospinning: a fascinating fiber fabrication technique. *Biotechnol. Adv.* 2010, 28, 325-347.

82. Sill, T. J.; von Recum, H. A. Electrospinning: applications in drug delivery and tissue engineering. *Biomaterials* 2008, 29, 1989-2006.

83. Schiffman, J. D.; Schauer, C. L. A review: electrospinning of biopolymer nanofibers and their applications. *Polym. Rev.* 2008, 48, 317-352.

84. Frenot, A.; Chronakis, I. S. Polymer nanofibers assembled by electrospinning. *Curr. Opin. Colloid Interface Sci.* 2003, 8, 64-75.

85. Ko, F. K. Nanofiber technology: Bridging the gap between nano and macro world. In *Nanoengineered Nanofibrous Materials;* Selcuk Guceri, Yuri G. Gogotsi, and Vladimir Kuznetsov, Eds.; Kluwer Academic Publishers: Dordrecht, 2004; pp: 1-18.

86. Fong, H.; Chun, I.; Reneker, D. H. Beaded nanofibers formed during electrospinning. *Polymer* 1999, 40, 4585-4592.

87. Liu, H.; Hsieh, Y. L. Ultrafine fibrous cellulose membranes from electrospinning of cellulose acetate. *J. Polym. Sci., Part B: Polym. Phys.* 2002, 40, 2119-2129.

88. Deitzel, J. M.; Kleinmeyer, J.; Harris, D.; Tan, N. The effect of processing variables on the morphology of electrospun nanofibers and textiles. *Polymer* 2001, 42, 261-272.

89. Kongkhlang, T.; Kotaki, M.; Kousaka, Y.; Umemura, T.; Nakaya, D.; Chirachanchai, S. Electrospun polyoxymethylene: Spinning conditions and its consequent nanoporous nanofiber. *Macromolecules* 2008, 41, 4746-4752.

90. Son, W. K.; Youk, J. H.; Lee, T. S.; Park, W. H. The effects of solution properties and polyelectrolyte on electrospinning of ultrafine poly (ethylene oxide) fibers. *Polymer* 2004, 45, 2959-2966.

91. Scheibel, T. Protein fibers as performance proteins: new technologies and applications. *Curr. Opin. Biotechnol.* 2005, 16, 427-433.

92. Jiang, Q.; Reddy, N.; Yang, Y. Cytocompatible cross-linking of electrospun zein fibers for the development of water-stable tissue engineering scaffolds. *Acta Biomater.* 2010, 6, 4042-4051.

93. Wang, Y.; Chen, L. Electrospinning of prolamin proteins in acetic acid: the effects of protein conformation and aggregation in solution. *Macromol. Mater. Eng.* 2012, 297, 902-913.

94. Tatham, A. S.; Shewry, P. R. Elastomeric proteins: biological roles, structures and mechanisms. *Trends Biochem. Sci.* 2000, 25, 567-571.

95. Wang, Y.; Chen, L. Impacts of nanowhisker on formation kinetics and properties of all-cellulose composite gels. *Carbohydr. Polym.* 2011, 83, 1937-1946.

96. Dong, Z.; Kennedy, S. J.; Wu, Y. Electrospinning materials for energy-related applications and devices. *J. Power Sources* 2011, 196, 4886-4904.

97. Lallave, M.; Bedia, J.; Ruiz-Rosas, R.; Rodríguez-Mirasol, J.; Cordero, T.; Otero, J. C.; Marquez, M.; Barrero, A.; Loscertales, I. Filled and hollow carbon nanofibers by coaxial electrospinning of alcell lignin without binder polymers. *Adv. Mater.* 2007, 19, 4292-4296.

98. Deng, L.; Young, R. J.; Kinloch, I. A.; Abdelkader, A. M.; Holmes, S. M.; De Haro-Del Rio, D. A.; Eichhorn, S. J. Supercapacitance from cellulose and carbon nanotube nanocomposite fibers. *ACS Appl. Mater. Interfaces* 2013, 5, 9983-9990.

99. Kötz, R.; Carlen, M. Principles and applications of electrochemical capacitors. *Electrochim. Acta* 2000, 45, 2483-2498.

100. Pandolfo, A. G.; Hollenkamp, A. F. Carbon properties and their role in supercapacitors. *J. Power Sources* 2006, 157, 11-27.

101. Frackowiak, E.; Beguin, F. Carbon materials for the electrochemical storage of energy in capacitors. *Carbon* 2001, 39, 937-950.

102. Wang, G.; Zhang, L.; Zhang, J. A review of electrode materials for electrochemical supercapacitors. *Chem. Soc. Rev.* 2012, 41, 797-828.

103. Chuang, C. M.; Huang, C. W.; Teng, H.; Ting, J. M. Effects of carbon nanotube grafting on the performance of electric double layer capacitors. *Energy Fuels* 2010, 24, 6476-6482.

104. Béguin, F.; Presser, V.; Balducci, A.; Frackowiak, E. Carbons and electrolytes for advanced supercapacitors. *Adv. Mater.* 2014, 26, 2219-2251.

105. Frackowiak, E. Carbon materials for supercapacitor application. *Phys. Chem. Chem. Phys.* 2007, 9, 1774-1785.

106. Naoi, K.; Simon, P. New materials and new configurations for advanced electrochemical capacitors. *J. Electrochem. Soc.* 2008, 17, 34-37.

107. Ryu, K. S.; Kim, K. M.; Park, N. G.; Park, Y. J.; Chang, S. H. Symmetric redox supercapacitor with conducting polyaniline electrodes. *J. Power Sources* 2002, 103, 305-309.

108. Fan, L. Z.; Maier, J. High-performance polypyrrole electrode materials for redox supercapacitors. *Electrochem. Commun.* 2006, 8, 937-940.

109. Xu, Y.; Wang, J.; Sun, W.; Wang, S. Capacitance properties of poly (3, 4-ethylenedioxythiophene)/polypyrrole composites. *J. Power Sources* 2006, 159, 370-373.

110. Sharma, P.; Bhatti, T. S. A review on electrochemical double-layer capacitors. *Energy Convers. Manage.* 2010, 51, 2901-2912.

111. Gupta, V.; Miura, N. High performance electrochemical supercapacitor from electrochemically synthesized nanostructured polyaniline. *Mater. Lett.* 2006, 60, 1466-1469.

112. Wu, Q.; Xu, Y.; Yao, Z.; Liu, A.; Shi, G. Supercapacitors based on flexible graphene/polyaniline nanofiber composite films. *ACS nano* 2010, 4, 1963-1970.

113. Simon, P.; Gogotsi, Y. Materials for electrochemical capacitors. *Nat. Mater.* 2008, 7, 845-854.

114. Gamby, J.; Taberna, P. L.; Simon, P.; Fauvarque, J. F.; Chesneau, M. Studies and characterisations of various activated carbons used for carbon/carbon supercapacitors. *J. Power Sources* 2001, 101, 109-116.

115. Li, Z.; Xu, Z.; Tan, X.; Wang, H.; Holt, C. M. B.; Stephenson, T.; Olsen, B. C.; Mitlin, D. Mesoporous nitrogen-rich carbons derived from protein for ultra-high capacity battery anodes and supercapacitors. *Energy Environ. Sci.* 2013, 6, 871-878.

116. Avraham, E.; Yaniv, B.; Soffer, A.; Aurbach, D. Developing ion electroadsorption stereoselectivity, by pore size adjustment with chemical vapor deposition onto active carbon fiber electrodes. Case of Ca^{2+}/Na^{+} separation in water capacitive desalination. *J. Phys. Chem. C* 2008, 112, 7385-7389.

117. Dutta, S.; Bhaumik, A.; Wu, K. C. W. Hierarchically porous carbon derived from polymers and biomass: effect of interconnected pores on energy applications. *Energy Environ. Sci.* 2014, 7, 3574-3592.

118. Chen, L. F.; Huang, Z. H.; Liang, H. W.; Guan, Q. F.; Yu, S. H. Bacterial-cellulose derived carbon nanofiber@MnO2 and nitrogen-doped carbon nanofiber electrode materials: an asymmetric supercapacitor with high energy and power density. *Adv. Mater.* 2013, 25, 4746-4752.

119. Hao, L.; Li, X.; Zhi, L. Carbonaceous electrode materials for supercapacitors. *Adv. Mater.* 2013, 25, 3899-3904.

120. Hulicova-Jurcakova, D.; Seredych, M.; Lu, G. Q.; Bandosz, T. J. Combined effect of nitrogen□and oxygen□containing functional groups of microporous activated carbon on its electrochemical performance in supercapacitors. *Adv. Funct. Mater.* 2009, 19, 438-447.

121. Lota, G.; Grzyb, B.; Machnikowska, H.; Machnikowski, J.; Frackowiak, E. Effect of nitrogen in carbon electrode on the supercapacitor performance. *Chem. Phys. Lett.* 2005, 404, 53-58.

122. Qian, W.; Sun, F.; Xu, Y.; Qiu, L.; Liu, C.; Wang, S.; Yan, F. Human hair-derived carbon flakes for electrochemical supercapacitors. *Energy Environ. Sci.* 2014, 7, 379-386.

123. Chen, L. F.; Zhang, X. D.; Liang, H. W.; Kong, M.; Guan, Q. F.; Chen, P.; Wu, Z. Y.; Yu, S. H. Synthesis of nitrogen-doped porous carbon nanofibers as an efficient electrode material for supercapacitors. *ACS nano* 2012, 6, 7092-7102.

124. Chen, L. F.; Huang, Z. H.; Liang, H. W.; Yao, W. T.; Yu, Z. Y.; Yu, S. H. Flexible all-solid-state high-power supercapacitor fabricated with nitrogen-doped carbon nanofiber electrode material derived from bacterial cellulose. *Energy Environ. Sci.* 2013, 6, 3331-3338.

125. Jeong, H. M.; Lee, J. W.; Shin, W. H.; Choi, Y. J.; Shin, H. J.; Kang, J. K.; Choi, J. W. Nitrogen-doped graphene for high-performance ultracapacitors and the importance of nitrogen-doped sites at basal planes. *Nano Lett.* 2011, 11, 2472-2477.

126. Jurewicz, K.; Babeł, K.; Źiółkowski, A.; Wachowska, H. Ammoxidation of active carbons for improvement of supercapacitor characteristics. *Electrochim. Acta* 2003, 48, 1491-1498.

127. Kalyani, P.; Anitha, A. Biomass carbon & its prospects in electrochemical energy systems. *Int. J. Hydrogen Energy* 2013, 38, 4034-4045.

128. Wu, X. L.; Wen, T.; Guo, H. L.; Yang, S.; Wang, X.; Xu, A. W. Biomass-derived sponge-like carbonaceous hydrogels and aerogels for supercapacitors. *ACS nano* 2013, 7, 3589-3597.

129. Wang, S.-X.; Yang, L.; Stubbs, L. P.; Li, X.; He, C. Lignin-derived fused electrospun carbon fibrous mats as high performance anode materials for lithium ion batteries. *ACS Appl. Mater. Interfaces* 2013, 5, 12275-12282.

130. Zhu, B.; Deng, Z.; Yang, W.; Wang, H.; Gao, L. Pyrolyzed polyaniline and graphene nano sheet composite with improved rate and cycle performance for lithium storage. *Carbon* 2015, 92, 354-361.

131. Lai, C.; Zhou, Z.; Zhang, L.; Wang, X.; Zhou, Q.; Zhao, Y.; Wang, Y.; Wu, X. F.; Zhu, Z.; Fong, H. Free-standing and mechanically flexible mats consisting of electrospun carbon

nanofibers made from a natural product of alkali lignin as binder-free electrodes for high-performance supercapacitors. *J. Power Sources* 2014, 247, 134-141.

132. Fitzer, E.; Kochling, K. H.; Boehm, H. P.; Marsh, H. Recommended terminology for the description of carbon as a solid (IUPAC Recommendations 1995). *Pure Appl. Chem.* 1995, 67, 473-506.

133. Zhai, D.; Du, H.; Li, B.; Zhu, Y.; Kang, F. Porous graphitic carbons prepared by combining chemical activation with catalytic graphitization. *Carbon* 2011, 49, 725-729.

134. Huang, C. H.; Zhang, Q.; Chou, T. C.; Chen, C. M.; Su, D. S.; Doong, R. A. Three-dimensional hierarchically ordered porous carbons with partially graphitic nanostructures for electrochemical capacitive energy storage. *ChemSusChem* 2012, 5, 563-571.

135. Wang, H.; Li, Z.; Mitlin, D. Tailoring biomass-derived carbon nanoarchitectures for high-performance supercapacitors. *ChemElectroChem* 2014, 1, 332-337.

136. Biswal, M.; Banerjee, A.; Deo, M.; Ogale, S. From dead leaves to high energy density supercapacitors. *Energy Environ. Sci.* 2013, 6, 1249-1259.

137. Sun, L.; Tian, C.; Li, M.; Meng, X.; Wang, L.; Wang, R.; Yin, J.; Fu, H. From coconut shell to porous graphene-like nanosheets for high-power supercapacitors. *J. Mater. Chem. A* 2013, 1, 6462-6470.

138. Li, Z.; Zhang, L.; Amirkhiz, B. S.; Tan, X.; Xu, Z.; Wang, H.; Olsen, B. C.; Holt, C.; Mitlin, D. Carbonized chicken eggshell membranes with 3D architectures as high-performance electrode materials for supercapacitors. *Adv. Energy Mater.* 2012, 2, 431-437.

139. Lee, Y. H.; Lee, Y. F.; Chang, K. H.; Hu, C. C. Synthesis of N-doped carbon nanosheets from collagen for electrochemical energy storage/conversion systems. *Electrochem. Commun.* 2011, 13, 50-53.

140. Yun, Y. S.; Cho, S. Y.; Shim, J.; Kim, B. H.; Chang, S.; Baek, S. J.; Huh, Y. S.; Tak, Y.; Park, Y. W.; Park, S. Microporous carbon nanoplates from regenerated silk proteins for supercapacitors. *Adv. Mater.* 2013, 25, 1993-1998.

141. Liang, Y.; Wu, D.; Fu, R. Carbon microfibers with hierarchical porous structure from electrospun fiber-like natural biopolymer. *Sci. Rep.* 2012, 3.

142. Xu, B.; Hou, S.; Cao, G.; Wu, F.; Yang, Y. Sustainable nitrogen-doped porous carbon with high surface areas prepared from gelatin for supercapacitors. *J. Mater. Chem.* 2012, 22, 19088-19093.

143. Gupta, M.; Bawa, A. S.; Semwal, A. D. Effect of barley flour incorporation on the instrumental texture of sponge cake. *Int. J. Food Prop.* 2009, 12, 243-251.

144. Newman, R. K.; Lewis, S. E.; Newman, C. W.; Boik, R. J.; Ramage, R. T. Hypocholesterolemic effect of barley foods on healthy men. *Nutr. Rep. Int.* 1989, 39, 749-760..

145. Hur, S. J.; Decker, E. A.; McClements, D. J. Influence of initial emulsifier type on microstructural changes occurring in emulsified lipids during in vitro digestion. *Food Chem.* 2009, 114, 253-262.

146. Qian, C.; McClements, D. J. Formation of nanoemulsions stabilized by model food-grade emulsifiers using high pressure homogenization: Factors affecting particle size. *Food Hydrocoll.* 2010, 25, 1000-1008.

147. McClements, D. J.; Li, Y. Structured emulsion-based delivery systems: Controlling the digestion and release of lipophilic food components. *Adv. Colloid Interface Sci.* 2010, 159, 213-228.

148. Chen, L.; Remondetto, G. E.; Subirade, M. Food protein-based materials as nutraceutical delivery systems. *Trends Food Sci. Technol.* 2006, 17, 272-283.

149. Zhai, J.; Hoffmann, S. V.; Day, L.; Lee, T. H.; Augustin, M. A.; Aguilar, M. I.; Wooster, T. J. Conformational changes of alpha-lactalbumin adsorbed at oil-water interfaces: interplay between protein structure and emulsion stability. *Langmuir* 2012, 28, 2357-2367.

150. Li, Y.; Zheng, J. K.; Xiao, H.; McClements, D. J. Nanoemulsion-based delivery systems for poorly water-soluble bioactive compounds: Influence of formulation parameters on polymethoxyflavone crystallization. *Food Hydrocoll.* 2012, 27, 517-528.

151. Lee, S. H.; Lefèvre, T.; Subirade, M.; Paquin, P. Changes and roles of secondary structures of whey protein for the formation of protein membrane at soy oil/water interface under high-pressure homogenization. *J. Agric. Food Chem.* 2007, 55, 10924-10931.

152. Kim, J.; Swager, T. M. Control of conformational and interpolymer effects in conjugated polymers. *Nature* 2001, 411, 1030-1034.

153. López-Montero, I.; Arriaga, L. R.; Rivas, G.; Vélez , M.; Monroy, F. Lipid domains and mechanical plasticity of *Escherichia coli* lipid monolayers. *Chem Phys Lipids* 2010, 163, 56-63.

154. Yalcin, E.; Celik, S.; Ibanoglu, E. Foaming properties of barley protein isolates and hydrolysates. *Eur. Food Res. Technol.* 2008, 226, 967-974.

155. Yang, J.; Zhou, Y.; Chen, L. Elaboration and characterization of barley protein nanoparticles as an oral delivery system for lipophilic bioactive compounds. *Food Funct.* 2014, 5, 92-101.

156. Marchylo, B. A.; Kruger, J. E. Identification of Canadian barley cultivars by reversed-phase high-performance liquid chromatography. *Cereal Chem.* 1984, 61, 295-301.

157. Shewry, P. R.; Ellis, J. R. S.; Pratt, H. M.; Miflin, B. J. A comparison of methods for the extraction and separation of hordein fractions from 29 barley varieties. *J. Sci. Food Agric.* 1978, 29, 433-441.

158. Bos, M. A.; Dunnewind, B.; van Vliet, T. Foams and surface rheological properties of bata-casein, gliadin and glycinin. *Colloids Surf., B* 2003, 31, 95-105.

159. Langmuir, I.; Schaefer, V. J. Properties and structure of protein monolayers. *Chem Rev* 1939, 24, 181-202.

160. Banc, A.; Desbat, B.; Renard, D.; Popineau, Y.; Mangavel, C.; Navailles, L. Exploring the interactions of gliadins with model membranes: effect of confined geometry and interfaces. *Biopolymers* 2009, 91, 610-622.

161. Lenk, T. J.; Horbett, T. A.; Ratner, B. D.; Chittur, K. K. Infrared spectroscopic studies of time-dependent changes in fibrinogen adsorbed to polyurethanes. *Langmuir* 1991, 7, 1755-1764.

162. Bantchev, G. B.; Schwartz, D. K. Surface shear rheology of beta-casein layers at the air/solution interface: Formation of a two-dimensional physical gel. *Langmuir* 2003, 19, 2673-2682.

163. Graham, D. E.; Phillips, M. C. Proteins at liquid interfaces: II. Adsorption isotherms. *J. Colloid Interface Sci.* 1979, 70, 415-426.

164. Croguennec, T.; Renault, A.; Bouhallab, S.; Pezennec, S. Interfacial and foaming properties of sulfydryl-modified bovine beta-lactoglobulin. *J. Colloid Interface Sci.* 2006, 302, 32-39.

165. Ipsen, R.; Otte, J. The relation between protein structure, interfacial rheology and foam formation for various milk proteins. *Annu. Trans. Nord. Rheol. Soc.* 2004, 12, 143-148.

166. Mahmoudi, N.; Axelos, M. A. V.; Riaublanc, A. Interfacial properties of fractal and spherical whey protein aggregates. *Soft Matter* 2011, 7, 7643-7654.

167. Erni, P.; Windhab, E. J.; Gunde, R.; Graber, M.; Pfister, B.; Parker, A.; Fischer, P. Interfacial rheology of surface-active biopolymers: Acacia senegal gum versus hydrophobically modifed starch. *Biomacromolecules* 2007, 8, 3458-3466.

168. Humblet-Hua, N.-P. K.; van der Linden, E.; Sagis, L. M. C. Surface rheological properties of liquid-liquid interfaces stabilized by protein fibrillar aggregates and protein-polysaccharide complexes. *Soft Matter* 2013, 9, 2154-2165.

169. Rodríguez Patino, J. M.; Molina Ortiz, S. E.; Carrera Sánchez, C.; Rodríguez Niño, M. R.; Añón, M. C. Dynamic properties of soy globulin adsorbed films at the air-water interface. *J. Colloid Interface Sci.* 2003, 268, 50-57.

170. Medrano, A.; Abirached, C.; Araujo, A. C.; Panizzolo, L. A.; Moyna, P.; Añón, M. C. Correlation of average hydrophobicity, water/air interface surface rheological properties and foaming properties of proteins. *Food Sci. Technol. Int.* 2012, 18, 187-193.

171. Rossetti, D.; Yakubov, G. E.; Stokes, J. R.; Williamson, A. M.; Fuller, G. G. Interaction of human whole saliva and astringent dietary compounds investigated by interfacial shear rheology. *Food Hydrocoll.* 2008, 22, 1068-1078.

172. Vessely, C. R.; Carpenter, J. F.; Schwartz, D. K. Calcium-induced changes to the molecular conformation and aggregate structure of beta-casein at the air-water interface. *Biomacromolecules* 2005, 6, 3334-3344.

173. Murray, B. S.; Nelson, P. V. A novel Langmuir trough for equilibrium and dynamic measurements on air-water and oil-water monolayers. *Langmuir* 1996, 12, 5973-5976.

174. Örnebro, J.; Nylander, T.; Eliasson, A. C.; Shewry, P. R.; Tatham, A. S.; Gilbert, S. M. The behaviour of the high molecular-weight glutenin subunit 1Dx5, the 58 kDa central repetitive domain and alpha-gliadins at the air-aqueous interface. *J. Cereal Sci.* 2003, 38, 147-156.

175. Kamilya, T.; Pal, P.; Talapatra, G. B. Interaction of ovalbumin with phospholipids Langmuir-Blodgett film. *J. Phys. Chem. B* 2007, 111, 1199-1205.

176. Graham, D. E.; Phillips, M. C. Proteins at liquid interfaces: III. Molecular structures of adsorbed films. *J. Colloid Interface Sci.* 1979, 70, 427-439.

177. Kaganer, V. M.; Möhwald, H.; Dutta, P. Structure and phase transitions in Langmuir monolayers. *Rev. Mod. Phys.* 1999, 71, 779-820.

178. Dervichian, D. G. Changes of phase and transformations of higher order in monolayers. *J. Chem. Phys.* 1939, 7, 931-948.

179. Murray, B. S. Equilibrium and dynamic surface pressure-area measurements on protein films at air-water and oil-water interfaces. *Colloids Surf., A* 1997, 125, 73-83.

180. Caswell, D. S.; Spiro, T. G. Proline signals in ultraviolet resonance Raman spectra of proteins: cis-trans isomerism in polyproline and ribonuclease A. *J. Am. Chem. Soc.* 1987, 109, 2796-2800.

181. Roach, P.; Farrar, D.; Perry, C. C. Interpretation of protein adsorption: surface-induced conformational changes. *J. Am. Chem. Soc.* 2005, 127, 8168-8173.

182. Cornut, I.; Desbat, B.; Turlet, J. M.; Dufourcq, J. *In situ* study by polarization modulated Fourier transform infrared spectroscopy of the structure and orientation of lipids and amphipathic peptides at the air-water interface. *Biophys. J.* 1996, 70, 305-312.

183. Buffeteau, T.; Le Calvez, E.; Castano, S.; Desbat, B.; Blaudez, D.; Dufourcq, J. Anisotropic optical constants of α-helix and β-sheet secondary structures in the infrared. *J. Phys.Chem.* 2000, 104, 4537-4544.

184. Chirgadze, Y. N.; Fedorov, O. V.; Trushina, N. P. Estimation of amino acid residue side-chain absorption in the infrared spectra of protein solutions in heavy water. *Biopolymers* 1975, 14, 679-694.

185. Barth, A. The infrared absorption of amino acid side chains. *Prog. Biophys. Mol. Bio.l* 2000, 74, 141-173.

186. Castano, S.; Desbat, B.; Dufourcq, J. Ideally amphipathic beta-sheeted peptides at interfaces: structure, orientation, affinities for lipids and hemolytic activity of $(KL)_mK$ peptides. *Biochim. Biophys. Acta, Biomembr.* 2000, 1463, 65-80.

187. Dluhy, R. A.; Shanmukh, S.; Brian Leapard, J.; Krüger, P.; Baatz, J. E. Deacylated pulmonary surfactant protein SP-C transforms from alpha-helical to amyloid fibril structure via a pH-dependent mechanism: an infrared structural investigation. *Biophys. J.* 2003, 85, 2417-2429.

188. Chou, P. Y.; Fasman, G. D. Empirical predictions of protein conformation. *Annu. Rev. Biochem.* 1978, 47, 251-276.

189. Thakur, G.; Wang, C.; Leblanc, R. M. Surface chemistry and *in situ* spectroscopy of a lysozyme Langmuir monolayer. *Langmuir* 2008, 24, 4888-4893.

190. Kim, F.; Cote, L. J.; Huang, J. Graphene oxide: Surface activity and two-dimensional assembly. *Adv. Mater.* 2010, 22, 1954-1958.

191. Mackie, A.; Macierzanka, A. Colloidal aspects of protein digestion. *Curr. Opin. Colloid Interface Sci.* 2010, 15, 102-108.

192. Tang, J. Specificity of pepsin and its dependence on a possible "hydrophobic binding site". *Nature* 1963, 199, 1094 - 1095.

193. Kaya-Celiker, H.; Mallikarjunan, K. Better nutrients and therapeutics delivery in food through nanotechnology. *Food Eng. Rev.* 2012, 4, 114-123.

194. Erdman Jr, J. W.; Bierer, T. L.; Gugger, E. T. Absorption and transport of carotenoids. *Ann. N Y Acad. Sci.* 1993, 691, 76-85.

195. Acosta, E. Bioavailability of nanoparticles in nutrient and nutraceutical delivery. *Curr. Opin. Colloid Interface Sci.* 2009, 14, 3-15.

196. Weiss, J.; Takhistov, P.; McClements, D. J. Functional materials in food nanotechnology. *J. Food Sci.* 2006, 71, R107-R116.

197. Ezpeleta, I.; Irache, J. M.; Stainmesse, S.; Chabenat, C.; Gueguen, J.; Popineau, Y.; Orecchioni, A. M. Gliadin nanoparticles for the controlled release of all-trans-retinoic acid. *Int. J. Pharm.* 1996, 131, 191-200.

198. Pan, X.; Yao, P.; Jiang, M. Simultaneous nanoparticle formation and encapsulation driven by hydrophobic interaction of casein-graft-dextran and β-carotene. *J. Colloid Interface Sci.* 2007, 315, 456-463.

199. Porter, C. J. H.; Trevaskis, N. L.; Charman, W. N. Lipids and lipid-based formulations: optimizing the oral delivery of lipophilic drugs. *Nat. Rev. Drug Discov.* 2007, 6, 231-248.

200. Li, Y.; Hu, M.; McClements, D. J. Factors affecting lipase digestibility of emulsified lipids using an *in vitro* digestion model: Proposal for a standardised pH-stat method. *Food Chem.* 2011, 126, 498-505.

201. Singh, A.; He, B.; Thompson, J.; Van Gerpen, J. Process optimization of biodiesel production using alkaline catalysts. *Appl. Eng. Agric.* 2006, 22, 597-600.

202. Dickinson, E. Proteins at interfaces and in emulsions - Stability, rheology and interactions. *J. Chem. Soc., Faraday Trans.* 1998, 94, 1657-1669.

203. Anton, N.; Benoit, J. P.; Saulnier, P. Design and production of nanoparticles formulated from nano-emulsion templates - A review. *J. Controlled Release* 2008, 128, 185-199.

204. Jafari, S. M.; Assadpoor, E.; He, Y.; Bhandari, B. Re-coalescence of emulsion droplets during high-energy emulsification. *Food Hydrocoll.* 2008, 22, 1191-1202.

205. Tan, C. P.; Nakajima, M. beta-Carotene nanodispersions: preparation, characterization and stability evaluation. *Food Chem.* 2005, 92, 661-671.

206. Yuan, Y.; Gao, Y. X.; Zhao, J.; Mao, L. Characterization and stability evaluation of beta-carotene nanoemulsions prepared by high pressure homogenization under various emulsifying conditions. *Food Res. Int.* 2008, 41, 61-68.

207. Guimaraes, C. A.; Menaa, F.; Menaa, B.; Quenca-Guillen, J. S.; Matos, J. D.; Mercuri, L. P.; Braz, A. B.; Rossetti, F. C.; Kedor-Hackmann, E. R. M.; Santoro, M. Comparative physical-chemical characterization of encapsulated lipid-based isotretinoin products assessed by particle size distribution and thermal behavior analyses. *Thermochim. Acta* 2010, 505, 73-78.

208. Muller, R. H.; Harden, D.; Keck, C. M. Development of industrially feasible concentrated 30% and 40% nanoemulsions for intravenous drug delivery. *Drug Dev. Ind. Pharm.* 2012, 38, 420-430.

209. Jafari, S. M.; He, Y.; Bhandari, B. Optimization of nano-emulsions production by microfluidization. *Eur. Food Res. Technol.* 2007, 225, 733-741.

210. Dickinson, E.; van Vliet, T. Colloidal aggregation: Mechanisms and implications. In *Food colloids, biopolymers and materials* Dickinson, E.; van Vliet, T., Eds. Royal Society of Chemistry: Cambridge, 2003; Vol. 284, pp 68-83.

211. Luo, Y. C.; Teng, Z.; Wang, Q. Development of zein nanoparticles coated with carboxymethyl chitosn for encapsulation and controlled release of vitamin D3. *J. Agric. Food Chem.* 2012, 60, 836-843.

212. Arangoa, M. A.; Campanero, M. A.; Renedo, M. J.; Ponchel, G.; Irache, J. M. Gliadin nanoparticles as carriers for the oral administration of lipophilic drugs. Relationships between bioadhesion and pharmacokinetics. *Pharm. Res.* 2001, 18, 1521-1527.

213. Zhang, J.; Liang, L.; Tian, Z.; Chen, L.; Subirade, M. Preparation and *in vitro* evaluation of calcium-induced soy protein isolate nanoparticles and their formation mechanism study. *Food Chem.* 2012, 133, 390-399.

214. Kim, Y. D.; Morr, C. V. Microencapsulation properties of gum Arabic and several food proteins: Spray-dried orange oil emulsion particles. *J. Agric. Food Chem.* 1996, 44, 1314-1320.

215. McClements, D. J.; Rao, J. Food-grade nanoemulsions: formulation, fabrication, properties, performance, biological fate, and potential toxicity. *Crit. Rev. Food Sci. Nutr.* 2011, 51, 285-330.

216. Arangoa, M. A.; Ponchel, G.; Orecchioni, A. M.; Renedo, M. J.; Duchene, D.; Irache, J. M. Bioadhesive potential of gliadin nanoparticulate systems. *Eur. J. Pharm. Sci.* 2000, 11, 333-341.

217. Lai, L. F.; Guo, H. X. Preparation new 5-fluorouracil-loaded zein nanoparticles for liver targeting. *Int. J. Pharm.* 2011, 404, 317-323.

218. Chen, L. Protein micro/nanoparticles for controlled nutraceutical delivery in functional foods. In *Designing functional foods: measuring and controlling food structure breakdown and nutrient absorption*; McClements, D. J., Decker, E. A., Eds.; CRC Press: Oxford, 2009; pp 572-600.

219. Chen, L. Y.; Subirade, M. Chitosan/β-lactoglobulin core-shell nanoparticles as nutraceutical carriers. *Biomaterials* 2005, 26, 6041-6053.

220. Simpson, D. J. Proteolytic degradation of cereal prolamins-the problem with proline. *Plant Sci.* 2001, 161, 825-838.

221. Konovalov, V. V.; Kispert, L. D. AM1, INDO/S and optical studies of carbocations of carotenoid molecules. Acid induced isomerization. *J. Chem. Soc., Perkin Trans. 2* 1999, 901-910.

222. Boon, C. S.; McClements, D. J.; Weiss, J.; Decker, E. A. Factors influencing the chemical stability of carotenoids in foods. *Crit. Rev. Food Sci. Nutr.* 2010, 50, 515-532.

223. Liang, L.; Line, V. L. S.; Remondetto, G. E.; Subirade, M. *In vitro* release of alpha-tocopherol from emulsion-loaded beta-lactoglobulin gels. *Int. Dairy J.* 2010, 20, 176-181.

224. Beaulieu, L.; Savoie, L.; Paquin, P.; Subirade, M. Elaboration and characterization of whey protein beads by an emulsification/cold gelation process: application for the protection of retinol. *Biomacromolecules* 2002, 3, 239-248.

225. Hernell, O.; Staggers, J. E.; Carey, M. C. Physical-chemical behavior of dietary and biliary lipids during intestinal digestion and absorption. 2. Phase analysis and aggregation states of luminal lipids during duodenal fat digestion in healthy adult human beings. *Biochemistry* 1990, 29, 2041-2056.

226. Hidalgo, I. J.; Raub, T. J.; Borchardt, R. T. Characterization of the human colon carcinoma cell line (Caco-2) as a model system for intestinal epithelial permeability. *Gastroenterology* 1989, 96, 736-749.

227. Jung, T.; Kamm, W.; Breitenbach, A.; Kaiserling, E.; Xiao, J. X.; Kissel, T. Biodegradable nanoparticles for oral delivery of peptides: is there a role for polymers to affect mucosal uptake? *Eur. J. Pharm. Biopharm.* 2000, 50, 147-160.

228. Qie, L.; Chen, W.; Xu, H.; Xiong, X.; Jiang, Y.; Zou, F.; Hu, X.; Xin, Y.; Zhang, Z.; Huang, Y. Synthesis of functionalized 3D hierarchical porous carbon for high-performance supercapacitors. *Energy & Environ. Sci.* 2013, 6, 2497-2504.

229. Qian, H.; Diao, H.; Shirshova, N.; Greenhalgh, E. S.; Steinke, J. G. H.; Shaffer, M. S. P.; Bismarck, A. Activation of structural carbon fibres for potential applications in multifunctional structural supercapacitors. *J. Colloid Interface Sci.* 2013, 395, 241-248.

230. Qiu, B.; Pan, C.; Qian, W.; Peng, Y.; Qiu, L.; Yan, F. Nitrogen-doped mesoporous carbons originated from ionic liquids as electrode materials for supercapacitors. *J. Mater. Chem. A* 2013, 1, 6373-6378.

231. Zhang, Y.; Feng, H.; Wu, X.; Wang, L.; Zhang, A.; Xia, T.; Dong, H.; Li, X.; Zhang, L. Progress of electrochemical capacitor electrode materials: A review. *Int. J. Hydrogen Energy* 2009, 34, 4889-4899.

232. Shanmugam, S.; Osaka, T. Efficient electrocatalytic oxygen reduction over metal free-nitrogen doped carbon nanocapsules. *Chem. Commun.* 2011, 47, 4463-4465.

233. Anderson, T. J.; Lamsal, B. P. Review: Zein extraction from corn, corn products, and coproducts and modifications for various applications: A review. *Cereal Chem.* 2011, 88, 159-173.

234. Dallmeyer, I.; Lin, L. T.; Li, Y.; Ko, F.; Kadla, J. F. Preparation and characterization of interconnected, kraft lignin-based carbon fibrous materials by electrospinning. *Macromol. Mater. Eng.* 2014, 299, 540-551.

235. Braun, J. L.; Holtman, K. M.; Kadla, J. F. Lignin-based carbon fibers: Oxidative thermostabilization of kraft lignin. *Carbon* 2005, 43, 385-394.

236. Bier, J. M.; Verbeek, C. J. R.; Lay, M. C. Thermal transitions and structural relaxations in protein-based thermoplastics. *Macromol. Mater. Eng.* 2014, 299, 524-539.

237. Salas, C.; Ago, M.; Lucia, L. A.; Rojas, O. J. Synthesis of soy protein-lignin nanofibers by solution electrospinning. *React. Funct. Polym.* 2015, 85, 221-227.

238. Zhai, Y.; Dou, Y.; Zhao, D.; Fulvio, P. F.; Mayes, R. T.; Dai, S. Carbon materials for chemical capacitive energy storage. *Adv. Mater.* 2011, 23, 4828-4850.

239. Bleda-Martínez, M. J.; Maciá-Agulló, J. A.; Lozano-Castelló, D.; Morallón, E.; Cazorla-Amorós, D.; Linares-Solano, A. Role of surface chemistry on electric double layer capacitance of carbon materials. *Carbon* 2005, 43, 2677-2684.

240. Wang, D. W.; Li, F.; Liu, M.; Lu, G. Q.; Cheng, H. M. 3D aperiodic hierarchical porous graphitic carbon material for high-rate electrochemical capacitive energy storage. *Angew. Chem.* 2008, 120, 379-382.

241. Rodriguez-Reinoso, F.; Molina-Sabio, M. Activated carbons from lignocellulosic materials by chemical and/or physical activation: an overview. *Carbon* 1992, 30, 1111-1118.

242. Lambert, T. N.; Luhrs, C. C.; Chavez, C. A.; Wakeland, S.; Brumbach, M. T.; Alam, T. M. Graphite oxide as a precursor for the synthesis of disordered graphenes using the aerosol-through-plasma method. *Carbon* 2010, 48, 4081-4089.

243. Pumera, M. Graphene-based nanomaterials for energy storage. *Energy Environ. Sci.* 2011, 4, 668-674.

244. Li, Y.; Li, Z.; Shen, P. K. Simultaneous formation of ultrahigh surface area and three-dimensional hierarchical porous graphene-like networks for fast and highly stable supercapacitors. *Adv. Mater.* 2013, 25, 2474-2480.

245. Cho, S. Y.; Yun, Y. S.; Lee, S.; Jang, D.; Park, K. Y.; Kim, J. K.; Kim, B. H.; Kang, K.; Kaplan, D. L.; Jin, H. J. Carbonization of a stable β-sheet-rich silk protein into a pseudographitic pyroprotein. *Nat. Commun.* 2015, 6, 1-7.

246. Castano, S.; Desbat, B.; Laguerre, M.; Dufourcq, J. Structure, orientation and affinity for interfaces and lipids of ideally amphipathic lytic L_iK_j(i=2j) peptides. *Biochim. Biophys. Acta, Biomembr.* 1999, 1416, 176-194.

247. Barth, A. Infrared spectroscopy of proteins. *Biochim. Biophys. Acta, Bioenerg.* 2007, 1767, 1073-1101.

248. Bailey, J. E.; Clarke, A. J. Carbon fibre formation-the oxidation treatment. *Nature* 1971, 529-531.

249. Sing, K. S. W. Reporting physisorption data for gas/solid systems with special reference to the determination of surface area and porosity (Recommendations 1984). *Pure Appl. Chem.* 1985, 57, 603-619.

250. Chen, H.; Müller, M. B.; Gilmore, K. J.; Wallace, G. G.; Li, D. Mechanically strong, electrically conductive, and biocompatible graphene paper. *Adv. Mater.* 2008, 20, 3557-3561.

251. Spyrou, K.; Rudolf, P. An introduction to graphene. In *Functionalization of graphene*; Vasilios G., Eds.; Wiley-VCH: Germany, 2014; pp 1-20.

252. Shen, J.; Hu, Y.; Shi, M.; Lu, X.; Qin, C.; Li, C.; Ye, M. Fast and facile preparation of graphene oxide and reduced graphene oxide nanoplatelets. *Chem. Mater.* 2009, 21, 3514-3520.

253. Dresselhaus, M. S.; Dresselhaus, G.; Saito, R.; Jorio, A. Raman spectroscopy of carbon nanotubes. *Phys. Rep.* 2005, 409, 47-99.

254. Wang, G.; Yang, J.; Park, J.; Gou, X.; Wang, B.; Liu, H.; Yao, J. Facile synthesis and characterization of graphene nanosheets. *J. Phys. Chem. C* 2008, 112, 8192-8195.

255. Lee, W. H.; Lee, J. G.; Reucroft, P. J. XPS study of carbon fiber surfaces treated by thermal oxidation in a gas mixture of $O_2/(O_2+N_2)$. *Appl. Surf. Sci.* 2001, 171, 136-142.

256. Ania, C. O.; Khomenko, V.; Raymundo-Piñero, E.; Parra, J. B.; Beguin, F. The large electrochemical capacitance of microporous doped carbon obtained by using a zeolite template. *Adv. Func. Mater.* 2007, 17, 1828-1836.

257. Qu, D. Studies of the activated carbons used in double-layer supercapacitors. *J. Power Sources* 2002, 109, 403-411.

258. Zhou, J. H.; Sui, Z. J.; Zhu, J.; Li, P.; Chen, D.; Dai, Y. C.; Yuan, W. K. Characterization of surface oxygen complexes on carbon nanofibers by TPD, XPS and FT-IR. *Carbon* 2007, 45, 785-796.

259. Eliad, L.; Salitra, G.; Soffer, A.; Aurbach, D. Ion sieving effects in the electrical double layer of porous carbon electrodes: estimating effective ion size in electrolytic solutions. *J. Phys. Chem. B* 2001, 105, 6880-6887.

260. Salitra, G.; Soffer, A.; Eliad, L.; Cohen, Y.; Aurbach, D. Carbon electrodes for double-layer capacitors I. Relations between ion and pore dimensions. *J. Electrochem. Soc.* 2000, 147, 2486-2493.

261. Xufeng, Z.; Wei, W.; Zhaoping, L. Graphene Overview. In *Graphene: energy storage and conversion applications*; Liu Z., Eds.; CRC Press: Boca Raton, 2014; pp 1-20.

262. Zhu, Y.; Murali, S.; Stoller, M. D.; Ganesh, K. J.; Cai, W.; Ferreira, P. J.; Pirkle, A.; Wallace, R. M.; Cychosz, K. A.; Thommes, M. Carbon-based supercapacitors produced by activation of graphene. *Science* 2011, 332, 1537-1541.

263. Xu, J.; Gao, Q.; Zhang, Y.; Tan, Y.; Tian, W.; Zhu, L.; Jiang, L. Preparing two-dimensional microporous carbon from Pistachio nutshell with high areal capacitance as supercapacitor materials. *Sci. Rep.* 2014, 4.

264. Xu, Q.; Yu, X.; Liang, Q.; Bai, Y.; Huang, Z.-H.; Kang, F. Nitrogen-doped hollow activated carbon nanofibers as high performance supercapacitor electrodes. *J. Electroanal. Chem.* 2015, 739, 84-88.

265. Chen, L.; Wang, Z.; He, C.; Zhao, N.; Shi, C.; Liu, E.; Li, J. Porous graphitic carbon nanosheets as a high-rate anode material for lithium-ion batteries. *ACS Appl. Mater. Interfaces* 2013, 5, 9537-9545.

266. Sun, L.; Fu, Y.; Tian, C.; Yang, Y.; Wang, L.; Yin, J.; Ma, J.; Wang, R.; Fu, H. Isolated boron and nitrogen sites on porous graphitic carbon synthesized from nitrogen-containing chitosan for supercapacitors. *ChemSusChem* 2014, 7, 1637-1646.

267. Wang, L.; Mu, G.; Tian, C.; Sun, L.; Zhou, W.; Yu, P.; Yin, J.; Fu, H. Porous graphitic carbon nanosheets derived from cornstalk biomass for advanced supercapacitors. *ChemSusChem* 2013, 6, 880-889.

268. Deng, D.; Liao, X.; Shi, B. Synthesis of porous carbon fibers from collagen fiber. *ChemSusChem* 2008, 1, 298-301.

269. Evans, N. A.; Milligan, B.; Montgomery, K. C. Collagen crosslinking: new binding sites for mineral tannage. *J. Am. Leather Chem. Assoc.* 1987, 82, 86-95.

270. Liao, X. P; Shi, B. I. Adsorption of fluoride on zirconium (IV)-impregnated collagen fiber. *Environ. Sci. Technol.* 2005, 39, 4628-4632.

271. Kim, C.; Ngoc, B. T. N.; Yang, K. S.; Kojima, M.; Kim, Y. A.; Kim, Y. J.; Endo, M.; Yang, S. C. Self-sustained thin webs consisting of porous carbon nanofibers for supercapacitors via the electrospinning of polyacrylonitrile solutions containing xinc chloride. *Adv. Mater.* 2007, 19, 2341-2346.

272. Zong, X.; Kim, K.; Fang, D.; Ran, S.; Hsiao, B. S.; Chu, B. Structure and process relationship of electrospun bioabsorbable nanofiber membranes. *Polymer* 2002, 43, 4403-4412.

273. Yang, L.; Fitie, C. F. C.; van der Werf, K. O.; Bennink, M. L.; Dijkstra, P. J.; Feijen, J. Mechanical properties of single electrospun collagen type I fibers. *Biomaterials* 2008, 29, 955-962.

274. Kim, B.; Park, H.; Lee, S. H.; Sigmund, W. M. Poly (acrylic acid) nanofibers by electrospinning. *Mater. Lett.* 2005, 59, 829-832.

275. Wine, Y.; Cohen-Hadar, N.; Freeman, A.; Frolow, F. Elucidation of the mechanism and end products of glutaraldehyde crosslinking reaction by X-ray structure analysis. *Biotechnol. Bioeng.* 2007, 98, 711-718.

276. Sisson, K.; Zhang, C.; Farach-Carson, M. C.; Chase, D. B.; Rabolt, J. F. Evaluation of cross-linking methods for electrospun gelatin on cell growth and viability. *Biomacromolecules* 2009, 10, 1675-1680.

277. Niu, S.; Han, K.; Lu, C.; Sun, R. Thermogravimetric analysis of the relationship among calcium magnesium acetate, calcium acetate and magnesium acetate. *Appl. Energy* 2010, 87, 2237-2242.

278. Chen, X. Y.; Zhou, Q. Q. The production of porous carbon from calcium lignosulfonate without activation process and the capacitive performance. *Electrochim. Acta* 2012, 71, 92-99.

279. Schwierz, N.; Horinek, D.; Netz, R. R. Specific ion binding to carboxylic surface groups and the pH dependence of the Hofmeister series. *Langmuir* 2014, 31, 215-225.

280. Bryant, C. M.; McClements, D. J. Influence of NaCl and $CaCl_2$ on cold-set gelation of heat-denatured whey protein. *J. Food Sci.* 2000, 65, 801-804.

281. Barreto, P. L. M.; Pires, A. T. N.; Soldi, V. Thermal degradation of edible films based on milk proteins and gelatin in inert atmosphere. *Polym. Degrad. Stab.* 2003, 79, 147-152.

282. Lemos, A. F.; Ferreira, J. M. F. Porous bioactive calcium carbonate implants processed by starch consolidation. *Mater. Sci. Eng.* 2000, 11, 35-40.

283. Yamasaki, N.; Tang, W.; Ke, J. Low-temperature sintering of calcium carbonate by a hydrothermal hot-pressing technique. *J. Mater. Sci. Lett.* 1992, 11, 934-936.

284. Lyckfeldt, O.; Brandt, J.; Lesca, S. Protein forming-a novel shaping technique for ceramics. *J. Eur. Ceram. Soc.* 2000, 20, 2551-2559.

285. Yu, H.-D.; Tee, S. Y.; Han, M.-Y. Preparation of porosity-controlled calcium carbonate by thermal decomposition of volume content-variable calcium carboxylate derivatives. *Chem. Commun.* 2013, 49, 4229-4231.

286. Demri, B.; Muster, D. XPS study of some calcium compounds. *J. Mater. Process. Technol.* 1995, 55, 311-314.

287. Seredych, M.; Hulicova-Jurcakova, D.; Lu, G. Q.; Bandosz, T. J. Surface functional groups of carbons and the effects of their chemical character, density and accessibility to ions on electrochemical performance. *Carbon* 2008, 46, 1475-1488.

288. Ugarte, D. Curling and closure of graphitic networks under electron-beam irradiation. *Nature* 1992, 359, 707-709.

289. Pech, D.; Brunet, M.; Durou, H.; Huang, P.; Mochalin, V.; Gogotsi, Y.; Taberna, P.-L.; Simon, P. Ultrahigh-power micrometre-sized supercapacitors based on onion-like carbon. *Nat. Nanotechnol.* 2010, 5, 651-654.

290. Feng, G.; Qiao, R.; Huang, J.; Dai, S.; Sumpter, B. G.; Meunier, V. The importance of ion size and electrode curvature on electrical double layers in ionic liquids. *Phys. Chem. Chem. Phys.* 2011, 13, 1152-1161.

291. Zhu, Y.; Murali, S.; Cai, W.; Li, X.; Suk, J. W.; Potts, J. R.; Ruoff, R. S. Graphene and graphene oxide: synthesis, properties, and applications. *Adv. Mater.* 2010, 22, 3906-3924.

292. Du, X.; Guo, P.; Song, H.; Chen, X. Graphene nanosheets as electrode material for electric double-layer capacitors. *Electrochim. Acta* 2010, 55, 4812-4819.

293. Sun, L.; Tian, C.; Wang, L.; Zou, J.; Mu, G.; Fu, H. Magnetically separable porous graphitic carbon with large surface area as excellent adsorbents for metal ions and dye. *J. Mater. Chem.* 2011, 21, 7232-7239.

294. Kim, W.; Kang, M. Y.; Joo, J. B.; Kim, N. D.; Song, I. K.; Kim, P.; Yoon, J. R.; Yi, J. Preparation of ordered mesoporous carbon nanopipes with controlled nitrogen species for application in electrical double-layer capacitors. *J. Power Sources* 2010, 195, 2125-2129.

295. Zhu, H.; Wang, X.; Liu, X.; Yang, X. Integrated synthesis of poly (o-phenylenediamine)-derived carbon materials for high performance supercapacitors. *Adv. Mater.* 2012, 24, 6524-6529.

296. Xu, B.; Yue, S.; Sui, Z.; Zhang, X.; Hou, S.; Cao, G.; Yang, Y. What is the choice for supercapacitors: graphene or graphene oxide? *Energy Environ. Sci.* 2011, 4, 2826-2830.

297. Wang, Y.; Shi, Z.; Huang, Y.; Ma, Y.; Wang, C.; Chen, M.; Chen, Y. Supercapacitor devices based on graphene materials. *J. Phys. Chem. C* 2009, 113, 13103-13107.

298. Weng, Z.; Su, Y.; Wang, D. W.; Li, F.; Du, J.; Cheng, H. M. Graphene-cellulose paper flexible supercapacitors. *Adv. Energy Mater.* 2011, 1, 917-922.

Appendix A1

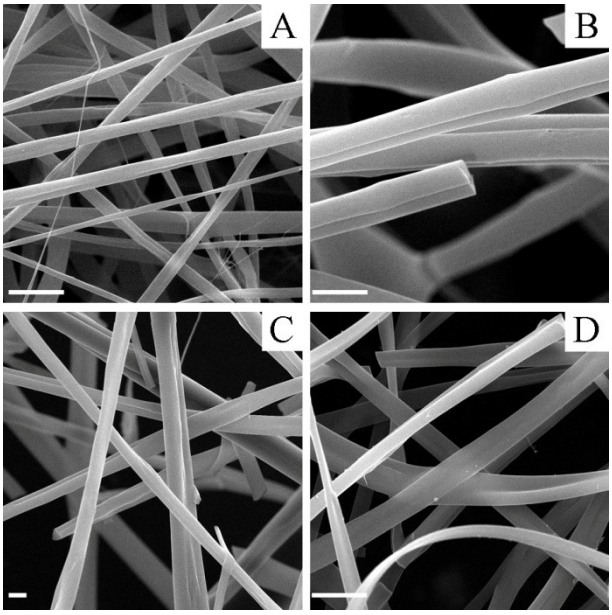

Figure A1-1 SEM images of electrospun protein-lignin fibers: (A) protein; (B) L2P8; (C) L5P5 and (D) L8P2. Scale bar is 2.5 µm.

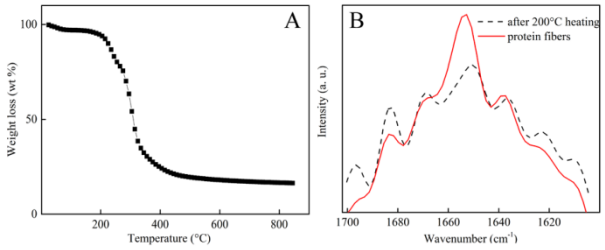

Figure A1-2 (A) TGA of protein fibers with 2 °C/min. (B) deconvoluted FTIR spectra of original electrospun protein fibers and protein fibers heated to 200 °C for 2h.

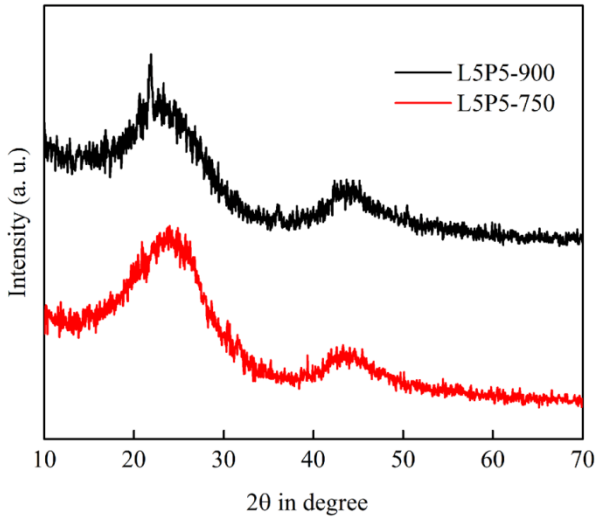

Figure A1-3 XRD patterns of carbon samples L5P5-750 and L5P5-900.

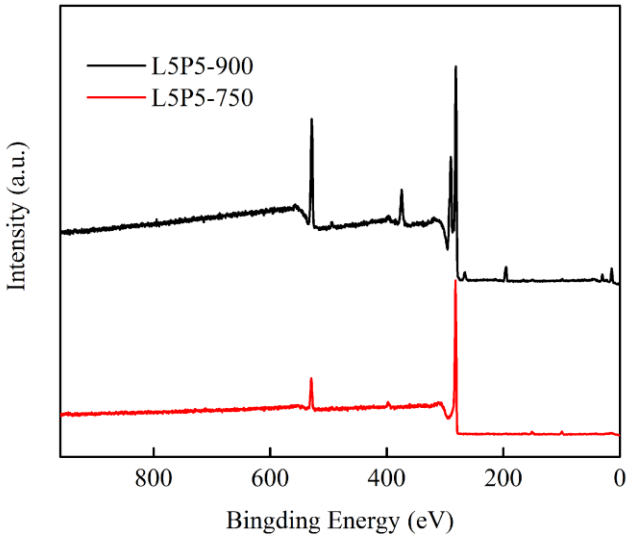

Figure A1-4 XPS spectra of carbon samples L5P5-750 and L5P5-900.

Appendix A2

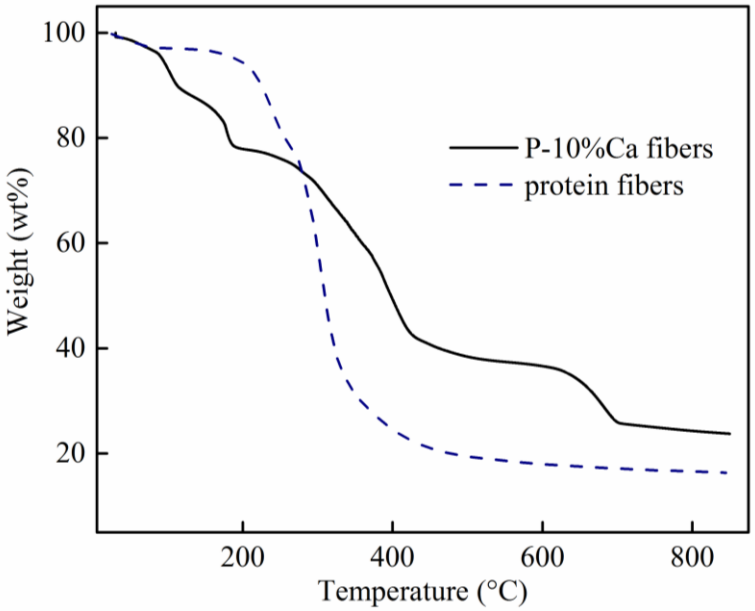

Figure A2-1 TGA of protein original fibers and protein and 10% calcium original electropun fibers with 2 °C/min.

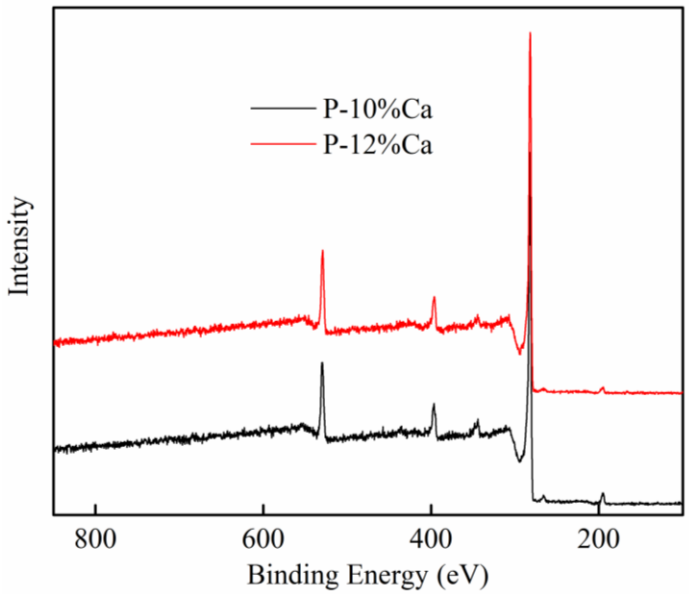

Figure A2-12 XPS survey spectra of P-10%Ca and P-12%Ca.

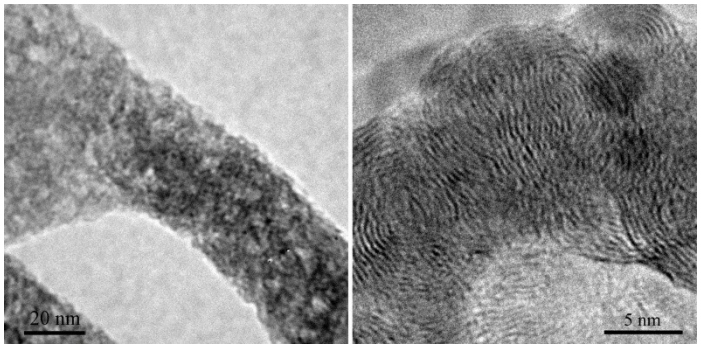

Figure A2-3 HR-TEM images of P-10%Ca.

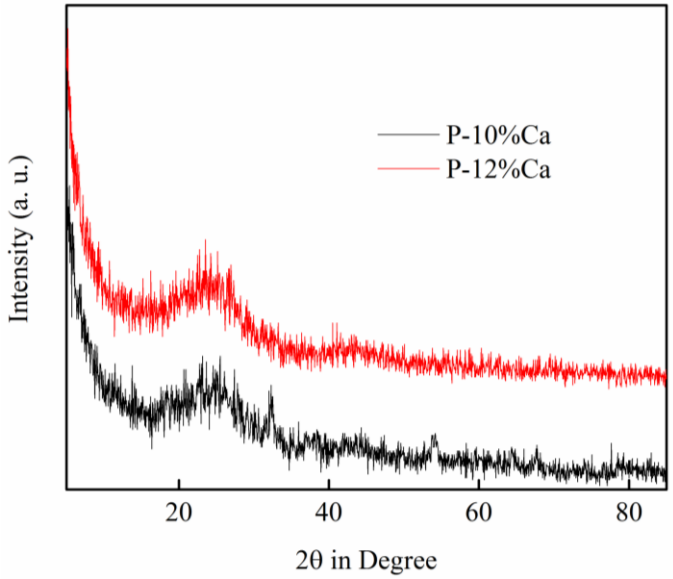

Figure A2-4 XRD patterns of P-10%Ca and P-12%Ca.

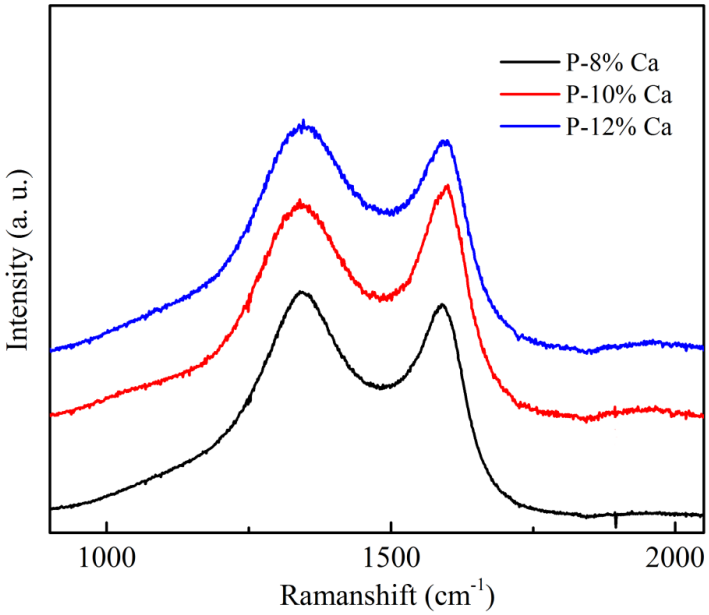

Figure A2-5 Raman spectra of P-8%Ca, P-10%Ca and P-12%Ca.